UNIVERSITY OF CALIFORNIA SAN DIEGO

Using Cosmological Observations to Search for New Physics and Study the Structure of the Universe

A dissertation submitted in partial satisfaction of the
requirements for the degree
Doctor of Philosophy

in

Physics

by

David Leon

Committee in charge:

Professor Brian Keating, Chair
Professor Kam Arnold
Professor David Meyer
Professor Tom Murphy
Professor Mike Norman

2020

The dissertation of David Leon is approved, and it is acceptable in quality and form for publication on microfilm and electronically:

_____

_____

_____

_____

_____

Chair

University of California San Diego

2020

EPIGRAPH

Is there anything of which one can say,
"Look! This is something new"?
It was here already, long ago;
it was here before our time.

Ecclesiastes 1:10

TABLE OF CONTENTS

LIST OF FIGURES

LIST OF TABLES

ACKNOWLEDGEMENTS

First I'd like to thank my advisor Brian Keating. He believed in me and supported me for my graduate career and shared his love of figuring out how the universe works.

I'd like to thank everyone in the POLARBEAR collaboration. Without their hard work and guidance I would have never been able to add my own contribution to the set of POLARBEAR publications.

Among my fellow POLARBEAR collaborators, I have a special place in my heart for all the grad students and researchers who worked beside me in SERF 375. Thanks for showing me all the time and care that goes into building the kind of instruments that make it possible for me to play around with interesting scientific datasets, and thanks for the occasional lab shenanigans in between the work of being a grad student.

I'd like to thank Andy Friedman for giving me the opportunity to poke at the underlying assumptions of physical theories on multiple projects.

And finally I want to thank my family, Christine, Daniel, and Diana, for their love and support in pursuing a passion that has been many long years in the making.

Chapter 2, in full, is a reprint of material as it appears in D. Leon, J. Kaufman, B. Keating, and M. Mewes, "The cosmic microwave background and pseudo-Nambu-Goldstone bosons: Searching for Lorentz violations in the cosmos," Mod. Phys. Lett. A, 32, 1730002, 2017 (arXiv:1611.00418) [1]. The dissertation author was the primary author of this work.

Chapter 3, in full, is a reprint of material as it appears in A.S. Friedman, D. Leon, K.D. Crowley, D. Johnson, G. Teply, D. Tytler, B.G. Keating, and G.M. Cole, "Constraints on Lorentz invariance and CPT violation using optical photometry and polarimetry of active galaxies BL Lacertae and S5 B0716+714," Phys. Rev. D, 99, 035045, 2019 (arXiv:1809.08356) [2]. The dissertation author made essential contributions to this work.

Chapter 4, in full, is a reprint of material as it appears in M. Aguilar Faúndez, K. Arnold, C. Baccigalupi, D. Barron, D. Beck, S. Beckman, F. Bianchini, J. Carron, K. Cheung, Y. Chinone, H. El Bouhargani, T. Elleflot, J. Errard, G. Fabbian, C. Feng, T. Fujino, N.

Goeckner-Wald, T. Hamada, M. Hasegawa, M. Hazumi, C.A. Hill, H. Hirose, O. Jeong, N. Katayama, B. Keating, S. Kikuchi, A. Kusaka, A.T. Lee, D. Leon, E. Linder, L.N. Lowry, F. Matsuda, T. Matsumura, Y. Minami, M. Navaroli, H. Nishino, A.T.P. Pham, D. Poletti, G. Puglisi, C.L. Reichardt, Y. Segawa, B.D. Sherwin, M. Silva-Feaver, P. Siritanasak, R. Stompor, A. Suzuki, O. Tajima, S. Takatori, D. Tanabe, G.P. Teply, and C. Tsai, "Measurement of the Cosmic Microwave Background Polarization Lensing Power Spectrum from Two Years of POLARBEAR Data" ApJ, 893, 85, 2020 (arXiv:1911.10980) [3]. The dissertation author was the primary author of this work.

Chapter 5, in part, contains a reprint of material as it appears in I. Ben-Dayan, B. Keating, D. Leon and I. Wolfson, "Constraints on scalar and tensor spectra from $N_{\rm eff}$," J. Cosmology Astropart. Phys., 2019, 007, 2019 (arXiv:1903.11843) [4]. The dissertation author made essential contributions to this work.

VITA

2012	B. S. in Physics with honors, California Institute of Technology
2012-2014	Graduate Teaching Assistant, University of California San Diego
2014-2020	Graduate Student Researcher, University of California San Diego
2020	Ph. D. in Physics, University of California San Diego

PUBLICATIONS

Mario Aguilar Faúndez, Kam Arnold, Carlo Baccigalupi, Darcy Barron, Dominic Beck, Shawn Beckman, Federico Bianchini, Julien Carron, Kolen Cheung, Yuji Chinone, Hamza El Bouhargani, Tucker Elleflot, Josquin Errard, Giulio Fabbian, Chang Feng, Takuro Fujino, Neil Goeckner-Wald, Takaho Hamada, Masaya Hasegawa, Masashi Hazumi, Charles A. Hill, Haruaki Hirose, Oliver Jeong, Nobuhiko Katayama, Brian Keating, Shuhei Kikuchi, Akito Kusaka, Adrian T. Lee, David Leon, Eric Linder, Lindsay Ng Lowry, Frederick Matsuda, Tomotake Matsumura, Yuto Minami, Martin Navaroli, Haruki Nishino, Anh Thi Phuong Pham, Davide Poletti, Giuseppe Puglisi, Christian L Reichardt, Yuuko Segawa, Blake D Sherwin, Maximiliano Silva-Feaver, Praween Siritanasak, Radek Stompor, Aritoki Suzuki, Osamu Tajima, Sayuri Takatori, Daiki Tanabe, Grant P. Teply, and Calvin Tsai. Measurement of the Cosmic Microwave Background Polarization Lensing Power Spectrum from Two Years of POLARBEAR Data. The Astrophysical Journal, 893(1):85, apr 2020.

S. Adachi, M. A. O. Aguilar Faúndez, Y. Akiba, A. Ali, K. Arnold, C. Baccigalupi, D. Barron, D. Beck, F. Bianchini, J. Borrill, J. Carron, K. Cheung, Y. Chinone, K. Crowley, H. El Bouhargani, T. Elleflot, J. Errard, G. Fabbian, C. Feng, T. Fujino, N. Goeckner-Wald, M. Hasegawa, M. Hazumi, C. A. Hill, L. Howe, N. Katayama, B. Keating, S. Kikuchi, A. Kusaka, A. T. Lee, D. Leon, E. Linder, L. N. Lowry, F. Matsuda, T. Matsumura, Y. Minami, T. Namikawa, M. Navaroli, H. Nishino, J. Peloton, A. T. P. Pham, D. Poletti, G. Puglisi, C. L. Reichardt, Y. Segawa, B. D. Sherwin, M. Silva-Feaver, P. Siritanasak, R. Stompor, O. Tajima, S. Takatori, D. Tanabe, G. P. Teply, and C. Vergès. Internal delensing of cosmic microwave background polarization b-modes with the polarbear experiment. Phys. Rev. Lett., 124:131301, Apr 2020.

Andrew S. Friedman, Roman Gerasimov, Fabian Kislat, David Leon, Walker Stevens, David Tytler, and Brian G. Keating. Improved Constraints on Anisotropic Birefringent Lorentz Invariance and CPT Violation from Broadband Optical Polarimetry of High Redshift Galaxies. arXiv e-prints, page arXiv:2003.00647, March 2020.

M. Aguilar Faúndez, K. Arnold, C. Baccigalupi, D. Barron, D. Beck, F. Bianchini, D. Boettger, J. Borrill, J. Carron, K. Cheung, Y. Chinone, H. El Bouhargani, T. Elleflot, J. Errard, G. Fabbian, C. Feng, N. Galitzki, N. Goeckner-Wald, M. Hasegawa, M. Hazumi, L. Howe, D. Kaneko, N. Katayama, B. Keating, N. Krachmalnicoff, A. Kusaka, A. T. Lee, D. Leon,

E. Linder, L. N. Lowry, F. Matsuda, Y. Minami, M. Navaroli, H. Nishino, A. T. P. Pham, D. Poletti, G. Puglisi, C. L. Reichardt, B. D. Sherwin, M. Silva-Feaver, R. Stompor, A. Suzuki, O. Tajima, S. Takakura, S. Takatori, G. P. Teply, C. Tsai, and C. Vergès and. Cross-correlation of CMB polarization lensing with high-z submillimeter herschel-ATLAS galaxies. The Astrophysical Journal, 886(1):38, nov 2019.

T. Namikawa, Y. Chinone, H. Miyatake, M. Oguri, R. Takahashi, A. Kusaka, N. Katayama, S. Adachi, M. Aguilar, H. Aihara, A. Ali, R. Armstrong, K. Arnold, C. Baccigalupi, D. Barron, D. Beck, S. Beckman, F. Bianchini, D. Boettger, J. Borrill, K. Cheung, L. Corbett, K. T. Crowley, H. El Bouhargani, T. Elleflot, J. Errard, G. Fabbian, C. Feng, N. Galitzki, N. Goeckner-Wald, J. Groh, T. Hamada, M. Hasegawa, M. Hazumi, C. A. Hill, L. Howe, O. Jeong, D. Kaneko, B. Keating, A. T. Lee, D. Leon, E. Linder, L. N. Lowry, A. Mangu, F. Matsuda, Y. Minami, S. Miyazaki, H. Murayama, M. Navaroli, H. Nishino, A. J. Nishizawa, A. T. P. Pham, D. Poletti, G. Puglisi, C. L. Reichardt, B. D. Sherwin, M. Silva-Feaver, P. Siritanasak, J. S. Speagle, R. Stompor, A. Suzuki, P. J. Tait, O. Tajima, M. Takada, S. Takakura, S. Takatori, D. Tanabe, M. Tanaka, G. P. Teply, C. Tsai, C. Vergés, B. Westbrook, and Y. Zhou and. Evidence for the cross-correlation between cosmic microwave background polarization lensing from polarbear and cosmic shear from subaru hyper suprime-cam. The Astrophysical Journal, 882(1):62, sep 2019.

Ido Ben-Dayan, Brian Keating, David Leon, and Ira Wolfson. Constraints on scalar and tensor spectra from neff. Journal of Cosmology and Astroparticle Physics, 2019(06):007–007, jun 2019.

Andrew S. Friedman, David Leon, Roman Gerasimov, Kevin D. Crowley, Isaac Broudy, Yash Melkani, Walker Stevens, Delwin Johnson, Grant Teply, David Tytler, Brian G. Keating, and Gary M. Cole. Standard-Model Extension Constraints on Lorentz and CPT Violation From Optical Polarimetry of Active Galactic Nuclei. arXiv e-prints, page arXiv:1906.07301, June 2019.

Andrew S. Friedman, David Leon, Kevin D. Crowley, Delwin Johnson, Grant Teply, David Tytler, Brian G. Keating, and Gary M. Cole. Constraints on lorentz invariance and *cpt* violation using optical photometry and polarimetry of active galaxies bl lacertae and s5 b0716+714. Phys. Rev. D, 99:035045, Feb 2019.

Peter Ade, James Aguirre, Zeeshan Ahmed, Simone Aiola, Aamir Ali, David Alonso, Marcelo A. Alvarez, Kam Arnold, Peter Ashton, Jason Austermann, Humna Awan, Carlo Baccigalupi, Taylor Baildon, Darcy Barron, Nick Battaglia, Richard Battye, Eric Baxter, Andrew Bazarko, James A. Beall, Rachel Bean, Dominic Beck, Shawn Beckman, Benjamin Beringue, Federico Bianchini, Steven Boada, David Boettger, J. Richard Bond, Julian Borrill, Michael L. Brown, Sarah Marie Bruno, Sean Bryan, Erminia Calabrese, Victoria Calafut, Paolo Calisse, Julien Carron, Anthony Challinor, Grace Chesmore, Yuji Chinone, Jens Chluba, Hsiao-Mei Sherry Cho, Steve Choi, Gabriele Coppi, Nicholas F. Cothard, Kevin Coughlin, Devin Crichton, Kevin D. Crowley, Kevin T. Crowley, Ari Cukierman, John M. D'Ewart, Rolando Dünner, Tijmen de Haan, Mark Devlin, Simon Dicker, Joy Didier, Matt Dobbs, Bradley Dober, Cody J. Duell, Shannon Duff, Adri Duivenvoorden, Jo Dunkley, John Dusatko,

Josquin Errard, Giulio Fabbian, Stephen Feeney, Simone Ferraro, Pedro Fluxà, Katherine Freese, Josef C. Frisch, Andrei Frolov, George Fuller, Brittany Fuzia, Nicholas Galitzki, Patricio A. Gallardo, Jose Tomas Galvez Ghersi, Jiansong Gao, Eric Gawiser, Martina Gerbino, Vera Gluscevic, Neil Goeckner-Wald, Joseph Golec, Sam Gordon, Megan Gralla, Daniel Green, Arpi Grigorian, John Groh, Chris Groppi, Yilun Guan, Jon E. Gudmundsson, Dongwon Han, Peter Hargrave, Masaya Hasegawa, Matthew Hasselfield, Makoto Hattori, Victor Haynes, Masashi Hazumi, Yizhou He, Erin Healy, Shawn W. Henderson, Carlos Hervias-Caimapo, Charles A. Hill, J. Colin Hill, Gene Hilton, Matt Hilton, Adam D. Hincks, Gary Hinshaw, Renée Hložek, Shirley Ho, Shuay-Pwu Patty Ho, Logan Howe, Zhiqi Huang, Johannes Hubmayr, Kevin Huffenberger, John P. Hughes, Anna Ijjas, Margaret Ikape, Kent Irwin, Andrew H. Jaffe, Bhuvnesh Jain, Oliver Jeong, Daisuke Kaneko, Ethan D. Karpel, Nobuhiko Katayama, Brian Keating, Sarah S. Kernasovskiy, Reijo Keskitalo, Theodore Kisner, Kenji Kiuchi, Jeff Klein, Kenda Knowles, Brian Koopman, Arthur Kosowsky, Nicoletta Krachmalnicoff, Stephen E. Kuenstner, Chao-Lin Kuo, Akito Kusaka, Jacob Lashner, Adrian Lee, Eunseong Lee, David Leon, Jason S.-Y. Leung, Antony Lewis, Yaqiong Li, Zack Li, Michele Limon, Eric Linder, Carlos Lopez-Caraballo, Thibaut Louis, Lindsay Lowry, Marius Lungu, Mathew Madhavacheril, Daisy Mak, Felipe Maldonado, Hamdi Mani, Ben Mates, Frederick Matsuda, Lo¨ic Maurin, Phil Mauskopf, Andrew May, Nialh McCallum, Chris McKenney, Jeff McMahon, P. Daniel Meerburg, Joel Meyers, Amber Miller, Mark Mirmelstein, Kavilan Moodley, Moritz Munchmeyer, Charles Munson, Sigurd Naess, Federico Nati, Martin Navaroli, Laura Newburgh, Ho Nam Nguyen, Michael Niemack, Haruki Nishino, John Orlowski-Scherer, Lyman Page, Bruce Partridge, Julien Peloton, Francesca Perrotta, Lucio Piccirillo, Giampaolo Pisano, Davide Poletti, Roberto Puddu, Giuseppe Puglisi, Chris Raum, Christian L. Reichardt, Mathieu Remazeilles, Yoel Rephaeli, Dominik Riechers, Felipe Rojas, Anirban Roy, Sharon Sadeh, Yuki Sakurai, Maria Salatino, Mayuri Sathyanarayana Rao, Emmanuel Schaan, Marcel Schmittfull, Neelima Sehgal, Joseph Seibert, Uros Seljak, Blake Sherwin, Meir Shimon, Carlos Sierra, Jonathan Sievers, Precious Sikhosana, Maximiliano Silva-Feaver, Sara M. Simon, Adrian Sinclair, Praween Siritanasak, Kendrick Smith, Stephen R. Smith, David Spergel, Suzanne T. Staggs, George Stein, Jason R. Stevens, Radek Stompor, Aritoki Suzuki, Osamu Tajima, Satoru Takakura, Grant Teply, Daniel B. Thomas, Ben Thorne, Robert Thornton, Hy Trac, Calvin Tsai, Carole Tucker, Joel Ullom, Sunny Vagnozzi, Alexander van Engelen, Jeff Van Lanen, Daniel D. Van Winkle, Eve M. Vavagiakis, Clara Vergès, Michael Vissers, Kasey Wagoner, Samantha Walker, Jon Ward, Ben Westbrook, Nathan Whitehorn, Jason Williams, Joel Williams, Edward J. Wollack, Zhilei Xu, Byeonghee Yu, Cyndia Yu, Fernando Zago, Hezi Zhang, and Ningfeng Zhu and. The simons observatory: science goals and forecasts. Journal of Cosmology and Astroparticle Physics, 2019(02):056–056, feb 2019.

B. Westbrook, P. A. R. Ade, M. Aguilar, Y. Akiba, K. Arnold, C. Baccigalupi, D. Barron, D. Beck, S. Beckman, A. N. Bender, F. Bianchini, D. Boettger, J. Borrill, S. Chapman, Y. Chinone, G. Coppi, K. Crowley, A. Cukierman, T. de Haan, R. Dünner, M. Dobbs, T. Elleflot, J. Errard, G. Fabbian, S. M. Feeney, C. Feng, G. Fuller, N. Galitzki, A. Gilbert, N. Goeckner-Wald, J. Groh, N. W. Halverson, T. Hamada, M. Hasegawa, M. Hazumi, C. A. Hill, W. Holzapfel, L. Howe, Y. Inoue, G. Jaehnig, A. Jaffe, O. Jeong, D. Kaneko, N. Katayama, B. Keating, R. Keskitalo, T. Kisner, N. Krachmalnicoff, A. Kusaka, M. Le

Jeune, A. T. Lee, D. Leon, E. Linder, L. Lowry, A. Madurowicz, D. Mak, F. Matsuda, A. May, N. J. Miller, Y. Minami, J. Montgomery, M. Navaroli, H. Nishino, J. Peloton, A. Pham, L. Piccirillo, D. Plambeck, D. Poletti, G. Puglisi, C. Raum, G. Rebeiz, C. L. Reichardt, P. L. Richards, H. Roberts, C. Ross, K. M. Rotermund, Y. Segawa, B. Sherwin, M. Silva-Feaver, P. Siritanasak, R. Stompor, A. Suzuki, O. Tajima, S. Takakura, S. Takatori, D. Tanabe, R. Tat, G. P. Teply, A. Tikhomirov, T. Tomaru, C. Tsai, N. Whitehorn, and A. Zahn. The POLARBEAR-2 and Simons Array Focal Plane Fabrication Status. Journal of Low Temperature Physics, 193(5-6):758–770, December 2018.

Dominik Rauch, Johannes Handsteiner, Armin Hochrainer, Jason Gallicchio, Andrew S. Friedman, Calvin Leung, Bo Liu, Lukas Bulla, Sebastian Ecker, Fabian Steinlechner, Rupert Ursin, Beili Hu, David Leon, Chris Benn, Adriano Ghedina, Massimo Cecconi, Alan H. Guth, David I. Kaiser, Thomas Scheidl, and Anton Zeilinger. Cosmic bell test using random measurement settings from high-redshift quasars. Phys. Rev. Lett., 121:080403, Aug 2018.

POLARBEAR Collaboration, P. A. R. Ade, M. Aguilar, Y. Akiba, K. Arnold, C. Baccigalupi, D. Barron, D. Beck, F. Bianchini, D. Boettger, J. Borrill, S. Chapman, Y. Chinone, K. Crowley, A. Cukierman, R. Dünner, M. Dobbs, A. Ducout, T. Elleflot, J. Errard, G. Fabbian, S. M. Feeney, C. Feng, T. Fujino, N. Galitzki, A. Gilbert, N. Goeckner-Wald, J. C. Groh, G. Hall, N. Halverson, T. Hamada, M. Hasegawa, M. Hazumi, C. A. Hill, L. Howe, Y. Inoue, G. Jaehnig, A. H. Jaffe, O. Jeong, D. Kaneko, N. Katayama, B. Keating, R. Keskitalo, T. Kisner, N. Krachmalnicoff, A. Kusaka, M. Le Jeune, A. T. Lee, E. M. Leitch, D. Leon, E. Linder, L. Lowry, F. Matsuda, T. Matsumura, Y. Minami, J. Montgomery, M. Navaroli, H. Nishino, H. Paar, J. Peloton, A. T. P. Pham, D. Poletti, G. Puglisi, C. L. Reichardt, P. L. Richards, C. Ross, Y. Segawa, B. D. Sherwin, M. Silva-Feaver, P. Siritanasak, N. Stebor, R. Stompor, A. Suzuki, O. Tajima, S. Takakura, S. Takatori, D. Tanabe, G. P. Teply, T. Tomaru, C. Tucker, N. Whitehorn, and A. Zahn. A Measurement of the Cosmic Microwave Background B-mode Polarization Power Spectrum at Subdegree Scales from Two Years of polarbear Data. ApJ, 848(2):121, October 2017.

Satoru Takakura, Mario Aguilar, Yoshiki Akiba, Kam Arnold, Carlo Baccigalupi, Darcy Barron, Shawn Beckman, David Boettger, Julian Borrill, Scott Chapman, Yuji Chinone, Ari Cukierman, Anne Ducout, Tucker Elleflot, Josquin Errard, Giulio Fabbian, Takuro Fujino, Nicholas Galitzki, Neil Goeckner-Wald, Nils W. Halverson, Masaya Hasegawa, Kaori Hattori, Masashi Hazumi, Charles Hill, Logan Howe, Yuki Inoue, Andrew H. Jaffe, Oliver Jeong, Daisuke Kaneko, Nobuhiko Katayama, Brian Keating, Reijo Keskitalo, Theodore Kisner, Nicoletta Krachmalnicoff, Akito Kusaka, Adrian T. Lee, David Leon, Lindsay Lowry, Frederick Matsuda, Tomotake Matsumura, Martin Navaroli, Haruki Nishino, Hans Paar, Julien Peloton, Davide Poletti, Giuseppe Puglisi, Christian L. Reichardt, Colin Ross, Praween Siritanasak, Aritoki Suzuki, Osamu Tajima, Sayuri Takatori, and Grant Teply. Performance of a continuously rotating half-wave plate on the POLARBEAR telescope. Journal of Cosmology and Astroparticle Physics, 2017(05):008–008, may 2017.

Davide Poletti, Giulio Fabbian, Maude Le Jeune, Julien Peloton, Kam Arnold, Carlo Baccigalupi, Darcy Barron, Shawn Beckman, Julian Borrill, Scott Chapman, Yuji Chinone, Ari

Cukierman, Anne Ducout, Tucker Elleflot, Josquin Errard, Stephen Feeney, Neil Goeckner-Wald, John Groh, Grantland Hall, Masaya Hasegawa, Masashi Hazumi, Charles Hill, Logan Howe, Yuki Inoue, Andrew H. Jaffe, Oliver Jeong, Nobuhiko Katayama, Brian Keating, Reijo Keskitalo, Theodore Kisner, Akito Kusaka, Adrian T. Lee, David Leon, Eric Linder, Lindsay Lowry, Frederick Matsuda, Martin Navaroli, Hans Paar, Giuseppe Puglisi, Christian L. Reichardt, Colin Ross, Praween Siritanasak, Nathan Stebor, Bryan Steinbach, Radek Stompor, Aritoki Suzuki, Osamu Tajima, Grant Teply, and Nathan Whitehorn. Making maps of cosmic microwave background polarization for B-mode studies: the POLARBEAR example. A&A, 600:A60, April 2017.

David Leon, Jonathan Kaufman, Brian Keating, and Matthew Mewes. The cosmic microwave background and pseudo-Nambu-Goldstone bosons: Searching for Lorentz violations in the cosmos. Modern Physics Letters A, 32(2):1730002, January 2017.

A. Suzuki, P. Ade, Y. Akiba, C. Aleman, K. Arnold, C. Baccigalupi, B. Barch, D. Barron, A. Bender, D. Boettger, J. Borrill, S. Chapman, Y. Chinone, A. Cukierman, M. Dobbs, A. Ducout, R. Dunner, T. Elleflot, J. Errard, G. Fabbian, S. Feeney, C. Feng, T. Fujino, G. Fuller, A. Gilbert, N. Goeckner-Wald, J. Groh, T. De Haan, G. Hall, N. Halverson, T. Hamada, M. Hasegawa, K. Hattori, M. Hazumi, C. Hill, W. Holzapfel, Y. Hori, L. Howe, Y. Inoue, F. Irie, G. Jaehnig, A. Jaffe, O. Jeong, N. Katayama, J. Kaufman, K. Kazemzadeh, B. Keating, Z. Kermish, R. Keskitalo, T. Kisner, A. Kusaka, M. Le Jeune, A. Lee, D. Leon, E. Linder, L. Lowry, F. Matsuda, T. Matsumura, N. Miller, K. Mizukami, J. Montgomery, M. Navaroli, H. Nishino, J. Peloton, D. Poletti, G. Puglisi, G. Rebeiz, C. Raum, C. Reichardt, P. Richards, C. Ross, K. Rotermund, Y. Segawa, B. Sherwin, I. Shirley, P. Siritanasak, N. Stebor, R. Stompor, J. Suzuki, O. Tajima, S. Takada, S. Takakura, S. Takatori, A. Tikhomirov, T. Tomaru, B. Westbrook, N. Whitehorn, T. Yamashita, A. Zahn, and O. Zahn. The Polarbear-2 and the Simons Array Experiments. Journal of Low Temperature Physics, 184(3-4):805–810, August 2016.

Y. Inoue, P. Ade, Y. Akiba, C. Aleman, K. Arnold, C. Baccigalupi, B. Barch, D. Barron, A. Bender, D. Boettger, J. Borrill, S. Chapman, Y. Chinone, A. Cukierman, T. de Haan, M. A. Dobbs, A. Ducout, R. Dünner, T. Elleflot, J. Errard, G. Fabbian, S. Feeney, C. Feng, G. Fuller, A. J. Gilbert, N. Goeckner-Wald, J. Groh, G. Hall, N. Halverson, T. Hamada, M. Hasegawa, K. Hattori, M. Hazumi, C. Hill, W. L. Holzapfel, Y. Hori, L. Howe, F. Irie, G. Jaehnig, A. Jaffe, O. Jeong, N. Katayama, J. P. Kaufman, K. Kazemzadeh, B. G. Keating, Z. Kermish, R. Keskitalo, T. S. Kisner, A. Kusaka, M. Le Jeune, A. T. Lee, D. Leon, E. V. Linder, L. Lowry, F. Matsuda, T. Matsumura, N. Miller, K. Mizukami, J. Montgomery, M. Navaroli, H. Nishino, H. Paar, J. Peloton, D. Poletti, G. Puglisi, C. R. Raum, G. M. Rebeiz, C. L. Reichardt, P. L. Richards, C. Ross, K. M. Rotermund, Y. Segawa, B. D. Sherwin, I. Shirley, P. Siritanasak, N. Stebor, R. Stompor, J. Suzuki, A. Suzuki, O. Tajima, S. Takada, S. Takatori, G. P. Teply, A. Tikhomirov, T. Tomaru, N. Whitehorn, A. Zahn, and O. Zahn. POLARBEAR-2: an instrument for CMB polarization measurements, volume 9914 of Society of Photo-Optical Instrumentation Engineers (SPIE) Conference Series, page 99141I. 2016.

N. Stebor, P. Ade, Y. Akiba, C. Aleman, K. Arnold, C. Baccigalupi, B. Barch, D. Barron,

S. Beckman, A. Bender, D. Boettger, J. Borrill, S. Chapman, Y. Chinone, A. Cukierman, T. de Haan, M. Dobbs, A. Ducout, R. Dunner, T. Elleflot, J. Errard, G. Fabbian, S. Feeney, C. Feng, T. Fujino, G. Fuller, A. J. Gilbert, N. Goeckner-Wald, J. Groh, G. Hall, N. Halverson, T. Hamada, M. Hasegawa, K. Hattori, M. Hazumi, C. Hill, W. L. Holzapfel, Y. Hori, L. Howe, Y. Inoue, F. Irie, G. Jaehnig, A. Jaffe, O. Jeong, N. Katayama, J. P. Kaufman, K. Kazemzadeh, B. G. Keating, Z. Kermish, R. Keskitalo, T. Kisner, A. Kusaka, M. Le Jeune, A. T. Lee, D. Leon, E. V. Linder, L. Lowry, F. Matsuda, T. Matsumura, N. Miller, J. Montgomery, M. Navaroli, H. Nishino, H. Paar, J. Peloton, D. Poletti, G. Puglisi, C. R. Raum, G. M. Rebeiz, C. L. Reichardt, P. L. Richards, C. Ross, K. M. Rotermund, Y. Segawa, B. D. Sherwin, I. Shirley, P. Siritanasak, L. Steinmetz, R. Stompor, A. Suzuki, O. Tajima, S. Takada, S. Takatori, G. P. Teply, A. Tikhomirov, T. Tomaru, B. Westbrook, N. Whitehorn, A. Zahn, and O. Zahn. The Simons Array CMB polarization experiment, volume 9914 of Society of Photo-Optical Instrumentation Engineers (SPIE) Conference Series, page 99141H. 2016.

Jonathan Kaufman, David Leon, and Brian Keating. Using the Crab Nebula as a high precision calibrator for cosmic microwave background polarimeters. International Journal of Modern Physics D, 25(11):1640008, March 2016.

Peter A. R. Ade, Kam Arnold, Matt Atlas, Carlo Baccigalupi, Darcy Barron, David Boettger, Julian Borrill, Scott Chapman, Yuji Chinone, Ari Cukierman, Matt Dobbs, Anne Ducout, Rolando Dunner, Tucker Elleflot, Josquin Errard, Giulio Fabbian, Stephen Feeney, Chang Feng, Adam Gilbert, Neil Goeckner-Wald, John Groh, Grantland Hall, Nils W. Halverson, Masaya Hasegawa, Kaori Hattori, Masashi Hazumi, Charles Hill, William L. Holzapfel, Yasuto Hori, Logan Howe, Yuki Inoue, Gregory C. Jaehnig, Andrew H. Jaffe, Oliver Jeong, Nobuhiko Katayama, Jonathan P. Kaufman, Brian Keating, Zigmund Kermish, Reijo Keskitalo, Theodore Kisner, Akito Kusaka, Maude Le Jeune, Adrian T. Lee, Erik M. Leitch, David Leon, Yun Li, Eric Linder, Lindsay Lowry, Frederick Matsuda, Tomotake Matsumura, Nathan Miller, Josh Montgomery, Michael J. Myers, Martin Navaroli, Haruki Nishino, Takahiro Okamura, Hans Paar, Julien Peloton, Levon Pogosian, Davide Poletti, Giuseppe Puglisi, Christopher Raum, Gabriel Rebeiz, Christian L. Reichardt, Paul L. Richards, Colin Ross, Kaja M. Rotermund, David E. Schenck, Blake D. Sherwin, Meir Shimon, Ian Shirley, Praween Siritanasak, Graeme Smecher, Nathan Stebor, Bryan Steinbach, Aritoki Suzuki, Jun-ichi Suzuki, Osamu Tajima, Satoru Takakura, Alexei Tikhomirov, Takayuki Tomaru, Nathan Whitehorn, Brandon Wilson, Amit Yadav, Alex Zahn, and Oliver Zahn. Polarbear constraints on cosmic birefringence and primordial magnetic fields. Phys. Rev. D, 92:123509, Dec 2015.

J. Errard, P. A. R. Ade, Y. Akiba, K. Arnold, M. Atlas, C. Baccigalupi, D. Barron, D. Boettger, J. Borrill, S. Chapman, Y. Chinone, A. Cukierman, J. Delabrouille, M. Dobbs, A. Ducout, T. Elleflot, G. Fabbian, C. Feng, S. Feeney, A. Gilbert, N. Goeckner-Wald, N. W. Halverson, M. Hasegawa, K. Hattori, M. Hazumi, C. Hill, W. L. Holzapfel, Y. Hori, Y. Inoue, G. C. Jaehnig, A. H. Jaffe, O. Jeong, N. Katayama, J. Kaufman, B. Keating, Z. Kermish, R. Keskitalo, T. Kisner, M. Le Jeune, A. T. Lee, E. M. Leitch, D. Leon, E. Linder, F. Matsuda, T. Matsumura, N. J. Miller, M. J. Myers, M. Navaroli, H. Nishino, T. Okamura, H. Paar, J. Peloton, D. Poletti, G. Puglisi, G. Rebeiz, C. L. Reichardt, P. L. Richards, C. Ross, K. M. Rotermund, D. E. Schenck, B. D. Sherwin, P. Siritanasak, G. Smecher, N. Stebor, B. Steinbach, R. Stompor, A. Suzuki, O. Tajima, S. Takakura, A. Tikhomirov, T. Tomaru,

N. Whitehorn, B. Wilson, A. Yadav, and O. Zahn. MODELING ATMOSPHERIC EMISSION FOR CMB GROUND-BASED OBSERVATIONS. The Astrophysical Journal, 809(1):63, aug 2015.

ABSTRACT OF THE DISSERTATION

Using Cosmological Observations to Search for New Physics and Study the Structure of the Universe

by

David Leon

Doctor of Philosophy in Physics

University of California San Diego, 2020

Professor Brian Keating, Chair

Cosmological observations have great potential to glean information about fundamental physics. The large distances and long time scales of distant sources of light allow us to leverage the vastness of the universe to search for tiny deviations to the currently accepted physical laws. This thesis will explore a number of ways that cosmological observations can help us search for new physics and learn about the evolution of the cosmos.

We will examine the dynamics of pseudo-Nambu-Goldstone bosons (PNGBs) and their behavior throughout cosmic history. Quantum scalar fields under the umbrella of PNGBs have been proposed to answer unsolved questions in physics, and they share the characteristic that they could be detected through Lorentz-violating polarization rotation of

photons travelling over cosmological distances.

We will then move to a general framework for studying potential Lorentz-violating physics called the Standard Model Extension (SME), and use the framework to place limits on coefficients of the SME. Using wideband optical polarimetry of two active galactic nuclei we demonstrate the ability to place constraints with small aperture telescopes and show how combining multiple simultaneous measurements in adjacent frequency bands increase the constraining power of such observations.

We then probe the evolution of the large scale structure of the universe with a measument of the gravitational lensing deflection power spectrum using measurements of the polarization of the cosmic microwave background (CMB) taken from two years of observations with the POLARBEAR experiment.

And finally we will see how the CMB and other cosmological observations constrain the shape of the primordial power spectrum of scalar perturbations through a likelihood analysis that takes advantage of second order effects in the perturbative expansion of the gravitational metric.

Chapter 1

Introduction

The universe is well described by two incredibly successful physical theories: the standard model of particle physics and the general theory of relativity. One governs the realm of fundamental forces and particles while the other governs the relationship between energy, momentum, and spacetime. While they are the best descriptions of our physical world we have so far, there are still deep questions that remain unanswered.

Our understanding of quantum mechanics and gravity work well in their respective regimes, but in the combined limits of large energy density and small length scales we lack a way to bring these two theories together. One of the goals of this work is to search for signs of an underlying Theory of Everything that may manifest itself as tiny violations of the known laws of physics.

We also know that our observations of the most distant parts of our universe are also observations of the earliest cosmic times. Any information we can extract from these earliest times give us the best chance at understanding how the cosmos was formed. This work also aims to illustrate how the CMB, the earliest light we can observe, helps us understand the initial conditions of the universe and the distribution of matter and energy in the present day.

1.1 Testing Special Relativity

The theory of special relativity is foundational to our understanding of electromagnetism. This symmetry of our physical laws manifests itself in many ways, perhaps none more well known than the fact that the speed of light is the same in any inertial reference frame. In addition, Lorentz symmetry also requires that electromagetic waves propagating in empty space maintain the polarization states of their electric and magnetic fields. Under this symmetry linearly polarized light will maintain its polarization angle, and linear and circular polarizations will not mix.

But if our theories of gravity and quantum mechanics are only effective theories of some more fundamental Theory of Everything, then there may be fields or interactions that are simply very hard to detect in the comparatively low energies of the aging universe. It might be the case that the familiar symmetries of our physical theories break down at high energies, and deviations from those symmetries at everyday laboratory scales are undetectable. But if we allow photons to propagate across distances comparable to the size of the observable universe, then any small deviations from Lorentz symmetry may be able to accumulate into an observable signal. This is the driving motivation behind using photons of cosmological origin to search for Lorentz violating physics.

1.1.1 The Chern-Simons Term

We will examine how the Chern-Simons term is one way that we could observe Lorentz violating effects, and in particular birefringence. First let's acquaint ourselves with classical electrodynamics with a 4-vector potential A_μ, current density J_μ, and electromagnetic field strength tensor $F_{\mu\nu} = \partial_\mu A_\nu - \partial_\nu A_\mu$. In classical field theory the electromagnetic Lagrangian is

$$\mathcal{L} = -\frac{1}{4} F_{\mu\nu} F^{\mu\nu} - A_\mu J^\mu. \tag{1.1}$$

Application of the Euler-Lagrange equations of motion with coordinates A_μ and momenta $\partial_\mu A_\nu$ result in the equations of motion

$$\partial_\mu F^{\mu\nu} = J^\nu, \tag{1.2}$$

which constitute two of the four Maxwell equations of classical electromagnetism.

But certain proposed extensions to the standard model hypothesize fields that introduce a Lagrangian term called the Chern-Simons term into the electromagnetic Lagrangian

$$\mathcal{L} = -\frac{1}{4}F_{\mu\nu}F^{\mu\nu} - A_\mu J^\mu - \frac{\theta}{2}F_{\mu\nu}\tilde{F}^{\mu\nu}, \tag{1.3}$$

where θ is a dynamical field, not simply a constant. This results in new equations of motion

$$\partial_\mu \left(F^{\mu\nu} + \theta\epsilon^{\mu\nu\rho\sigma}F_{\rho\sigma}\right) = J^\nu. \tag{1.4}$$

In the case of a θ with temporal or spatial variation, this induces a precession of the polarization angle in a linearly polarized electromagnetic wave, in violation of Lorentz symmetry. The questions of why a field like θ might exist, how it relates to the evolution of the universe, and how we might detect its presence are the subject of Chapter 2.

1.1.2 The Standard Model Extension

One way we can search for Lorentz violating physics is to propose a theory, perhaps with new particles or fields, then solve for the dynamics of that theory and use it to search for a particular experimental signal. But this approach requires us to specify a model and if our model is wrong then designing an experiment to test a certain model may miss effects that appear in a different theory. To get around this problem, the framework known as the Standard Model Extension (SME) takes a model independent approach and instead utilizes an effective field theory approach to search for Lorentz violations.

Rather than posit the existence of an undiscovered field as in the previous section, the SME considers all possible Lorentz violating Lagrangian terms that otherwise respect the other symmetries of the standard model. These new Lagrangian terms are parameterized by coefficients that can represent the low energy effective field theory manifestation of some underlying theory at higher energy. As we are concerned with photons propagating over cosmological distances, we use the pure electromagnetic sector of the SME in our searches for Lorentz violating effects. This Lagrangian has the form

$$\mathcal{L} = -\frac{1}{4}F_{\mu\nu}F^{\mu\nu} + \frac{1}{2}\epsilon^{\kappa\lambda\mu\nu}A_\lambda \left(\hat{k}_{AF}\right)_\kappa F_{\mu\nu} - \frac{1}{4}F_{\kappa\lambda}\left(\hat{k}_F\right)^{\kappa\lambda\mu\nu} F_{\mu\nu}, \tag{1.5}$$

where the operators $\hat{k}_{AF}$ and $\hat{k}_F$ contain parametrizations for the CPT-odd and CPT-even Lorentz violating terms respectively.[5] When dealing with observations on the spherical surface of the sky, it is more useful to reparameterize these Lorentz violating terms in a spherical harmonic decomposition. This results in four Lorentz violating quantities

$$\varsigma^0 = \sum_{djm} \omega^{d-4}\ {}_0Y_{jm}(\hat{\boldsymbol{n}}) k^{(d)}_{(I)jm}, \tag{1.6}$$

$$\varsigma^1 \pm i\varsigma^2 = \sum_{djm} \omega^{d-4}\ {}_{\pm 2}Y_{jm}(\hat{\boldsymbol{n}}) \left(k^{(d)}_{(E)jm} \mp i k^{(d)}_{(B)jm}\right), \tag{1.7}$$

$$\varsigma^3 = \sum_{djm} \omega^{d-4}\ {}_0Y_{jm}(\hat{\boldsymbol{n}}) k^{(d)}_{(V)jm}. \tag{1.8}$$

Nonzero ς^i can induce a number of different Lorentz violating effects in freely propagating photons including a modification of the photon dispersion relation, which becomes

$$k = \omega\left[1 + \varsigma^0 \mp \sqrt{(\varsigma^1)^2 + (\varsigma^2)^2 + (\varsigma^3)^2}\right]. \tag{1.9}$$

This can produce a frequency dependent speed of light, phase delay between two orthogonal polarizations of light, rotation of linearly polarized light, and mixing between linear and circular polarization. In Chapter 3 we apply the SME to optical polarimetric observations in

order to constrain the size of the SME coefficients $k^{(d)}_{(x)jm}$

1.2 The Evolution of the Universe

When it comes to photons freely propagating over cosmological distances, there is no better source to study than the CMB. While studies of the CMB extract much information from its perturbations, one of the most important and distinctive features of the CMB is its extreme uniformity. The CMB consists of the photons emitted from the surface of last scattering as the universe cooled enough to the point at which hydrogen atoms began to form and allowed photons to free stream through space. And although CMB photons reaching us from opposite ends of the night sky were out of causal contact when the universe formed, they have the same blackbody distribution as the rest of the CMB, deviating only at the order of 1 part in 10^5. We attribute this remarkable fact to inflation, but in order to appreciate small perturbations in an otherwise uniform cosmos, we will review what general relativity tells us about the evolution of the universe.

1.2.1 The Friedmann Equations and Metric Perturbations

Einstein's theory of general relativity describes space and time in terms of a metric. Spacetime acts like a fabric that is bent and curved by energy in the universe, and in turn bends the paths of particles that travel through it. The metric tensor $g_{\mu\nu}$, which describes the shape of spacetime, and the stress-energy tensor $T_{\mu\nu}$, which describes the energy and momentum content of spacetime, appear in the Einstein field equations,

$$R_{\mu\nu} - \frac{1}{2}Rg_{\mu\nu} = \frac{8\pi G}{c^4}T_{\mu\nu}, \tag{1.10}$$

a set of nonlinear differential equations. In general, solutions of these equations are difficult to find, but observations of our universe tell us that to a surprising degree it is homogenous

and isotropic at large scales. This empirical observation allows us to greatly simplify the equations of general relativity and the form of the metric to one that is parameterized by a scale factor $a(t)$ and a curvature k.

The metric is typically expressed in terms of the infinitescimal line element

$$ds^2 = g_{\mu\nu} dx^\mu dx^\nu. \tag{1.11}$$

In cartesian coordinates of a laboratory setting this would be

$$ds^2 = -dt^2 + dx^2 + dy^2 + dz^2, \tag{1.12}$$

and in the metric of a homogenous and isotropic universe this would be expressed in spherical coordinates as

$$ds^2 = -dt^2 + a^2(t) \left[dr^2 + \chi_k^2(r)(d\theta^2 + \sin^2\theta d\phi^2) \right], \tag{1.13}$$

where the distance measure $\chi_k(r)$ depends on whether the metric is open, closed or flat. This simple parametrization leads to the Friedman equations, a set of differential equations relating a, k, and the energy density ρ that allows us to describe the evolution of the universe for a given type of energy content.

But of course the universe is not perfectly homogenous and isotropic, otherwise we would not be here to observe it. The mostly uniform universe allows us to apply perturbation theory to the gravitational metric and write it as

$$g_{\mu\nu} = \eta_{\mu\nu} + h_{\mu\nu}. \tag{1.14}$$

$\eta_{\mu\nu}$ is the metric of static spacetime that is used in special relativity and appears in Equation 1.12. The small variation on the background metric, $h_{\mu\nu}$, is what appears in the perturbative equations of general relativity. This transforms the Einstein field equations into a set of linear, second order differential equations of $h_{\mu\nu}$. One important consequence of this

perturbative approach is that at first order $h_{\mu\nu}$ can be decomposed into independent scalar, vector, and tensor components. Of these, the scalar and tensor components are of particular importance in studies of the CMB.

The components of $h_{\mu\nu}$ at a given time can be conceptualized as spatially varying fields, but equivalently they can be thought of in terms of their power spectra. A Fourier transform of fields in (x, y, z) coordinates can be turned into a function of (k_x, k_y, k_z), and in an isotropic universe these power spectra can be described in terms of the wavenumber magnitude k. The power spectra of scalar and tensor perturbations can in general be denoted as the functions $P_S(k)$ and $P_T(k)$, but empirical observations of the early universe show us that to a good approximation the scalar power spectrum at scales relevant to the CMB has a very simple form,

$$P_S(k) = A_S \left(\frac{k}{k_0}\right)^{n_s - 1}. \tag{1.15}$$

And while searches are still ongoing for evidence of tensor perturbations at CMB scales, the theory of inflation predicts that the tensor power spectrum should have a similar form,

$$P_T(k) = A_T \left(\frac{k}{k_0}\right)^{n_t}. \tag{1.16}$$

1.2.2 The Cosmic Microwave Background

Information about the scalar and tensor power spectra at the largest scales is embedded in the angular power spectra of the CMB. In the largely uniform early universe, the formation of the CMB at the surface of last scattering meant the emission of a background of photons at a uniform temperature that largely have traveled through space unimpeded until we observe them. Observations of the CMB across the sky have confirmed that to very high precision it is a uniform blackbody at a temperature of approximately 2.7 K visible from everywhere in space.

But the CMB is not perfectly uniform. Small variations from the mean temperature

can be described as a field across the sky, $T(\hat{n})$, where $\hat{n}$ denotes a direction on the sky. Similar to the description of the primordial scalar and tensor perturbations in terms of power spectra, we can also describe the temperature variation in terms of a power spectrum. The temperature variations are well described by the spherical harmonic decomposition

$$T(\hat{n}) = \sum_{\ell m} a_{\ell m} Y_{\ell m}(\hat{n}), \tag{1.17}$$

where $Y_{\ell m}$ are the spherical harmonic functions and coefficients $a_{\ell m}$ are independent Gaussian random variables with mean zero and variance C_ℓ. The set of variances C_ℓ constitute the CMB temperature angular power spectrum.

The origin of the temperature power spectrum is closely related to the power spectra of the primordial metric perturbations, in particular the scalar perturbations, and observations of the CMB temperature power spectrum can constrain the amplitude A_S and spectral index n_s of the scalar power spectrum. But the CMB has more information than simply temperature variations. At the surface of last scattering, the anisotropy of Compton scattering generated net polarization in the CMB. This is due to the fact that a local temperature quadrupole in the plane of the CMB generates a net linear polarization signal that we can detect.

Now since polarization is a directional quantity, it must be parameterized in terms of components. Anyone familiar with laboratory experiments with polarized light will be familiar with the stokes Q and U parametrization, but a more useful parametrization for extracting cosmological information from CMB experiments is the definition of E- and B-modes respectively as the curl-free and divergence free components of CMB polarization. The Compton scattering at the formation of the CMB only generates E-mode polarization, and as such the CMB E-mode power spectrum is much larger than the B-mode power spectrum. Potential sources for B-modes may include primordial tensor perturbations among other things. A comparison of the relative sizes of the T, E and B power spectra are shown in Figure 1.1.

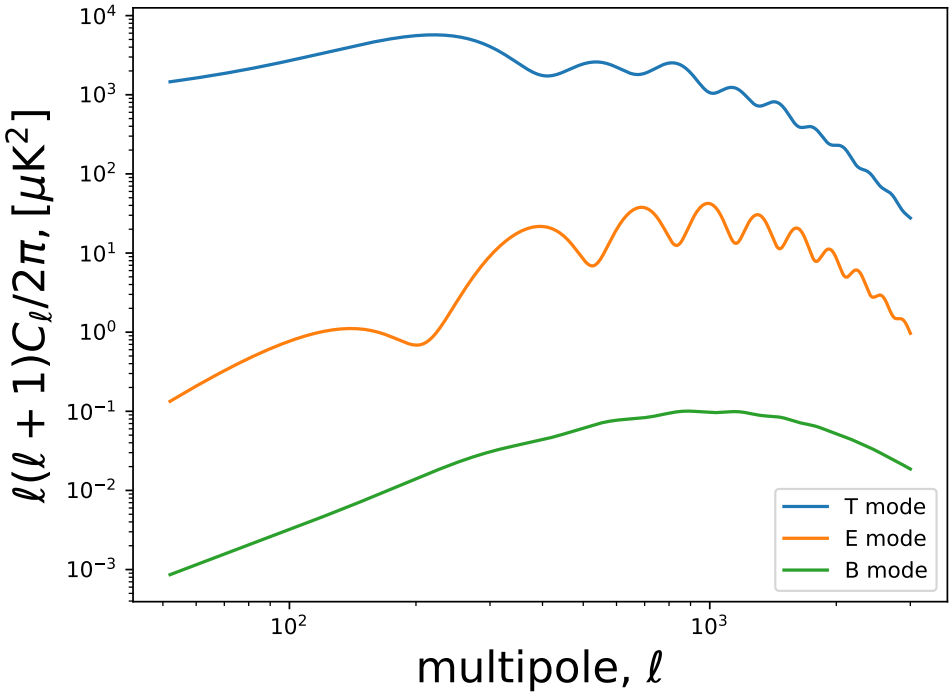

Figure 1.1: CMB temperature and polarization angular power spectra

1.2.3 Reconstruction of Gravitational Lensing

We saw how the temperature power spectrum C_ℓ can be extracted from the temperature variation map $T(\hat{n})$ under the assumption that CMB photons travel in unperturbed straight paths from the surface of last scattering to us. But if the paths of CMB photons is perturbed then the coefficients $a_{\ell m}$ of the spherical harmonic decomposition will not be independently distributed Gaussian random variables. If instead a photon coming from direction $\hat{n}$ has been deflected by a small amount $\vec{d}(\hat{n})$ then we are actually observing a temperature map $\tilde{T}(\hat{n} + \vec{d}(\hat{n}))$. For small deflections this can be expanded to first order,

$$T(\hat{n}) = \tilde{T}(\hat{n} + \vec{d}(\hat{n})) = \tilde{T}(\hat{n}) + \vec{d}(\hat{n}) \cdot \vec{\nabla} T(\hat{n}). \tag{1.18}$$

We use $T(\hat{n})$ to denote the lensed temperature map and $\tilde{T}(\hat{n})$ to denote the unlensed temperature map.

In fact gravitational lensing by large scale structure in the late universe does deflect CMB photons in this way. We can describe the angular distribution of this structure with the lensing potential $\phi(\hat{n})$ which is related to the lensing deflection,

$$\vec{d}(\hat{n}) = \vec{\nabla}\phi(\hat{n}). \tag{1.19}$$

This lensing distortion by large scale structure means that information about the lensing potential ϕ is embedded in the lensed CMB power spectra.

We can see this by first considering a flat sky approximation to the CMB. Instead of a spherical harmonic decomposition into coefficients $a_{\ell m}$, we can consider $T(\hat{n})$ on a small section of the sky and its corresponding Fourier mode vector l,

$$T(l) = \int d^2\hat{n} T(\hat{n}) e^{i\hat{n}\cdot l}. \tag{1.20}$$

The statistical isotropy of the CMB means that the temperature mode has the statistical properties

$$\langle T(l) \rangle = 0, \tag{1.21}$$

$$\langle T^*(l) T(l') \rangle = \delta(l - l') C_l. \tag{1.22}$$

But when the CMB is gravitationally lensed, the equivalent of Equation 1.18 in mode space states

$$T(l) = \tilde{T}(l) - \int \frac{d^2 l'}{(2\pi)^2} l' \cdot (l - l') \tilde{T}(l') \phi(l - l'). \tag{1.23}$$

The outcome of this result is that temperature modes at different multipoles now do have a nonzero correlation which is proportional to the lensing potential,

$$\langle T^*(l) T(L - l) \rangle \propto \phi(L). \tag{1.24}$$

This is the basis of using CMB maps to reconstruct gravitational lensing by large scale structure. While this example used the CMB temperature, we can in fact use off-diagonal correlations between any two CMB maps, T, E, or B, to reconstruct the lensing potential. In Chapter 4 we use CMB polarization measured by POLARBEAR to estimate the lensing deflection power spectrum of the deflection field $\vec{d}(\hat{n})$.

1.2.4 Second Order Metric Perturbations

Finally we will make one more note about the scalar and tensor power spectra discussed in this section. Expanding the gravitational metric $g_{\mu\nu} = \eta_{\mu\nu} + h_{\mu\nu}$ and working to first order in $h_{\mu\nu}$ is generally sufficient to capture most important aspects of cosmology on the largest scales. In this approximation the scalar and tensor perturbations remain independent, however at second order in this expansion, this is no longer the case. The tensor power spectrum recieves a contribution from the scalar power spectrum such that in the absence of primordial tensor perturbations at first order,

$$P_T(k) \sim P_S^2(k). \tag{1.25}$$

As a second order term this would have negligible importance in most cases, but since we have yet to measure $P_T(k)$ at CMB scales, we can use this relationship to place tight constraints on the shape of $P_S(k)$ at scales even beyond the CMB. In Chapter 5 we shrink the parameter space for the running of n_s and the running of running of n_s using this second order relationship.

Chapter 2

The Cosmic Microwave Background and Pseudo-Nambu-Goldstone Bosons: Searching for Lorentz Violations in the Cosmos

One of the most powerful probes of new physics is the polarized Cosmic Microwave Background (CMB). The detection of a nonzero polarization angle rotation between the CMB surface of last scattering and today could provide evidence of Lorentz-violating physics. The purpose of this paper is twofold. First we review one popular mechanism for polarization rotation of CMB photons: the pseudo-Nambu-Goldstone boson. Second, we propose a method to use the POLARBEAR experiment to constrain Lorentz-violating physics in the context of the Standard-Model Extension, a framework to standardize a large class of potential Lorentz-violating terms in particle physics.

2.1 Introduction

The principle of Lorentz invariance undergirds our two most fundamental theories of physics: the standard model of particle physics and general relativity. While these theories have been extraordinarily successful at describing nature, we expect new physics to emerge at high energies. Since we have limited ability to directly probe the regimes where both quantum mechanics and relativity dominate, we can instead search for small deviations in our low-energy theories such as a departure from Lorentz symmetry.

One promising way to search for Lorentz violations is to study linearly polarized light as it propagates through space. From rotational symmetry, it is expected that the polarization plane of a linearly polarized photon should not change as it propagates through empty space, so any rotation of the polarization would indicate some physical interaction that violates Lorentz invariance.

Although there are a number of potential theories that could cause such a rotation, one popular mechanism for achieving this effect is the introduction of an additional scalar field to the standard model. The pseudo-Nambu-Goldstone boson (PNGB) has a number of attractive qualities, including the ability to conserve an otherwise broken global symmetry and to naturally explain the connection between symmetry-breaking effects over many orders of magnitude in energy. It is also a potential candidate to account for the observed dark energy or dark matter densities. Since PNGBs generically introduce a Lorentz-violating polarization angle rotation via Chern-Simons coupling to electromagnetism, we also have a promising avenue to search for their existence.[6],[7],[8],[9],[10]

Of course this is only one possible mechanism so we should also consider ways to classify more general Lorentz violations, which is the aim of the Standard-Model Extension (SME) framework. In particular the CMB is an excellent probe of Lorentz violations because small effects can accumulate over cosmological distances. Using observations from the POLARBEAR experiment[11] we propose a method to constrain a subset of the SME parameters using the three CMB patches observed by POLARBEAR.

The paper is organized as follows. Sections 2.2 through 2.8 are a brief review of a general PNGB and its evolution through the universe, including specific examples like the QCD axion and quintessence; a candidate for dark energy. Sections 2.9 through 2.11 deal with the SME and show how cosmic polarization rotation angle measurements can be used to constrain SME parameters.

2.2 Energy Scales in Field Theory

There is a general heuristic in field theory that can be expressed in imprecise terms as: "mass terms in the action correspond to energy scales of the relevant physics."

This statement is tantamount to dimensional analysis. When using natural units that set $c = 1$ and $\hbar = 1$ any quantity can be written in terms of powers of a single unit, usually in terms of eV, sometimes in terms of mass. In the path integral approach to quantum mechanics, the action appears in an exponential e^{iS} so dimensional analysis tells us that the action must be dimensionless. We can then examine the definiton of the action

$$S = \int d^4x \mathcal{L}(\phi). \tag{2.1}$$

From this one can conclude that, in 4D space, the Lagrangian has units of [distance]$^{-4}$, or equivalently [mass]^4, in order to make the action unitless. Quantum fields also have mass dimensions. For example, in order for the kinetic term of the scalar field, $\frac{1}{2}\partial_\mu\phi\partial^\mu\phi$, to have dimension 4, and noting that a derivative has mass dimension 1, then it is necessary for the field ϕ to have dimension 1. A consequence of this is that a term like ϕ^2 has dimension 2 and therefore needs a dimensionful coupling in order to be in the Lagrangian, for example: $m^2\phi^2$, where m is a constant with mass dimension 1.

A more complicated example is the Chern-Simons term between a scalar field and a field strength tensor: $\phi F^{\mu\nu}\widetilde{F}_{\mu\nu}$. In electromagnetism the field strength tensor $F_{\mu\nu}$ is

constructed from derivatives and the vector potential (mass dimension 1)

$$F_{\mu\nu} = \partial_\mu A_\nu - \partial_\nu A_\mu. \tag{2.2}$$

Therefore $F_{\mu\nu}$ has dimension 2, and the overall Chern-Simons term has dimension 5, so it must be accompanied by a coupling of dimension -1. Therefore something like a constant $1/M$ for a Lagrangian term of the form

$$\frac{1}{M}\phi F^{\mu\nu}\widetilde{F}_{\mu\nu} \tag{2.3}$$

would be a candidate ansatz. Considering a theory that contains terms with dimensionful constants, a reasonable question to ask is whether the value of that constant is an arbitrary parameter of the theory or whether it traces new physics at roughly that scale, which is not yet understood. Take for example the masses of the W and Z bosons. They are not arbitrary parameters but they come from electroweak-symmetry breaking. Furthermore both of these particles and the Higgs boson all have masses of around 100 GeV, which is on the order of the electroweak scale ~ 200 GeV.

Similarly the pion of mass ~ 130 MeV and the proton/neutron masses ~ 1000 MeV are all around the same order of magnitude as the QCD scale ~ 200 MeV.

This reasoning also leads us to believe there is some, as yet unknown, physics at the Planck scale since general relativity has a dimensionful parameter of its own: $G = \frac{1}{M_P^2}$.

This energy-scale approach is especially relevant to cosmology because it deals with the evolution of the universe, which spans some 30 orders of magnitude in temperature, with the temperature going down as the universe ages. Even an order of magnitude approach to cosmological fields should lend us considerable insight. So with this heuristic in mind, we now take a look at the PNGB.

2.3 Mass of the Pseudo-Nambu-Goldstone Boson

If a scalar field theory with multiple degrees of freedom is invariant under some symmetry, that symmetry can be spontaneously broken via the Higgs mechanism. To understand how this happens, first consider an example with a single scalar field.

2.3.1 Spontaneous Symmetry Breaking

A single (real) scalar field, which has only one degree of freedom, has a Lagrangian of the form

$$\mathcal{L} = \frac{1}{2}\partial_\mu\phi\partial^\mu\phi - V(\phi). \tag{2.4}$$

The lowest-energy state is simply a constant value $\phi = \phi_0$. The derivative terms are zero for a constant, so its value is determined by the minimum of the potential, $V(\phi_0)$. Including a mass term or even a higher-order quartic term results in a potential

$$V(\phi) = \frac{1}{2}\mu^2\phi^2 + \frac{1}{4}\lambda\phi^4. \tag{2.5}$$

This potential, as well as the full Lagrangian, has a discrete sign symmetry. Replacing ϕ with $-\phi$, the Lagrangian is unchanged because only even powers of ϕ appear. As long as the parameters μ^2 and λ are positive, then the minimum of this potential is $\phi_0 = 0$. However, in field theory it is usually the case that "constants" in the Lagrangian are not truly constant. Due to the process of renormalization, the coupling "constants" can actually depend on energy scale. For example, asymptotic freedom in QCD is related to the statement that the strong fine-structure parameter α_s is large at low energies, but becomes asymptotically smaller at larger energies.

If, at some point in the evolution of the universe, the temperature-dependent parameter $\mu^2 = \mu^2(T)$ changes from a positive value to a negative value, then the minimum of the potential will no longer be $\phi_0 = 0$. Figure 2.1 shows plots of the potential $V(\phi)$ for two cases

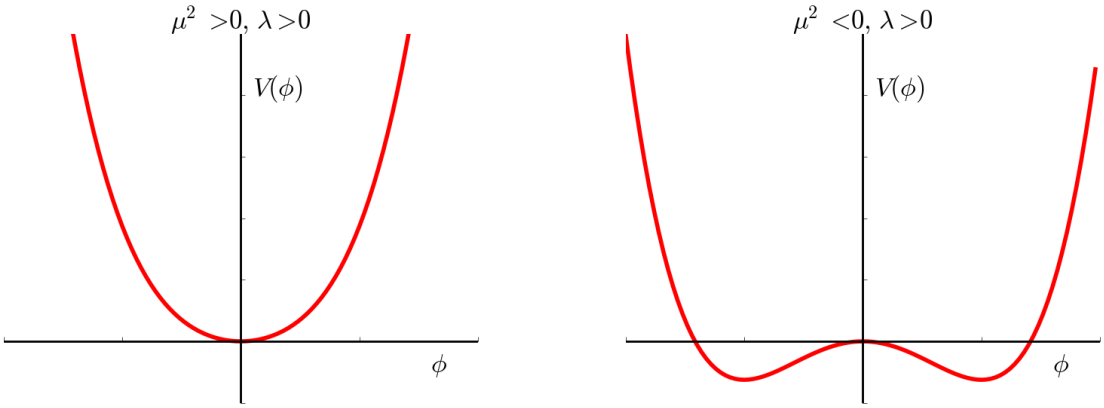

Figure 2.1: Scalar potential for positive and negative mass parameters.

$\mu^2 > 0$ and $\mu^2 < 0$. In the second case there are two minima at

$$\phi = \pm v = \pm\sqrt{\frac{-\mu^2}{\lambda}}. \tag{2.6}$$

After transitioning to $\mu^2 < 0$ the Lagrangian is still symmetric but expansion of the Lagrangian about the ground state, in terms of $\phi - \phi_0$, is no longer symmetric. This phenomemon is called "spontaneous symmetry breaking" because, while the symmetry of the underlying Lagrangian is not broken, symmetry of the ground state *is* broken. In this example the symmetry was discrete but in a model with more degrees of freedom, spontaneous symmetry breaking of a continuous symmetry will occur.

2.3.2 Complex Scalar Field

Next consider a complex scalar field $\psi = \psi_1 + i\psi_2$ with Lagrangian

$$\mathcal{L} = \partial_\mu \psi^\dagger \partial^\mu \psi - V(\psi). \tag{2.7}$$

This field will have a similar potential

$$V(\psi) = \mu^2 \psi^\dagger \psi + \lambda(\psi^\dagger \psi)^2. \tag{2.8}$$

Under a spontaneous-symmetry-breaking event as described above, μ^2 will become negative and the potential will take on the new form

$$V(\psi) = \lambda(\psi^\dagger\psi - v^2)^2. \tag{2.9}$$

In terms of the component fields ψ_1 and ψ_2 this is

$$V(\psi_1, \psi_2) = \lambda(\psi_1^2 + \psi_2^2 - v^2)^2. \tag{2.10}$$

This can be parameterized in terms of two different real scalar fields H and ϕ

$$\psi = He^{i\phi/f}, \tag{2.11}$$

so that

$$\psi_1 = H\cos(\phi/f), \tag{2.12}$$

$$\psi_2 = H\sin(\phi/f). \tag{2.13}$$

This yields a potential only dependent on the longitudinal degree of freedom H, as seen in Figure 2.2

$$V(H, \phi) = V(H) = \lambda(H^2 - v^2)^2. \tag{2.14}$$

This result, where the potential depends on some degrees of freedom but not others, is a general feature of spontaneous-symmetry-breaking events. The degrees of freedom that do not appear in the potential after symmetry breaking are called "Nambu-Goldstone bosons," and the lack of a potential means they are massless by definition. In this example ϕ is the Nambu-Goldstone boson. Additionally they possess shift symmetry in which a change in the

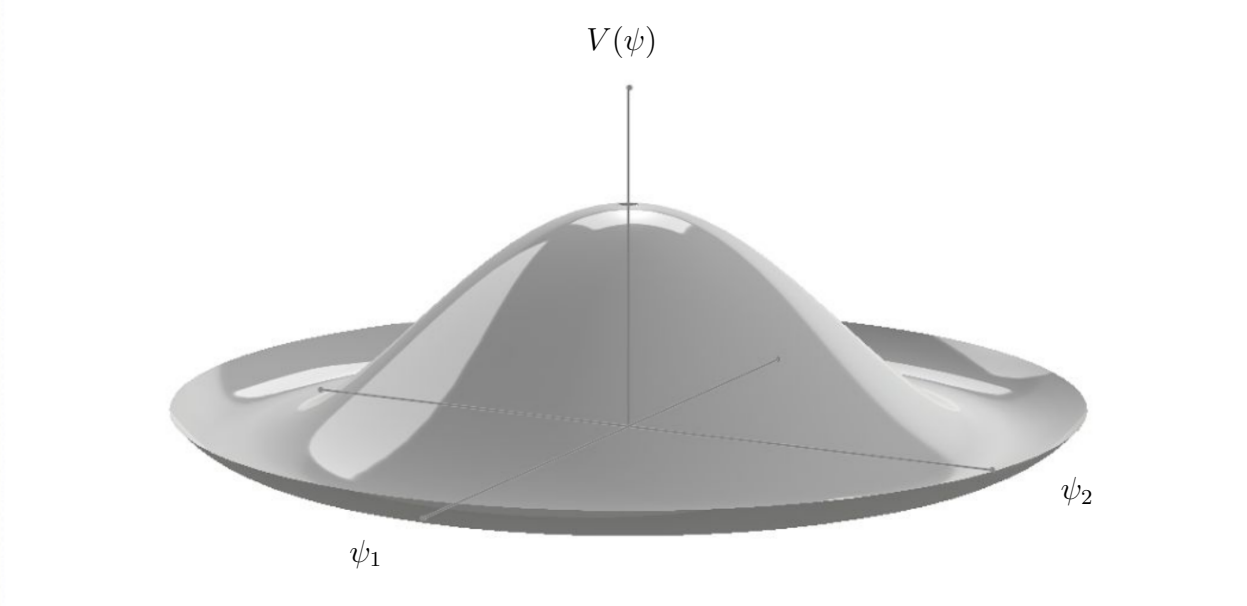

Figure 2.2: Potential of a Nambu-Goldstone boson.

value of ϕ by $2\pi f$ corresponds to the same physical system

$$He^{i\phi/f} \to He^{i(\phi+2\pi f)/f} = He^{i\phi/f}. \tag{2.15}$$

This new parameter f is included because if ϕ is interpreted as a scalar field, dimensional analysis tells us that in order to have it inside the argument of an exponential it must be divided by a coupling with dimension 1. In the spirit of the previous section, it is reasonable to expect that the value of the coupling f will be on the same order of magnitude as the other scales in this scenario like the vacuum expectation value $f \sim v$.

This is the situation with only a scalar field and a spontaneous-symmetry-breaking event. But PNGBs have a second relevant temperature scale when the shift symmetry of ϕ is broken. Next consider a case where the scalar is coupled to either some other field, or collection of fields, or constant term generated by other fields, so that the potential is

$$V(\psi, \Psi) = \lambda(\psi^\dagger\psi - v^2) - \beta\frac{\psi_1}{f}\Psi. \tag{2.16}$$

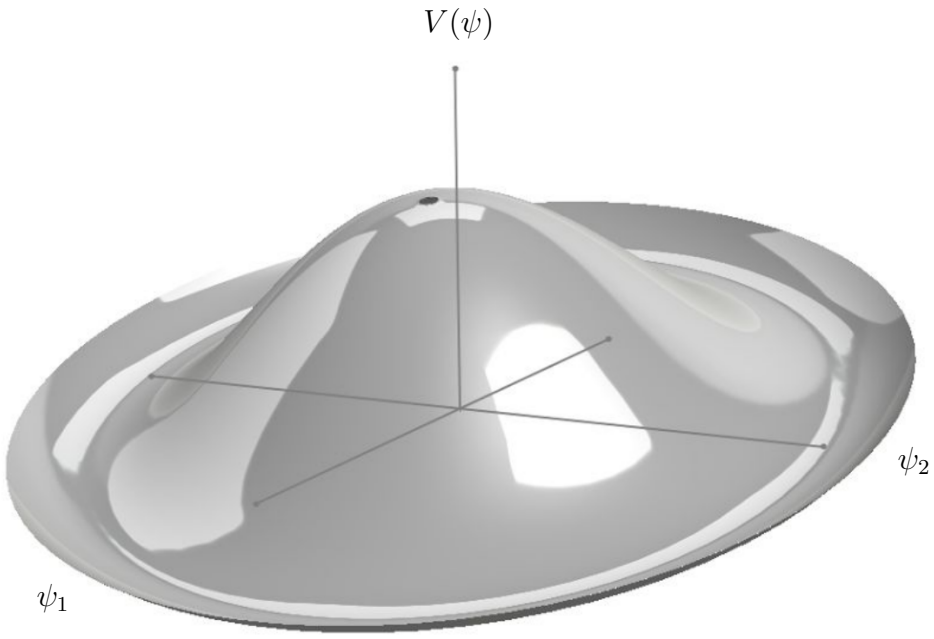

Figure 2.3: Potential of a pseudo-Nambu-Goldstone boson.

Where β is a dimensionless coupling of order unity. In this case, not only will the field undergo spontaneous symmetry breaking, but it will experience explicit symmetry breaking because the $\psi_1\Psi$ term does not respect the U(1) symmetry of ψ: the Lagrangian is not invariant under the global transformation $\psi \to \psi' = e^{i\theta}\psi$.

In this example Ψ represents whatever physics is explicitly breaking the symmetry. This is model dependent, but by dimensional analysis it must have mass dimension 4 regardless of the model. The potential can be seen in Figure 2.3

Now when reparameterizing the ψ field, the potential becomes

$$V(\psi, \Psi) = \lambda(H^2 - v^2) - \frac{\beta}{f} H \cos(\phi/f)\Psi. \tag{2.17}$$

In the low-energy limit, $\phi \ll f$, the quadratic term from the cosine in Eq. (2.12) will dominate and the potential for the PNGB is

$$V(\phi) \approx \frac{\beta}{2f^3} H\phi^2\Psi. \tag{2.18}$$

Additionally, in the low-energy limit, the H field will be near its equilibrium value v, which should be around the same size as f. The potential is therefore

$$V(\phi) \approx \frac{1}{2f^2}\phi^2\Psi. \tag{2.19}$$

Ψ depends on the model, but the fact that Φ is a dimensionful term means it should correspond to the temperature scale of the explicit-symmetry-breaking mechanism. Therefore the potential should generally be on the order of

$$V(\phi) \approx \frac{\Lambda^4}{2f^2}\phi^2, \tag{2.20}$$

where Λ now represents the temperature scale of the explicit symmetry breaking. From this scalar mass term, the mass of the PNGB is

$$m \approx \frac{\Lambda^2}{f}. \tag{2.21}$$

Thus the mass is dependent on the two relevant temperature scales of the PNGB: the spontaneous-symmetry-breaking scale, parameterized by f, and the explicit-symmetry-breaking scale, parameterized by Λ.

2.4 Energy Density of the PNGB

2.4.1 Pre-Oscillations

Now consider the PNGB field in the context of general relativity. The Lagrangian is

$$\mathcal{L} = \frac{1}{2}\sqrt{-g}(g^{\mu\nu}\partial_\mu\phi\partial_\nu\phi - m^2\phi^2). \tag{2.22}$$

Focusing only on a spatially uniform field over cosmological scales in the Friedmann-Lemaˆitre-Robertson-Walker metric, the Euler-Lagrange equation of motion is

$$\frac{d^2\phi}{dt^2} + 3H\frac{d\phi}{dt} + m^2\phi = 0. \tag{2.23}$$

At this point, the PNGB has first gone through spontaneous symmetry breaking and then explicit symmetry breaking. The equation of motion is of the form of a damped simple harmonic oscillator with a damping term $3H$ and angular frequency m. Since H is time dependent the decay envelope will actually be a power law rather than an exponential, but qualitatively the situation is similar. However when the mass first "turns on" at the explicit-symmetry-breaking scale Λ, defined in Eq. (2.20), it is much smaller than H. The mass and Hubble parameters are roughly $H \sim \Lambda$, and $m \sim \frac{\Lambda^2}{f}$, therefore their ratio is small $\frac{m}{H} \sim \frac{\Lambda}{f} \ll 1$. This means the mass can be neglected until H drops to a small enough value. Until then the evolution is governed by

$$\frac{d^2\phi}{dt^2} + 3H\frac{d\phi}{dt} = 0. \tag{2.24}$$

The solution is simply a constant value $\phi = \langle\phi\rangle$. The PNGB sits at the same vacuum expectation value it was given all the way back at spontaneous symmetry breaking. Only once H reaches a small enough value, so that $H \sim m$, do oscillations begin. At this point, the potential energy of the PNGB is about

$$V(\phi) = \frac{1}{2}m^2\phi^2 \sim m^2\alpha^2 f^2. \tag{2.25}$$

Here the vacuum expectation value is $\langle\phi\rangle = \alpha f$, where α is a constant of order 1. This is assumed since the initial value of the field should be the same magnitude as the spontaneous-symmetry-breaking scale $\langle\phi\rangle \sim f$. At symmetry breaking, ϕ takes a value at the bottom of the Higgs potential in the range $-\pi f < \phi < \pi f$. It has no preference for any particular value,

so a random value of α in the range from $-\pi$ to π will give an expectation value on the order of f.

2.4.2 Post-Oscillations

Starting from the initial value of $\phi \sim m^2\alpha^2 f^2$ from Eq. (2.25), the field then evolves according to the equation of motion stated above, now including mass. The general form of the solution is a sinusoidal oscillation with a decaying power law in time. For example, the solution to the field evolution in a radiation dominated universe is a Bessel function

$$\phi(t) \propto t^{-1/4} J_{1/4}(mt) \approx Ct^{-3/4}\sin(mt) = Ca(t)^{-3/2}\sin(mt). \tag{2.26}$$

Regardless of the time dependence of H, the result is that the amplitude of the field oscillations is proportional to the scale factor in this regime

$$A_\phi \propto a^{-3/2}. \tag{2.27}$$

The energy density of the oscillating field as a function of time is

$$\rho = \frac{1}{2}m^2 A_\phi(t)^2 = \frac{1}{2}m^2 A_\phi(t_1)^2 \frac{a(t_1)^3}{a(t)^3}, \tag{2.28}$$

where t_1 is the time at which the oscillations began, at the temperature scale $\Lambda_1 = m$. Finally this allows us to find the energy density today. The initial amplitude of the PNGB oscillations is

$$A_\phi(t_1) = \alpha f. \tag{2.29}$$

The ratio of scale factors can be expressed as a ratio of temperatures

$$\frac{a(t_1)}{a(t_0)} = \frac{T_0}{T_1}, \tag{2.30}$$

where the subscript 0 denotes values at the present day, yielding

$$\rho_0 = \frac{1}{2} m^2 \alpha^2 f^2 \frac{T_0^3}{T_1^3}. \tag{2.31}$$

Using the energy at initial oscillation $T_1 = m$ and the definition of the mass from the previous section, this is simply

$$\rho_0 = \frac{1}{2} \alpha^2 \frac{f^3 T_0^3}{\Lambda^2} \sim \frac{f^3 T_0^3}{\Lambda^2}. \tag{2.32}$$

So the present PNGB energy density depends on the three relevant temperatures: the temperatures at spontaneous symmetry breaking, at explicit symmetry breaking, and the current CMB temperature of 2.7 K.

2.5 Timeline of the PNGB

To summarize the results from the previous sections, we can examine the evolution of the field value in Figure 2.4 and energy density in Figure 2.5.

- First the PNGB starts as a Nambu-Goldstone boson when its parent complex scalar field undergoes spontaneous symmetry breaking at the scale f. It acquires a vaccum expectation value of αf.

- It retains its vacuum expectation value until it reaches the explicit-symmetry-breaking scale Λ and acquires a mass $m = \frac{\Lambda^2}{f}$.

- Now the PNGB is massive, but its mass is much too small to induce any significant changes. The field "slowly rolls" toward its minimum potential energy during this time period since it has a mass, but the change is very small and the majority of its energy density is potential energy, so it acts as vacuum energy with equation of state $w \approx -1$.

- Finally it reaches the third temperature scale T_1, which is set when the mass is the same size as the Hubble parameter $m \sim H$. At this point it begins oscillating. The energy

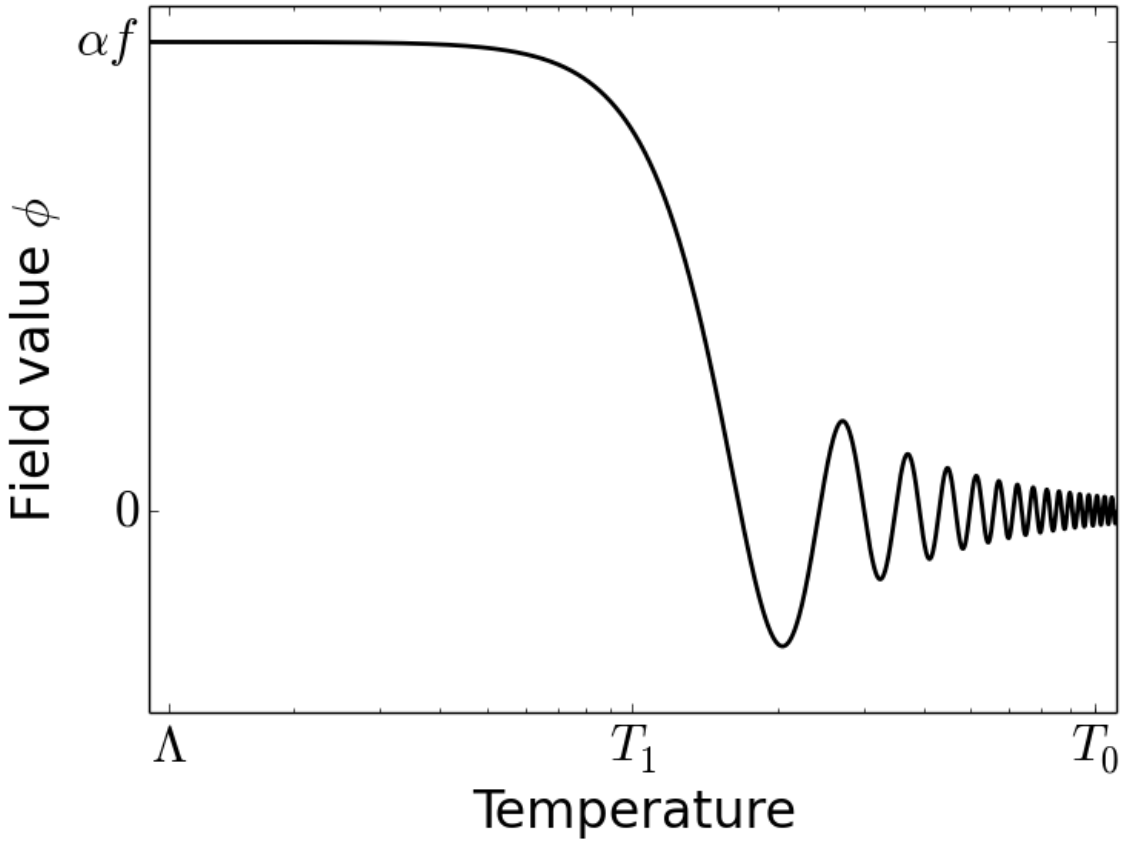

Figure 2.4: PNGB field value vs. temperature. Temperature is plotted on a log scale.

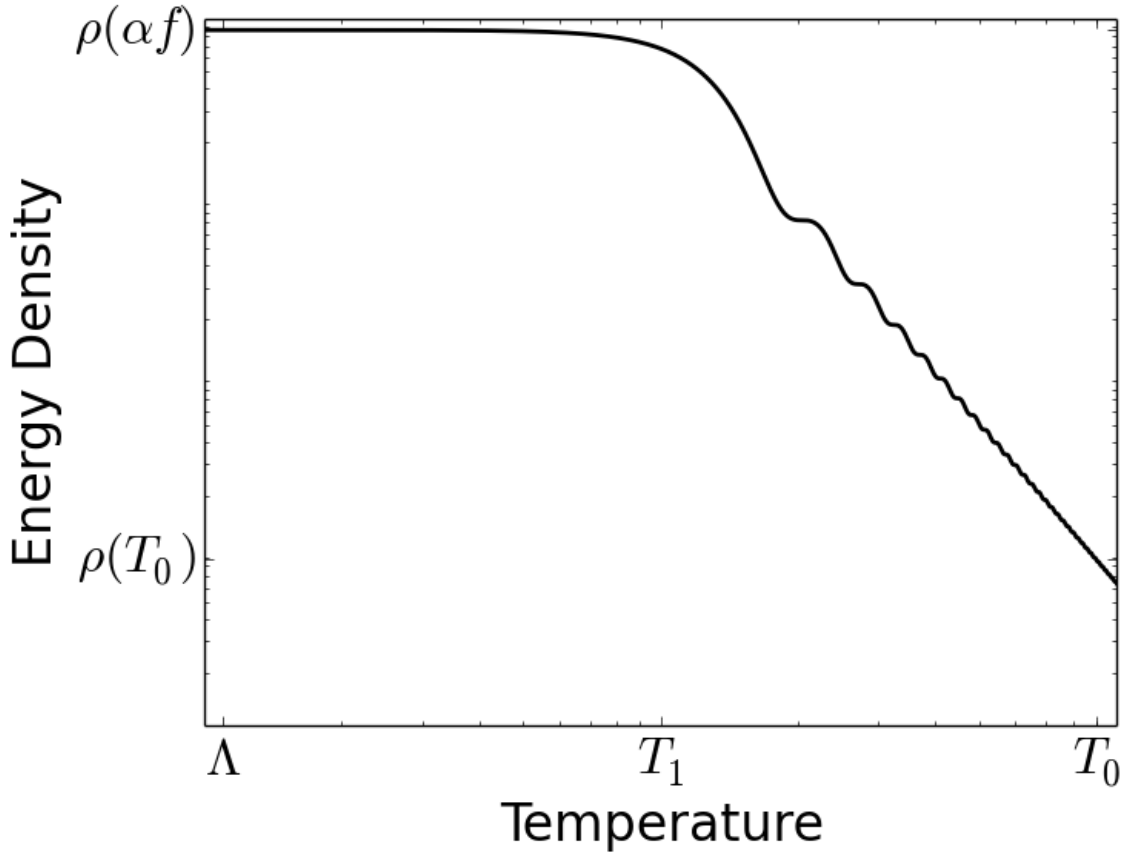

Figure 2.5: Energy density of the PNGB vs. temperature, plotted on a log-log scale.

density begins at $\sim m^2 f^2 = \Lambda^4$ and evolves with time proportional to a^{-3} until reaching the present temperature T_0. Its equation of state is $w \approx 0$, therefore contributing to the matter energy density.

2.6 The Axion

The discussion until this point has only referred to a generic PNGB. The above results should roughly hold for a wide range of PNGBs regardless of the physics that generates them, as well as the two specific examples: the axion and quintessence. While they are both PNGBs, they are at different points in their evolution and we will arrive at a few interesting values like the axion-mass lower bound and the quintessence mass.

The axion was originally postulated to solve the strong CP problem.[12] It makes its transition from Nambu-Goldstone boson to PNGB at the QCD scale so the explicit-symmetry-breaking scale for the axion can be identified as

$$\Lambda = \Lambda_{QCD} \approx 200 \text{ GeV}. \tag{2.33}$$

Now the axion's density parameter can be calculated

$$\Omega_{axion} = \frac{\rho_0}{\rho_c}, \tag{2.34}$$

where ρ_c is the critical density. Finally the requirement that it be less than the dark matter density parameter $\Omega_{axion} < 0.2$, results in an upper limit on f on the order of 10^{12} GeV.[6]

Assuming the axion is the dark matter particle, an approximate bound can be placed on the axion mass using the formula

$$m > \frac{\Lambda^2}{f_{max}} = \frac{(200 \text{ GeV})^2}{10^{21} \text{ eV}} = 4\mu\text{eV}, \tag{2.35}$$

which sets a lower limit on the axion mass.

2.7 Quintessence

The quintessence field is one possible candidate for dark energy. The dark-energy density is the same order of magnitude as the critical density of the universe at present day, and if the dark energy is of the form of a cosmological constant then its value is unnaturally small at early times. To resolve this "naturalness problem," consider the existence of a PNGB whose explicit-symmetry-breaking scale is very close to the temperature of the universe at present.[7],[13]

In the timeline of a PNGB, quintessence is just now entering the slow-roll phase. It has acquired a mass at a scale of the vacuum energy $\Lambda \sim 10^{-3}$ eV, and almost all of its energy is in the form of potential energy, which results in dark energy having a significant contribution to the density today. Furthermore its symmetry-breaking scale is expected to be at the scale of some new unknown physics. A natural scale to postulate for spontaneous symmetry breaking is the Planck scale: $f \sim M_P = 10^{28}$ eV. With these two scales, a naive estimate of the expected mass of the quintessence particle can be obtained[14]

$$m = \frac{\Lambda^2}{f} = 10^{-34} \text{ eV}. \tag{2.36}$$

2.8 Birefringence

Finally, we consider how this relates to birefringence. The Chern-Simons term is of the form

$$\mathcal{L}_{CS} = -\frac{\beta\phi}{2M} F^{\mu\nu}\tilde{F}_{\mu\nu}. \tag{2.37}$$

Where β is a dimensionless coupling, ϕ is the PNGB field, and M is a coupling of mass dimension 1. To see how this could cause a rotation of a linearly polarized photon, consider

the modified electromagnetic Lagrangian

$$\mathcal{L} = -\frac{1}{4}F^{\mu\nu}F_{\mu\nu} - \frac{\beta\phi}{2M}F^{\mu\nu}\tilde{F}_{\mu\nu}. \tag{2.38}$$

The Euler-Lagrange equations for the field A_μ are

$$\partial^\nu F_{\mu\nu} + \partial_\nu\left(\frac{\beta\phi}{M}\varepsilon^{\nu\mu\rho\sigma}F_{\rho\sigma}\right) = 0. \tag{2.39}$$

Since the quantity $\varepsilon^{\nu\mu\rho\sigma}\partial_\nu F_{\rho\sigma}$ is identically zero, this equation becomes

$$\partial^\nu F_{\mu\nu} + \frac{\beta}{M}\varepsilon^{\mu\rho\sigma\nu}F_{\rho\sigma}\partial_\nu\phi = 0. \tag{2.40}$$

Identifying the components of the field strength tensor with the electric and magnetic fields as

$$E^i = -F^{0i}, \tag{2.41}$$

$$B^i = -\varepsilon^{ijk}F_{jk}, \tag{2.42}$$

the two equations take the forms

$$\vec{\nabla}\cdot\vec{E} - \frac{\beta}{M}\vec{B}\cdot\vec{\nabla}\phi = 0, \tag{2.43}$$

$$\vec{\nabla}\times\vec{B} - \frac{\partial\vec{E}}{\partial t} + \frac{\beta}{M}\left(\vec{E}\times\vec{\nabla}\phi - \vec{B}\frac{\partial\phi}{\partial t}\right) = 0. \tag{2.44}$$

For a spatially uniform scalar field, ϕ only appears in Eq. (2.44), which is now of the form:

$$\vec{\nabla}\times\vec{B} - \frac{\partial\vec{E}}{\partial t} = \frac{\beta}{M}\vec{B}\frac{\partial\phi}{\partial t}. \tag{2.45}$$

Therefore if the scalar PNGB field changes over time as a linearly polarized photon travels through the universe, the electric-field vector will change in the direction of the magnetic field. This corresponds to a rotation of the electric field direction. The total rotation angle α can be written in terms of the total change in the PNGB field value[14]

$$\alpha = \frac{\beta}{M}\Delta\phi. \tag{2.46}$$

Following in the theme of this discussion the magnitude of M should be considered. Since this term deals with ϕ, it should be at least as big as the spontaneous-symmetry-breaking scale f. But recall that the PNGB descended from a theory of a complex scalar field ψ, so this coupling likely has a scale associated with some higher energy physics. Again, a plausible scale for this would be the Planck scale $M \sim M_P$.

In order to detect any appreciable rotation angle, the change in the field value of the PNGB must not be more than a few orders of magnitude smaller than M_P. The axion's spontaneous-symmetry-breaking scale has an upper bound at around 10^{21} eV, so any rotation of photon polarization due to the axion field would be at largest on the order of 10^{-7} rad.

On the other hand, quintessence undergoes spontaneous symmetry breaking closer to the Planck scale. If quintessence exists, we would expect to naturally observe rotation angles on the order of the ratio $\frac{f}{M}$, which could conceivably be as large as order unity.

Put in this context, the axion and quintessence fields should both cause cosmological birefringence, but the magnitudes of these effects may be very different, roughly corresponding to the ratio of their spontaneous-symmetry-breaking scales.

2.9 The Standard-Model Extension

Until now, the focus has been on one possible mechanism for generating cosmic birefringence, but the SME is a framework to characterize all realistic violations of Lorentz symmetry based on effective field theory, while maintaining other desireable features such as

gauge invariance, renormalizability, etc.[15],[16],[17] .

Within this framework, we can classify potential Lorentz violations in the photon sector with two sets of differential operators $\hat{\boldsymbol{k}}_{AF}$ and $\hat{\boldsymbol{k}}_F$, which characterize CPT-odd and CPT-even violations, respectively.[18],[19] They appear in the extended electromagnetic Lagrangian[20]

$$\mathcal{L}_{SME} = -\frac{1}{4}F_{\mu\nu}F^{\mu\nu} + \frac{1}{2}\epsilon^{\kappa\lambda\mu\nu}A_\lambda \left(\hat{\boldsymbol{k}}_{AF}\right)_\kappa F_{\mu\nu} - \frac{1}{4}F_{\kappa\lambda}\left(\hat{\boldsymbol{k}}_F\right)^{\kappa\lambda\mu\nu} F_{\mu\nu}, \tag{2.47}$$

where A_μ is the vector potential, $F_{\mu\nu}$ is the field strength tensor, and the SME operators are defined as

$$\left(\hat{\boldsymbol{k}}_{AF}\right)_\kappa = \sum_{d=\text{odd}} \left(k_{AF}^{(d)}\right)_\kappa^{\alpha_1\ldots\alpha_{(d-3)}} \partial_{\alpha_1}\ldots\partial_{\alpha_{(d-3)}}, \tag{2.48}$$

$$\left(\hat{\boldsymbol{k}}_F\right)^{\kappa\lambda\mu\nu} = \sum_{d=\text{even}} \left(k_F^{(d)}\right)^{\kappa\lambda\mu\nu\alpha_1\ldots\alpha_{(d-4)}} \partial_{\alpha_1}\ldots\partial_{\alpha_{(d-4)}}. \tag{2.49}$$

The effect of including the higher-dimension d terms introduces an energy dependence. Expressing the operators in a spherical-harmonic basis, we can write these possible Lorentz violations as first-order modifications to the photon dispersion relation

$$\omega = \left[1 - \varsigma^0 \pm \sqrt{\left(\varsigma^1\right)^2 + \left(\varsigma^2\right)^2 + \left(\varsigma^3\right)^2}\right] k, \tag{2.50}$$

where the "$\pm$" corresponds to the two polarizations and the four ς^i are given as sums over SME parameters[5]

$$\varsigma^0 = \sum_{djm} \omega^{d-4}\ {}_0Y_{jm}(\hat{\boldsymbol{n}}) k_{(I)jm}^{(d)}, \tag{2.51}$$

$$\varsigma^1 \pm i\varsigma^2 = \sum_{djm} \omega^{d-4}\ {}_{\pm2}Y_{jm}(\hat{\boldsymbol{n}}) \left(k_{(E)jm}^{(d)} \mp i k_{(B)jm}^{(d)}\right), \tag{2.52}$$

$$\varsigma^3 = \sum_{djm} \omega^{d-4}\ {}_0Y_{jm}(\hat{\boldsymbol{n}}) k_{(V)jm}^{(d)}, \tag{2.53}$$

where $j \leq d-2$ and $\hat{\boldsymbol{n}} = -\hat{\boldsymbol{p}}$ is the line-of-sight direction toward the photon's point of origin. The terms in Eqs. (2.51) and (2.52) exist only for even values $d \geq 4$ while those in Eq. (2.53) exist for odd values $d \geq 3$. It is in terms of the four sets of parameters $k^{(d)}_{(I)jm}, k^{(d)}_{(E)jm}, k^{(d)}_{(B)jm}, k^{(d)}_{(V)jm}$ that we can classify Lorentz violations.[5]

2.10 Using the CMB for Birefringence Tests

Now in order to determine which of these infinitely many parameters we can constrain using CMB measurements, we should understand to what each of these four ς^i terms correspond. From the dispersion relation we can see that ς^0 is the only one that changes the photon speed by the same amount for both polarizations. This term will not generate birefringence, but, because it contains energy dependence from parameters of dimension $d > 4$, its effects can be detected, for example, by measuring arrival times of photons with different frequencies from the same source. However, CMB experiments are not ideal for searching for such an effect, since they may operate only over a single frequency band or a few relatively closely spaced bands. Still, we leave such estimates to a future paper.

The terms ς^1 and ς^2 characterize CPT-even birefringent effects which mix linear polarization and circular polarization. However the polarization of the CMB, generated primarily by Thomson scattering, is not expected to contain circular polarization and as such CMB experiments typically are not designed to search for circular polarization.

Finally, ς^3 characterizes CPT-odd birefringent effects, which result in a rotation of linearly polarized photons without conversion to circular polarization. Measurements of CMB polarization are particularly sensitive to this effect. Unlike other polarized astrophysical sources, like gamma-ray bursts (GRBs) or quasars, the CMB is a well-understood source governed by simple linear physics that allows us to predict the initial polarization state of emitted photons to high accuracy. Combined with the fact that the CMB surface of last scattering has redshift $z \sim 1100$, the extraordinarily long propagation distance of CMB

photons allows any birefringent effects to accumulate. This is why the CMB is the most sensitive probe of Lorentz violations of this type.[5]

Each of these potential Lorentz-violating terms carries energy dependence that increases with the dimension d of the SME parameters. While the CMB is a relatively low-energy source, higher-energy sources like GRBs, pulsars, and blazars will give us much tighter constraints on these higher-dimension parameters. However, for the lowest-dimension terms, CMB measurements are not hampered by this energy dependence, and it is for this reason that we restrict our analysis only to the dimension ($d = 3$) coefficients of the SME.

In this case, the change in polarization angle of a linearly polarized photon is[5]

$$\delta\psi_z = \int_0^z \frac{dz}{(1+z)H_z} \sum_{jm} Y_{jm}(\hat{\boldsymbol{n}}) k^{(3)}_{(V)jm}, \tag{2.54}$$

where the sum is over $j = 0, 1$. For a CMB photon, this is approximately

$$\delta\psi_{\text{CMB}} \approx \left(\frac{3.8^\circ}{10^{-43}\ \text{GeV}}\right) \sum_{jm} Y_{jm}(\hat{\boldsymbol{n}}) k^{(3)}_{(V)jm}. \tag{2.55}$$

2.11 POLARBEAR Observations

We can use observations from the POLARBEAR experiment[21] to constrain these dimension $d = 3$ SME parameters using its three observational patches. These patches are approximately $3^\circ \times 3^\circ$, which is relatively small in the context of the dimension 3 parameters we wish to constrain. Eq. (2.55) contains simple spherical harmonics up to $j = 1$, meaning we are dealing with a monopole term and dipole terms. If we take measurements of a constant rotation angle across one of these sky patches as a measurement of $\delta\psi$ at that particular right ascension and declination, then we can constrain direction-dependent combinations of the four $d = 3$ coefficients.

We can see the three patches in Figure 2.6, along with the values of their RA and

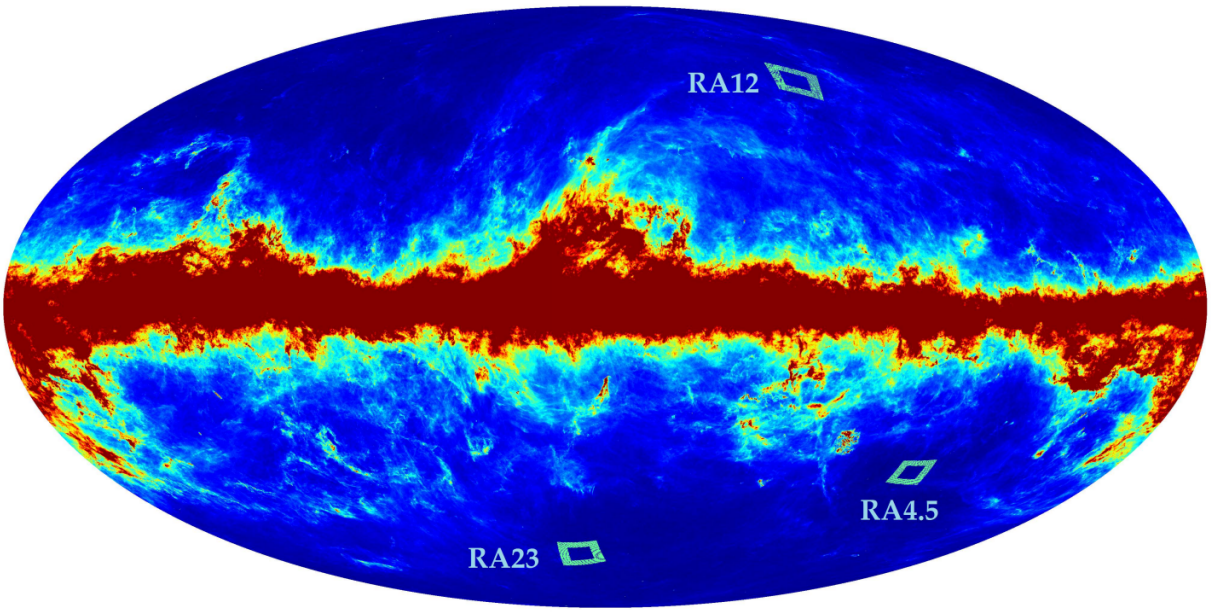

Patch	RA	Dec	Effective Area
RA4.5	$04^{\mathrm{h}}40^{\mathrm{m}}12^{\mathrm{s}}$	$-45°$	7.0 deg^2
RA12	$11^{\mathrm{h}}53^{\mathrm{m}}00^{\mathrm{s}}$	$-0°20'$	8.7 deg^2
RA23	$23^{\mathrm{h}}01^{\mathrm{m}}48^{\mathrm{s}}$	$-32°48'$	8.8 deg^2

Figure 2.6: The three POLARBEAR Patches overlaid on a Planck Collaboration full-sky 857 GHz intensity map. [21]

Dec. The constraint equations would then be

$$\delta\psi_{\mathrm{ra4.5}} = 3.8^\circ \sum_{jm} Y_{jm}(-45^\circ, 70^\circ) \left(\frac{k^{(3)}_{(V)jm}}{10^{-43}\ \mathrm{GeV}} \right), \tag{2.56}$$

$$\delta\psi_{\mathrm{ra12}} = 3.8^\circ \sum_{jm} Y_{jm}(-0.5^\circ, 178^\circ) \left(\frac{k^{(3)}_{(V)jm}}{10^{-43}\ \mathrm{GeV}} \right), \tag{2.57}$$

$$\delta\psi_{\mathrm{ra23}} = 3.8^\circ \sum_{jm} Y_{jm}(-33^\circ, 345^\circ) \left(\frac{k^{(3)}_{(V)jm}}{10^{-43}\ \mathrm{GeV}} \right). \tag{2.58}$$

There is one additional complication. During the first season of observations, the POLARBEAR experiment's absolute angle calibration was obtained by minimizing the EB power spectrum under the assumption of zero overall birefringence.[22] Such an instrumental offset α' will mix the parity-even E-mode polarization patterns with the parity-odd B-mode polarization patterns to generate spurious TB and EB correlations that are proportional to α'. E- and B-mode maps are rotated by an overall rotation angle to minimize the EB power spectrum in order to remove instrumental miscalibration. This instrumental offset is unfortunately degenerate with a global birefringence angle α meaning that the POLARBEAR patches cannot constrain the monopole term $k^{(3)}_{(V)00}$ but can still constrain the other coefficients even after this self-calibration procedure by performing the same EB minimization procedure on each of the three patches individually and using the monopole-subtracted rotation angles to constrain the $j = 1$ SME coefficients. We leave the calculation of these $j = 1$ SME coefficients using data from the POLARBEAR experiment to a future work.

2.12 Conclusion and Outlook

We have seen now both a theoretical motivation to search for cosmic birefringence and a framework set up by the Standard-Model Extension to use experimental results to place limits on Lorentz-violating effects. Using measurements of the CMB's polarization rotation we can place extremely sensitive constraints on a set of low-dimension SME parameters on

the order of 10^{-43} GeV.

However, there is still room for improvement. Experiments like POLARBEAR are in direct need of more accurate calibration measurements. An absolute polarization-angle calibration source would allow POLARBEAR and other similar CMB experiments to forego self-calibration methods and allow measurements of a global rotation angle offset to constraint isotropic cosmic birefringence as well.[23]

The CMB's potential as a probe of parity and Lorentz violation is promising. Through more accurate polarization calibration, or multifrequency analysis, or even a probe of spurious circular polarization we may yet extract even more information from the oldest light in the universe in our search for Lorentz violations in the laws of physics.

Acknowledgements

The authors would like to thank Grant Teply for useful discussions and feedback on this paper, and Kevin Crowley for help with the preparation of this paper.

Chapter 2, in full, is a reprint of material as it appears in D. Leon, J. Kaufman, B. Keating, and M. Mewes, "The cosmic microwave background and pseudo-Nambu-Goldstone bosons: Searching for Lorentz violations in the cosmos," Mod. Phys. Lett. A, 32, 1730002, 2017 (arXiv:1611.00418) [1]. The dissertation author was the primary author of this work.

Chapter 3

Constraints on Lorentz Invariance and CPT Violation using Optical Photometry and Polarimetry of Active Galaxies BL Lacertae and S5 B0716+714

Various quantum gravity approaches that extend beyond the standard model predict Lorentz Invariance and Charge-Parity-Time Violation at energies approaching the Planck scale. These models frequently predict a wavelength dependent speed of light, which would result in time delays between promptly emitted photons at different energies, as well as a wavelength-dependent rotation of the plane of linear polarization for photons resulting from vacuum birefringence. Here, we describe a pilot program with an automated system of small telescopes that can simultaneously conduct high cadence optical photometry and polarimetry of Active Galactic Nuclei (AGN) in multiple passbands. We use these observations as a proof-of-principle to demonstrate how such data can be used to test various Lorentz Violation

models, including special cases of the Standard Model Extension (SME). In our initial campaign with this system, the Array Photo Polarimeter, we observed two AGN sources, including BL Lacertae at redshift $z = 0.069$, and S5 B0716+714 at $z = 0.31$. We demonstrate that optical polarimetry with a broadband *Luminance* filter combined with simultaneous I_c-band observations yields SME parameter constraints that are up to ∼10 and ∼30 times more sensitive than with a standard I_c-band filter, for SME models with mass dimension $d = 5$ and $d = 6$, respectively. Using only a small system of telescopes with an effective 0.45-m aperture, we further demonstrate $d = 5$ constraints for individual lines of sight that are within a factor of ∼1-10 in sensitivity to comparable constraints from optical polarimetry with a 3.6-m telescope. Such an approach could significantly improve existing SME constraints via a polarimetric all-sky survey of AGN with multiple 1-meter class telescopes.

3.1 Introduction

Special relativity and the standard model of particle physics obey the symmetry of Lorentz Invariance, which has survived an enormous range of tests over the past century (See [24] for a review). However, many theoretical approaches seeking to unify quantum theory and general relativity predict that Lorentz Invariance may be broken at energies approaching the Planck scale $E_p = \sqrt{c^5\hbar/G} = 1.22{\times}10^{19}\,\mathrm{GeV}$, perhaps due to the underlying quantized nature of spacetime (e.g. [25, 26]). Since the relevant energies are not accessible to any current, or foreseeable, Earth-bound tests, most approaches to testing such models have relied on observations of high redshift astronomical sources to exploit small effects that may accumulate to detectable levels over cosmological distances and timescales.

This paper considers only Lorentz Invariance Violation (LIV) for photons[1], which can lead to a modified vacuum dispersion relation, and therefore an energy dependent speed of light, which causes a time delay (or early arrival) for promptly emitted photons of different

[1]Other authors have considered testing LIV models for massive particles including neutrinos, which can be considered as approximately massless [27, 28, 29, 30, 26] and cosmic rays [31, 32, 33, 34, 35].

Table 3.1: Celestial coordinates and BVR magnitudes of observed AGN sources from the Simbad database. Lum and I_c magnitudes are mean values from our own photometry in Tables 3.5-3.6.

Name	RA IRCS(J2000)°	DEC IRCS(J2000)°	Redshift z	z Ref.	B (mag)	V (mag)	R (mag)	Lum (mag)	I_c (mag)
S5 0716+714	110.47270192	+71.34343428	0.31 ± 0.08	[41, 42]	15.50	14.17	14.27	14.65	14.10
BL Lacertae	330.68038079	+42.27777231	0.0686 ± 0.0004	[43]	15.66	14.72	13.00	13.89	13.06

energies [28, 36, 37]. LIV models can also yield vacuum birefringence, which causes a rotation of the plane of linear polarization for promptly emitted photons at different energies emitted with the same initial polarization angle [38, 36]. In general, each of these effects can be anisotropic, such that time delays and polarization rotations possess an angular dependence on the sky, and require observations of extended sources like the Cosmic Microwave Background (CMB) or measurements of point sources along many lines of sight to fully test the LIV model parameter space [39, 40].

Testing LIV is difficult because each of these effects are expected to be negligible at energies accessible in Earth-bound or solar system experiments. However, any such effects could, in principle, accrue to measurable levels as these tiny deviations from Lorentz symmetry accumulate over cosmological distances. Qualitatively, evidence for LIV time delays from photometric observations are easier to measure for sources at higher cosmological redshifts and higher energies [27, 28, 36, 39]. Compared to time delays, birefringent LIV models can be tested with much higher sensitivity using spectropolarimetry or broadband polarimetry [39].

In this work, we restrict our analysis to constraining a subset of the Standard Model Extension (SME), an effective field theory approach describing the low energy corrections stemming from a more fundamental Planck scale theory of quantum gravity. The SME therefore provides a general framework for Lorentz Invariance and Charge-Parity-Time (CPT) violation tests with electromagnetic radiation [39].[2] More specifically, since we are only reporting observations of two optical AGN sources, we are limited to constraining either

[2]We therefore do not consider models such as Doubly (or Deformed) Special Relativity (e.g. [44, 45]), which may not be compatible with the SME [39, 40].

general SME models along specific lines of sight or vacuum isotropic SME models, which correspond to some of the more popular models studied in the literature. We further confine our analysis to SME models of mass operator dimension $d = 4, 5, 6, 7, 8, 9$. Mass dimension $d = 3$ models are best constrained with observations of the CMB [36, 39, 46, 47, 48, 49, 1][3]. While $d = 4$ models can yield birefringent effects, they would not produce LIV induced time delays, since they involve no changes to the usual photon dispersion relation [39].

Simultaneous photometric observations in two filters allows one to estimate upper limits to time delays between light curves in each bandpass. While our optical time delay constraints are not competitive with observations of gamma-ray bursts [52, 53, 54, 55, 56, 57, 58, 59, 32, 60, 61, 62, 63, 64, 65, 66, 67, 68] or TeV flares from blazars [69, 70, 71, 36, 72, 73, 74], our approach, which may be unique in the literature, does constrain both time delays and maximum observed polarization with simultaneously obtained photometry and polarimetry using the same pair of broadband optical filters. As such, they have the promise to compliment existing SME constraints.

Time delay measurements uniquely constrain the SME vacuum dispersion coefficients and, in principle, could constrain the vacuum birefringent coefficents as well for all models with $d \neq 4$. However, time delay measurements are typically less sensitive than broadband polarimetry for constraining the birefringent SME coefficients [39], so we exclusively use broadband polarimetry to constrain all other SME coefficients. While optical spectropolarimetry can yield constraints $\sim$2-3 orders of magnitude better for $d = 5$ models than broadband optical polarimetry [40], this generally requires $\gtrsim$ 2-meter class telescopes. With telescopes less than 1-m in diameter, broadband polarimetry in two or more filters is considerably more practical, offering a solution that is low-cost and scalable to large numbers of observatories around the world. Since we did not obtain spectropolarimetry in our pilot program, we focus on the broadband polarimetry method for the rest of this work.

When observing a single source, as noted by [54], it is, in general, impossible to

[3]For a discussion of the difficulties in calibrating the reference angle for astrophysical CMB polarization measurements, see [50] and [51].

disentangle an intrinsic time-lag at the source from a delay induced by genuine LIV dispersion effects.[4] Therefore, to constrain LIV models using observed time delays, one must either assume A) there are no intrinsic time delays, or B) statistically model observations of many sources using the fact that all LIV effects are predicted to increase with redshift and therefore be negligible for sufficiently "nearby" sources. For approach B, one would model the population distribution of intrinsic time lags using a calibration sample of low redshift sources and use this to disentangle these non-LIV effects from genuine LIV effects which could be manifest in a suitably matched population of higher redshift sources [54, 39, 40]. However, since we only observed one nearby source (BL Lacertae at $z = 0.0686 \pm 0.0004$; [43]) and one high redshift source (S5 B0716+714 at $z = 0.31 \pm 0.08$, [41, 42]), we assume option A for the remainder of this work.

Similarly, it is, in general, impossible to know the intrinsic polarization angles for photons emitted with different energies from a given cosmological source. If one possessed this information, evidence for birefringence could be obtained by observing differences between the known intrinsic polarization angle and the actual observed angles for photons emitted promptly with the same polarization angle but at different energies. However, even in the absence of such knowledge, birefringent effects can be constrained for sources at arbitrary redshifts because a large degree of birefringence would yield large differences in observed polarization angles at nearby frequencies, effectively washing out most, if not all, of the observed polarization [39, 62, 67]. Therefore, observing a given polarization fraction can constrain wavelength-dependent birefringence effects, which, if in effect, would have led to a smaller degree of observed polarization. To analyze SME models in this work, we follow the "average polarization" approach in [40].[5]

In this work, we present simultaneous photometric and polarimetric observations

[4]Note that the cosmological time delay calculation from [54] contains a basic error which was noted and corrected by [28] and used by subsequent analyses (e.g. [36, 40]). This issue is also relevant for LIV tests using gravitational lensing [75] and pulsar timing [76].

[5]The authors in [40] also analyzed both optical polarimetry and spectropolarimetry, where available, from 72 existing polarized AGN and Gamma-Ray Burst (GRB) afterglow sources in the literature (e.g. [77, 78, 79]).

using two broadband optical filters on separate telescopes, including the *Luminance*-band filter (Lum) and a Johnson-Cousins I-band filter (I_c). While not as common as standard optical $BVRI$ filters, we chose the wider Lum filter both to maximize the signal for our small telescopes and because wider optical bandpasses lead to tighter constraints on birefringent SME Models obtained using any of the standard optical $BVRI$ filters [40]. In particular, we demonstrate significant advantages of the wider Lum filter versus the narrower I_c filter, where, for the same observed maximum polarization fraction, the Lum filter yields $d = 5, 6$ SME parameter upper bounds that are factors of ∼3-26 times more sensitive than with the I_c-band filter.

In addition, we develop a technique to combine simultaneous polarimetric observations using two co-located telescopes with different filters into an effective system with a single broadband optical filter that avoids the expense of a half-wave plate with high transmission over the full ∼400-900 nm wavelength range of the combined $Lum + I_c$ filter. This yields more stringent SME constraints than either filter alone, while achieving the effective light collecting power of a larger telescope. This approach can be contrasted with an optical system using dichroic beamsplitters on a single telescope to obtain simultaneous polarimetry in different bandpasses (e.g. the DIPOL-2 instrument [80]). With this approach, for the same observed maximum polarization fraction, our combined $Lum + I_c$ filter yields $d = 5, 6$ SME parameter upper bounds that are factors of ∼2-30 times more sensitive than with the I_c-band filter.

The pilot program in this work is meant as a proof-of-principle to obtain the most stringent SME constraints using broadband optical polarimetric observations with small telescopes for which spectropolarimetry is unfeasible. Even without spectropolarimetry, anisotropic SME constraints can be improved by observing sources along lines of sight without previously published optical polarimetry. Even if specific AGN sources already have published optical polarimetry, improved SME constraints can potentially be obtained simply by observing these sources with wider optical bandpasses, and by potentially observing a larger maximum polarization value than previously found. For all of these reasons, this work

aims to motivate design feasibility studies for a follow up optical polarimetry survey using at least two 1-m class telescopes, with one or more in each hemisphere.

This paper is organized as follows. In §3.2, we describe the Standard Model Extension family of Lorentz and CPT-Invariance violating models we are interested in testing and present our main constraints. In §3.3, we describe the optical polarimetric and photometric observing systems used in this work, with emphasis on correcting for systematic errors in our maximum polarization measurements. Conclusions are presented in 3.4. Mathematical details, and the data obtained for this paper are presented in the Appendix.

3.2 Standard Model Extension

We do not describe the full SME framework here. Instead, see [39] for a review. Qualitatively, if the Standard Model holds perfectly, all SME coefficients vanish identically. No strong evidence yet exists for any non-zero SME coefficients, and therefore, many LIV models falling under the SME umbrella have already been ruled out. However, the general approach to make progress testing such models is to use observations of cosmological sources at different wavelengths, higher redshifts, and varied positions on the sky to progressively lower the upper bounds for any non-zero values of the coefficients over the full SME parameter space. Weak constraints imply very large, uninformative, upper bounds. Strong constraints imply very small, informative, upper bounds that constrain coefficient values progressively closer to zero. However, even seemingly weak constraints can be of value of they are obtained with an observational approach with smaller (or different) systematics than an approach that nominally yields stronger constraints [40].

3.2.1 Vacuum Dispersion SME Models

Most LIV models predict a wavelength-dependent speed of light, leading to light of a given energy arriving earlier (or later) than light of another energy, even if both were emitted

simultaneously in the rest frame of the source. Following [28, 36, 39, 62], using "natural" units (in which $\hbar = c = 1$), in the context of the SME, the arrival time difference between photons emitted simultaneously from a cosmological source with index label s at redshift $z = z_s$ and sky position (θ_s, ϕ_s), with observed energies E_1 and E_2, (and detected at observer frame times t_1 and t_2, respectively), is given by

$$\Delta t^{(d)}_{(z_s)} \;=\; t_2 - t_1 \approx \left(E_2^{d-4} - E_1^{d-4}\right) L^{(d)}_{(z_s)} \sum_{jm} Y_{jm,s} c^{(d)}_{(I)jm} \,, \tag{3.1}$$

where $Y_{jm,s} \equiv Y_{jm}(\theta_s, \phi_s)$ are the spin weighted spherical harmonics for spin-0[6], $c^{(d)}_{(I)jm}$ are the vacuum dispersion SME coefficients with mass dimension $d = 4, 6, 8, \ldots$ which must be CPT-even, and

$$L^{(d)}_{(z_s)} = \int_0^{z_s} \frac{(1+z)^{d-4}}{H(z)} dz = \int_{a_s}^{1} \frac{da}{(a)^{d-2} H(a)} \,, \tag{3.2}$$

where $L^{(d)}_{(z_s)}$ is the effective comoving distance traveled by the photons, including the cosmological effects needed to compute arrival time differences in an expanding universe [28]. Setting $d = 4$ recovers the usual expression for comoving distance. In Eq. (3.2), $H(z) = H(a)$ is the Hubble expansion rate at a redshift z_s with scale factor $a_s^{-1} = 1 + z_s$ (with the usual normalization $a(t_0) = 1$ at the present cosmic time $t = t_0$ at $z = 0$) given by

$$H(a) = H_0 \Big[\Omega_{\rm r} a^{-4} + \Omega_{\rm m} a^{-3} + \Omega_{\rm k} a^{-2} + \Omega_\Lambda \Big]^{1/2} , \tag{3.3}$$

in terms of the present day Hubble constant, which we set to $H_0 = 73.24$ km s^{-1}Mpc^{-1} [81], and best fit cosmological parameters for matter $\Omega_{\rm m} = 0.3089$, radiation $\Omega_{\rm r} = \Omega_{\rm m}/(1 + z_{eq}) = 9.16{\times}10^{-5}$ (with the matter-radiation equality redshift $z_{eq} = 3371$), vacuum energy $\Omega_\Lambda = 0.6911$, and curvature $\Omega_{\rm k} = 1 - \Omega_{\rm r} - \Omega_{\rm m} - \Omega_\Lambda \approx 0$ using the Planck satellite 2015 data

[6] $Y_{jm} \equiv {}_0Y_{jm}$ are the usual spherical harmonics for spin-0.

release [82].[7]

In principle, observations constraining the theoretical time delay $\Delta t^{(d)}_{(z_s)}$ from Eq. (3.1) between photons observed at different energies can constrain the SME coefficients $c^{(d)}_{(I)jm}$. More specifically, an upper bound $|\Delta t_\star|$ on the theoretical time delay (or early arrival) $|\Delta t^{(d)}_{(z_s)}| \leq |\Delta t_\star|$ measured from photometry in different bandpasses can be recast as an upper bound on a linear combination of SME coefficients:

$$\left|\bar{c}^{(d)}_{(I),s}\right| \lesssim \frac{c\,|\Delta t_\star|}{\left|E_2^{d-4} - E_1^{d-4}\right| L^{(d)}_{(z_s)}}, \tag{3.4}$$

where $\bar{c}^{(d)}_{(I),s} \equiv \sum_{jm} Y_{jm,s} c^{(d)}_{(I)jm}$ is shorthand for the linear combination of vacuum dispersion SME coefficients for source s and E_1 and E_2 can be estimated from the central wavelengths of the filters.

Fig. 3.1 shows the relation between time delay upper limits and $d = 6$ isotropic SME models for sample sources observed with both our *Lum* and I_c filters over a range of redshifts $z \in [0.1, 1, 10]$, while highlighting the parameter space already ruled out by limits from GRB observations, as well as the weaker, but meaningful constraints obtainable from optical time delay data with $|\Delta t_\star| \leq 1$ hour.

3.2.2 CPT-Odd Vacuum Birefringent SME Models

For a subset of vacuum birefringent SME models with coefficients $k^{(d)}_{(V)jm}$, where the mass dimension $d = 3, 5, 7, \ldots$ must be CPT-odd, rather than arrival times, the relevant quantity is the rotation of the plane of linear polarization for photons with different observed energies E_1 and E_2 that were emitted in the rest frame of the source with the same polarization angle. After traveling an effective distance of $L^{(d)}_{(z_s)}$ through an expanding universe, the

[7] We use cosmological parameters reported in Table 4 column 6 of [82]. These are the joint cosmological constraints (TT,TE,EE+lowP+lensing+ext 68% limits (where ext=BAO+JLA+H0)). However, based on recent tension between the Hubble constant H_0 determined using CMB data and Type Ia supernovae (SN Ia), we use the SN Ia Hubble constant $H_0 = 73.24$ km s^{-1}Mpc^{-1}[81] rather than $H_0 = 67.74$ km s^{-1}Mpc^{-1}from Table 4 column 6 of [82].

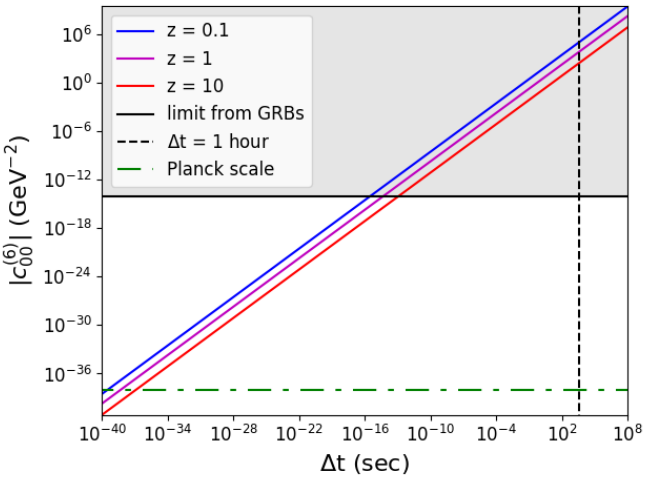

Figure 3.1: We plot the dimension $d = 6$ isotropic vacuum dispersion SME parameter $|c^{(6)}_{(I)00}|$ for time delays between two example observations in the *Lum* and I_c bands (central wavelengths of ∼550 nm vs. ∼800 nm) for various redshift sources ($z = 0.1, 1, 10$).

The horizontal dot-dashed line shows the $|c^{(6)}_{(I)00}|$ corresponding to the Planck energy scale, while the dashed vertical line corresponds to a time delay of 1 hour. Gray regions in the parameter space with $|c^{(6)}_{(I)00}| \gtrsim 10^{-14}$ GeV^{-2} have already been ruled out by high redshift, high time resolution, Gamma-Ray burst data [62]. Because of this, optical time delays on the order of minutes to hours for moderate redshift sources can only provide weak — but still independent — constraints as a consistency check.

difference in their observed polarization angles $\Delta\psi^{(d)}_{(z_s)} = \psi_2 - \psi_1$ will be

$$\Delta\psi^{(d)}_{(z_s)} \;\approx\; \left(E_2^{d-3} - E_1^{d-3}\right) L^{(d)}_{(z_s)} \sum_{jm} Y_{jm,s} k^{(d)}_{(V)jm} \,. \tag{3.5}$$

In principle, polarimetric observations measuring an observed polarization angle difference $|\Delta\psi_\star|$ in a single broadband filter with bandpass edge energies E_1 and E_2, with $|\Delta\psi^{(d)}_{(z_s)}| \leq |\Delta\psi_\star|$, can constrain the SME coefficients $k^{(d)}_{(V)jm}$ directly using Eq. (3.5),

$$\left|\bar{k}^{(d)}_{(V),s}\right| \;\leq\; \frac{c\,|\Delta\psi_\star|}{\left|E_2^{d-3} - E_1^{d-3}\right| L^{(d)}_{(z_s)}} \,, \tag{3.6}$$

where $\bar{k}^{(d)}_{(V),s} \equiv \sum_{jm} Y_{jm,s} k^{(d)}_{(V)jm}$ is shorthand for the linear combination of birefringent SME coefficients for source s.[8]

[8]We present constraints from our data using the *Lum* and I_c-band optical filters in Sec 3.2.5.

Eq. (3.6) requires the assumption that all photons in the observed bandpass were emitted with the same (unknown) intrinsic polarization angle. When not making such an assumption, a more complicated and indirect argument is required. In general, when integrating over an energy range $[E_1, E_2]$, if LIV effects exist, the observed polarization degree will be substantially suppressed for a given observed energy if $\Delta\psi_\star > \pi$, regardless of the intrinsic polarization fraction at the corresponding rest frame energy [62, 40]. Other authors present arguments allowing them to assume $\Delta\psi_\star \leq \pi/2$ to derive bounds on certain SME models [59, 60, 61]. In our case, observing a polarization fraction $p_\star$ can be used to constrain birefringent SME coefficients as follows.

First, one conservatively assumes a 100% intrinsic polarization fraction at the source for all wavelengths. Lower fractions for the source polarization spectrum would lead to tighter SME bounds. In this case, the total intensity I is equal to the polarized intensity I_p, such that

$$I = \int_{E_1}^{E_2} T(E) dE = I_p \,, \tag{3.7}$$

where $T(E)$ is the total throughput transmission function as a function of photon energy $E = hc/\lambda$ (with wavelength λ) for the polarimeter, including the relevant optics, broadband filters, and detectors (see Fig. 3.2). Then, following [40], integrating Eq. (3.5) over the energy range of the effective bandpass $T(E)$ yields normalized linear polarization Stokes parameters $q \equiv Q/I$ and $u \equiv U/I$, given by

$$\begin{aligned} q^{(d)}_{(z_s)} &= \frac{I_p}{I} \int_{E_1}^{E_2} \cos\Big(2\Delta\psi\Big) T(E) dE \\ &= \int_{E_1}^{E_2} \cos\Big(2\left(E^{d-3} - E_1^{d-3}\right) L^{(d)}_{(z_s)} \bar{k}^{(d)}_{(V),s}\Big) T(E) dE \,, \end{aligned} \tag{3.8}$$

and

$$u^{(d)}_{(z_s)} = \frac{I_p}{I}\int_{E_1}^{E_2} \sin\Big(2\Delta\psi\Big)T(E)dE \tag{3.9}$$
$$= \int_{E_1}^{E_2} \sin\Big(2\left(E^{d-3}-E_1^{d-3}\right)L^{(d)}_{(z_s)}\bar{k}^{(d)}_{(V),s}\Big)T(E)dE\,,$$

where the intensity normalized Stokes parameters $q = q^{(d)}_{(z_s)}$ and $u = u^{(d)}_{(z_s)}$ depend on mass dimension d and redshift z_s in the SME framework.

An upper bound on the observed polarization is then

$$p_\star - 2\sigma_\star < p^{(d)}_{max,(z_s)} = \sqrt{\left(q^{(d)}_{(z_s)}\right)^2 + \left(u^{(d)}_{(z_s)}\right)^2}\,, \tag{3.10}$$

such that observing a polarization fraction $p_\star$ implies an upper bound on $\bar{k}^{(d)}_{(V),s}$ by finding the largest value of $\bar{k}^{(d)}_{(V),s}$ that is consistent with the inequality $p^{(d)}_{max,(z_s)} > p_\star - 2\sigma_\star$, where $\sigma_\star$ is the 1-σ uncertainty on the polarization measurement. This corresponds to a 95% confidence interval assuming Gaussian measurement errors for the polarization fraction.

As shown by [40], in this framework, broader filters lead to smaller values for $p^{(d)}_{max,(z_s)}$, so observing larger $p_\star$ values in those filters leads to tighter constraints on $\bar{k}^{(d)}_{(V),s}$ than observing the same polarization $p_\star$ through a narrower filter for the same source. In addition to improving our signal-to-noise, this is a key reason we chose the broader Lum band filter to compare to the more standard I_c band filter, and implemented a method to combine both filters using simultaneous observations on two telescopes. The transmission $T(\lambda)$ for our combined $Lum + I_c$-band polarimetry is shown in Fig. 3.2, which can be used to compute $T(E)$. Our observational setup is described in § 3.3.

In principle, one should also consider the source spectrum and the atmospheric attenuation in computing $T(E)$, but we follow [40] and assume that the optical spectra are flat enough in the relevant wavelength range so that we can ignore these small effects. However, unlike [40], which only consider the transmission function of the broadband filter,

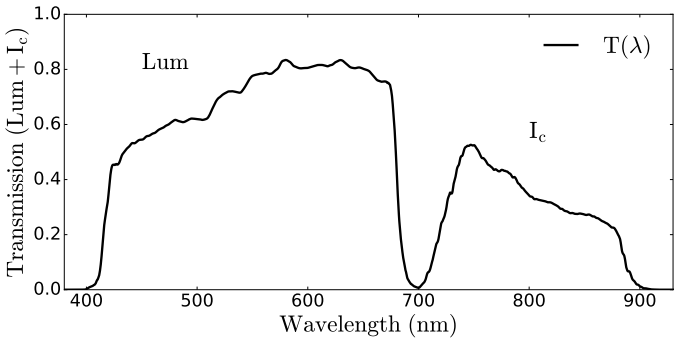

Figure 3.2: Transmission Function

Total transmission function from optics, filters, and CCD detectors for our *Lum* and I_c-bands observed using the Array Photo Polarimeter (APPOL, see §3.3), which we combine into a single, effective broadband $Lum + I_c$ filter with coverage from ∼400-900 nm (with minimal filter overlap at ∼700 nm), using simultaneous data from two telescopes (see Fig. 3.8).

we additionally consider the transmission functions for the optics and CCD detector, in addition to the filter, when computing $T(E)$ (see Fig. 3.8).

Following [40], to jointly parameterize the cosmological redshift dependence and SME parameter effects, we define the quantity $\zeta_s^{(5)}$ as

$$\zeta_s^{(5)} \equiv L_{(z_s)}^{(5)} \bar{k}_{(V),s}^{(5)} \,. \tag{3.11}$$

Also following [40], Fig. 3.3 shows the change in the intensity normalized Stokes parameter $q_{(z_s)}^{(d)}$ from Eq. (3.9) for several values of $\zeta_s^{(5)}$, while Fig. 3.4 shows theoretical limits from the maximum observed polarization p_{max} versus $|\zeta_s^{(5)}|$ in our *Lum* and I_c bands, and for our combined $Lum + I_c$-band in Fig. 3.2. Based on Fig. 3.4, Fig. 3.5 shows that the $Lum + I_c$ band yields $|\zeta_s^{(5)}|$ constraints ∼2-10 times more restrictive than the I_c band for the same observed polarization fraction, over the range $p_{max} \gtrsim 0.02$, (where $p_\star < p_{max}$), assuming negligible uncertainties, $\sigma_\star$.

3.2.3 CPT-Odd Vacuum Isotropic SME Models

Since jm are the angular quantum numbers with $-j \leq m \leq j$, with $j \leq d-2$, for each value of d, the number of distinct anisotropic vacuum dispersion and vacuum birefringent SME

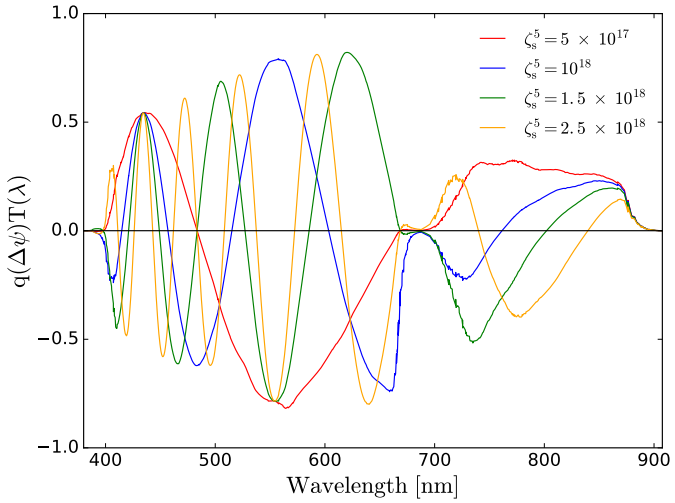

Figure 3.3: Change of the Stokes parameter $q^{(d)}_{(z_s)}$ from Eq. (3.9) for our combined $Lum + I_c$ filter in Fig. 3.2 for several values of $\zeta_s^{(5)}$. For comparison, see Fig. 2 of [40].

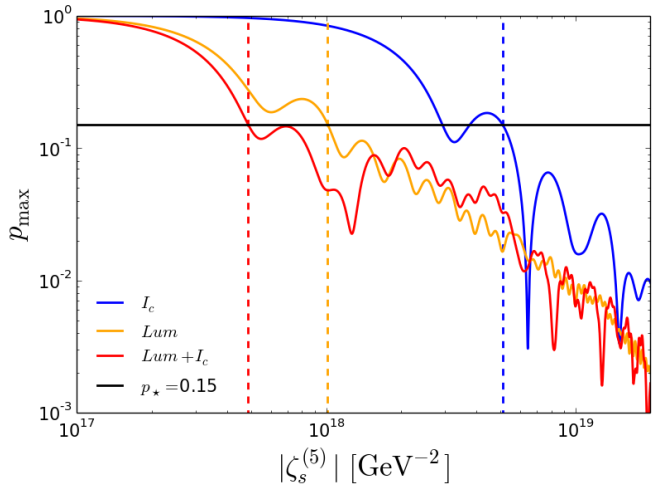

Figure 3.4: Maximum allowed polarization fraction p_{max} vs. $d = 5$ CPT-Odd Vacuum birefringence parameter $|\zeta_s^{(5)}|$ from Eq. (3.11) for the I_c-band (blue), Lum-band (orange), and our combined $Lum + I_c$-band (red).

For an example observed polarization fraction $p_\star = 0.15$ (horizontal black line), upper limits on $|\zeta_s^{(5)}|$ for each band (dashed vertical lines) can be obtained by noting that p_{max} eventually falls below the observed value of $p_\star$ for all values of that coefficient. For $p_\star \gtrsim 0.02$, the most stringent upper limit comes from the combined $Lum + I_c$-band. For $p_\star = 0.15$, this yields a $Lum + I_c$-band upper limit $|\zeta_s^{(5)}| \lesssim 5.0 \times 10^{17}$ GeV^{-2}, a factor of $\sim$10 better than the corresponding limit from the I_c band.

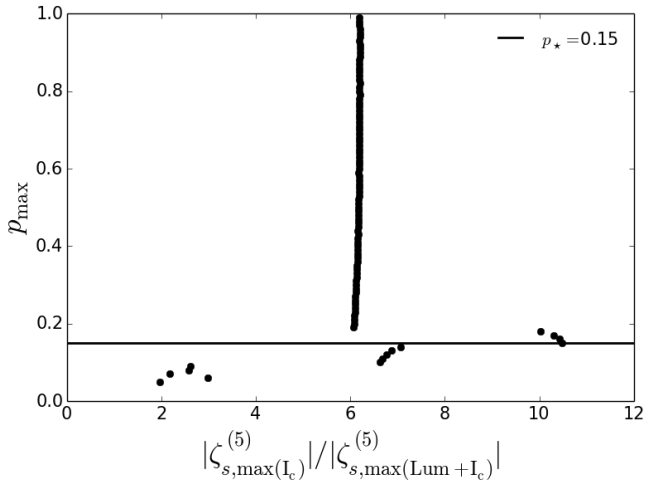

Figure 3.5: Theoretical maximum observed polarization p_{max} vs. the ratio of CPT-odd vacuum birefringent $d = 5$ SME coefficients from Fig. 3.4 from the I_c and $Lum + I_c$ bands, $|\zeta_s^{(5)}(I_c)|/|\zeta_s^{(5)}(Lum + I_c)|$.

Ignoring polarization uncertainties $\sigma_\star$, for all observed polarization fractions $p_\star \gtrsim 0.02$ (where $p_\star < p_{max}$), constraints from the $Lum + I_c$ band are ∼2-10 times tighter than for the I_c-band. The spike at $|\zeta_s^{(5)}(I_c)|/|\zeta_s^{(5)}(Lum + I_c)| \sim 6$ results from the fact that the ratio of the $|\zeta_s^{(5)}|$ values in each band (blue and red curves in Fig. 3.4) is nearly constant for $p_\star \gtrsim 0.17$.

coefficients increases as $(d-1)^2$ when d is CPT-odd and as $3(d-1)^2 - 8$ when d is CPT-even [39] (See Table II of [62]). For example, the $d = 5$ model has 16 SME coefficients [40]. Since we only observed two sources, we are limited to constraining only linear combinations of SME coefficients $c^{(d)}_{(I)jm}$ and $k^{(d)}_{(V)jm}$ along two specific lines of sight. Ultimately, progressively larger numbers of sources at different locations on the sky are required to better constrain the general anisotropic model space for a given value of d.

However, we can follow a simpler approach and also test the subset of isotropic models, which are recovered for each value of d when setting $j = m = 0$. Lines of sight to individual point sources are therefore most useful for constraining the isotropic SME coefficients $c^{(d)}_{(I)00}$ and $k^{(d)}_{(V)00}$, which correspond to some of the simplest LIV models in the literature [39, 62]. Constraints for both isotropic SME models and linear combinations along our specific lines of sight are shown in Table 3.2.

3.2.4 CPT-Even Vacuum Birefringent SME Models

There exists an additional subset of CPT-even vacuum birefringent SME models with coefficients $k^{(d)}_{(E)jm}$ and $k^{(d)}_{(B)jm}$, where $d = 4, 6, 8, \ldots$, which correspond to spin-2 helicity, rather than spin-0. Let us first define

$$\bar{k}^{(d)}_{(EB),s} \equiv \sum_{jm} {}_{\pm 2}Y_{jm,s}\left(k^{(d)}_{(E)jm} + ik^{(d)}_{(B)jm}\right), \tag{3.12}$$

as shorthand for the linear combination of CPT-even birefringent SME coefficients for source s. Note that there do not exist isotropic models for this subset of SME parameters so there are no $jm = 00$ terms corresponding to Eq. (3.12) [39]. The CPT-even case is also more complex than the CPT-odd case, because the normal modes are linearly polarized and, in general, can involve no change in the polarization angle, or mixing of linearly polarized into elliptical or circularly polarized modes [62].

Following, [39, 62], we now define the accumulated phase change Φ at a given energy E as

$$\Phi_s = 2E^{d-3}L^{(d)}_{(z_s)}\bar{k}^{(d)}_{(EB),s}\,. \tag{3.13}$$

In the CPT-odd vacuum birefringent case, this phase change directly resulted in a polarization angle rotation because we can split linearly polarized light equally into left and right circularly polarized states. But the same is not true of the CPT-even case. Linearly polarized light will not in general be split evenly between the normal modes of a CPT-even Lorentz violation.

But similar to the CPT-odd case, we can still arrive at an expression for the maximum allowed polarization given a particular broadband filter. Again assuming a 100% polarized source at all wavelengths, the observation of a linear polarization fraction $p_\star$ (with uncertainty $\sigma_\star$) in a given broad energy band can be used to constrain the quantity $\bar{k}^{(d)}_{(EB),s}$.

Following [62], let us first define the angle $\Psi = \psi_0 - \psi_b$ as the difference between

the initial polarization angle ψ_0 for light not produced in a normal mode and the initial polarization angle ψ_b for the slower of the two normal modes. For simplicity, we omit the source index s from the notation for Ψ, ψ_0, and ψ_b, since we will soon make assumptions which remove the Ψ dependence.

Additionally we can define $\langle \cos \Phi_s \rangle$ as the average value of $\cos \Phi_s$ for source s after integrating over the relevant energy band

$$\langle \cos \Phi_s \rangle \equiv \int_{E_1}^{E_2} \cos \left(2 \left(E^{d-3} - E_1^{d-3} \right) L_{(z_s)}^{(d)} \bar{k}_{(EB),s}^{(d)} \right) T(E) dE \,. \tag{3.14}$$

In this case, as shown in Appendix 3.6.1, the normalized Stokes parameters $q = q_{(z_s)}^{(d)}$ and $u = u_{(z_s)}^{(d)}$ are

$$q_{(z_s)}^{(d)} = \cos 2\Psi \cos 2\psi_b - \langle \cos \Phi_s \rangle^2 \sin 2\Psi \sin 2\psi_b \,, \tag{3.15}$$

$$u_{(z_s)}^{(d)} = \cos 2\Psi \sin 2\psi_b + \langle \cos \Phi_s \rangle^2 \sin 2\Psi \cos 2\psi_b \,, \tag{3.16}$$

and, via Eq. (3.10), the corresponding maximum limit on polarization is

$$\begin{aligned} & p_\star - 2\sigma_\star < p_{max,(z_s)}^{(d)} \\ & = \sqrt{1 - (1 - \langle \cos \Phi_s \rangle^2) \sin^2 2\Psi} \leq |\langle \cos \Phi_s \rangle| \,, \end{aligned} \tag{3.17}$$

where the conservative upper bound is reached when $\Psi = \pi/4$. Fig. 3.6 shows the corresponding limits obtained in this most conservative case.

Similar to Fig. 3.4, Fig. 3.6 shows limits from the theoretical maximum polarization p_{max} in our Lum, I_c, and $Lum + I_c$-bands versus the quantity $\zeta_s^{(6)}$, defined as

$$\zeta_s^{(6)} \equiv L_{(z_s)}^{(6)} \bar{k}_{(EB),s}^{(6)} \,. \tag{3.18}$$

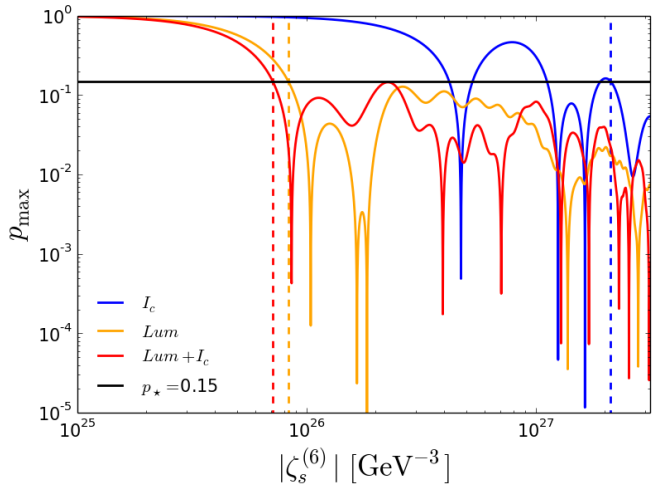

Figure 3.6: Similar to Fig. 3.4, but for p_{max} vs. the $d = 6$ CPT-Even Vacuum Birefringence parameter $|\zeta_s^{(6)}|$ from Eq. (3.18).

For an example observed polarization fraction $p_\star = 0.15$ (horizontal black line), the most stringent upper limit of $|\zeta_s^{(6)}| \lesssim 7 \times 10^{25}$ GeV^{-3} (dashed red line) comes from our combined $Lum + I_c$-band, a factor of ∼30 better than the corresponding limit from the I_c band (dashed blue line).

Again, similar to Fig. 3.5, Fig. 3.7 shows that the combined $Lum + I_c$-band yields $|\zeta_s^{(6)}|$ constraints up to ∼3-30 times more sensitive than the I_c-band.

3.2.5 Constraints on SME Models

With simultaneous photometric time series in two filter bands, one can estimate upper limits to any time delays (or early arrivals) between the corresponding light curves under the simple assumption that the intrinsic light curve shapes are identical. We perform this analysis on our entire photometric time series (see Tables 3.5-3.6 and Figs. 3.9-3.13) using an open source implementation of the Discrete Correlation Function (DCF) in Python[9], which can be used to analyze variable time series with arbitrary sampling [83] (see, for example [84]). Constraints from time delays are presented in Table 3.2, using the methods of §3.2.1.

We consider possible estimated time delays $\Delta t_\star = m_I - m_L$ between observed photometric light curves in the Lum and I_c bands. Since our data points have a typical 8-10

[9] `https://github.com/astronomerdamo/pydcf`

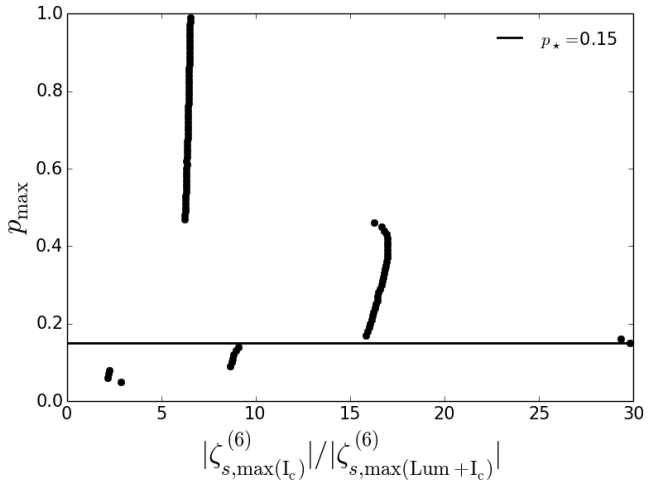

Figure 3.7: Similar to Fig. 3.5, but for p_{max} vs. the ratio of CPT-even vacuum birefringent $d = 6$ SME coefficients from Fig. 3.6 from the I_c and $Lum + I_c$ bands, $|\zeta_s^{(6)}(I_c)|/|\zeta_s^{(6)}(Lum + I_c)|$.

Again, ignoring polarization uncertainties $\sigma_\star$, for all observed polarization fractions $p_\star \gtrsim 0.1$ and for many values $p_\star < 0.1$ (where $p_\star < p_{max}$), constraints from the $Lum + I_c$ band are ∼3-30 times tighter than for the I_c-band.

minute cadence, we compute the best-fit DCF time delay using a series of DCF bin widths in the range $[5, 20]$ minutes with step size 0.1 minutes, while considering possible time delays or early arrivals in the range of $[-250, 250]$ minutes for both sources. The mean and standard deviation of the set of best fit DCF time delays then yields $\Delta t_\star = 26.5 \pm 19.5$ minutes and $\Delta t_\star = -5.1 \pm 3.3$ minutes for BL Lacertae and S5 B0716+714, respectively. Both are consistent with $\Delta t_\star = 0$, and thus no time delay, to within the 2-σ uncertainties. Using the 2-σ errors, and remaining agnostic as to the sign of $\Delta t^{(d)}_{(z_s)}$ leads to conservative time delay upper bounds of

$$|\Delta t_\star| \leq \max\{|\Delta t_\star - 2\sigma_{\Delta t_\star}|, |\Delta t_\star + 2\sigma_{\Delta t_\star}|\}\,, \tag{3.19}$$

which for the two sources yields $|\Delta t^{(d)}_{(z_s)}| \leq |\Delta t_\star| = 65.5$ minutes and 11.7 minutes, for BL Lacertae and S5 B0716+714, respectively.[10]

For a polarimetric time series measuring the polarization p in either the Lum, I_c, or combined $Lum + I_c$-bands, one can use the maximum observed polarization $p_\star$ during the

[10]The time delay upper limit for BL Lacertae is less stringent than the limit form S5 B0716+714 due mainly to the smaller number of data points.

observing period to place limits on the SME parameters as in §3.2.2-3.2.4, with an additional correction for systematic errors described in Sec. 3.3.1. While a longer survey could, in principle, yield larger values of $p_\star$, and thus, more stringent SME constraints, meaningful constraints can still be obtained for arbitrary values of $p_\star$, even though these are likely lower limits to the true maximum polarization. Constraints from maximum observed polarization measurements are presented in Table 3.2 for the *Lum* and I_c-bands, and in Table 3.3 for the combined $Lum + I_c$-bands.

Even though we observed only two low redshift sources with small telescopes, our best *Lum*-band $d = 5$ SME constraint from maximum polarization measurements of S5 B0716+714 at $z = 0.31 \pm 0.08$ in Tables 3.2-3.3, of $|\bar{k}^{(5)}_{(V)}| < 1 \times 10^{-23}$ GeV^{-1} is within an order of magnitude of all constraints for individual lines of sight from the 36 QSOs in the redshift range $z \in [0.634, 2.936]$ analyzed in Table II of [40], where their SME parameter $\gamma_{\rm max}$ corresponds to our parameter $|\bar{k}^{(5)}_{(V)}|$.[11] More specifically, our best $d = 5$ constraint is comparable to the least sensitive constraint $\gamma_{\rm max} < 9.79 \times 10^{-24}$ GeV^{-1} from Table II of [40] (for FIRST J21079-0620 with $p_\star = 1.12 \pm 0.22\%$ at $z = 0.644$), while our best constraint is only a factor of ∼10 less sensitive than the *best* constraint of $\gamma_{\rm max} < 0.97 \times 10^{-24}$ GeV^{-1} (for PKS 1256 – 229 with $p_\star = 22.32 \pm 0.15\%$ at $z = 1.365$). This is the case even though our analysis was arguably more conservative than [40], in regard to modeling our transmission functions, correcting for polarimetry systematics, and including uncertainties in the reported redshift measurements.

Note that the sources analyzed in [40] used linear polarization measurements from [78], which were observed using the 3.6-m telescope at the European Southern Observatory in La Silla, with the EFOSC2 polarimeter equipped with a V-band filter. As such, this work demonstrates that meaningful SME constraints for individual lines of sight — that are comparable to, or within a factor of 10 as sensitive as polarimetry constraints from a 3.6-m

[11] Our $Lum + I_c$, $\bar{k}^{(5)}_{(V)}$ constraint is actually a factor of ∼2 worse than our *Lum*-band constraint because the maximum observed polarization for the combined $Lum + I_c$ band data of $p_{\star,cor} = 7.83 \pm 0.38\%$ is slightly smaller than the *Lum* band measurement of $p_{\star,cor} = 9.77 \pm 0.52\%$. However, for the same value of $p_{\star,cor}$, the $Lum + Ic$ constraint will always be more sensitive than the *Lum* or I_c-band constraints alone.

telescope — can be readily obtained using a polarimetric $Lum + I_c$-band system of small telescopes with an effective 0.45-m aperture, with ∼64 times less collecting area, which we describe in Sec. 3.3.

Table 3.2: Upper limits on linear combinations of SME coefficients of Lorentz and CPT violation along specific lines of sight from our *Lum* and I_c-band observations of BL Lacertae and S5 B0716+714, with sky coordinates and redshifts from Table 3.1.

Source	S5 B0716+714		BL Lacertae	
(RA, DEC)	(110.47°, 71.34°)		(330.68°, 42.28°)	
Redshift z	0.31 ± 0.08		0.0686 ± 0.0004	
Time Delay Upper Bound	*Lum*-I_c		*Lum*-I_c	
$\lvert\Delta t_\star\rvert$ [minutes]	11.7		65.5	
$\lvert\bar{c}^{(6)}_{(I)}\rvert$	$< 6 \times 10^{+01}$ GeV^{-2}		$< 8 \times 10^{+02}$ GeV^{-2}	
$\lvert\bar{c}^{(8)}_{(I)}\rvert$	$< 8 \times 10^{+18}$ GeV^{-4}		$< 1 \times 10^{+20}$ GeV^{-4}	
$\lvert c^{(6)}_{(I)00}\rvert$	$< 2 \times 10^{+02}$ GeV^{-2}		$< 3 \times 10^{+03}$ GeV^{-2}	
$\lvert c^{(8)}_{(I)00}\rvert$	$< 3 \times 10^{+19}$ GeV^{-4}		$< 4 \times 10^{+20}$ GeV^{-4}	
Max. Obs. Polarization	*Lum*	I_c	*Lum*	I_c
$p_\star$ [%]	10.02 ± 0.44	8.30 ± 0.48	10.33 ± 0.43	10.50 ± 0.30
$p_{\rm sys,ISP}$ [%]	0.21 ± 0.27	0.77 ± 0.23	0.92 ± 0.07	0.46 ± 0.07
$p_{\rm sys,int}$ [%]	0.04	0.04	0.04	0.04
$p_{\star,cor}$ [%]	9.77 ± 0.52	7.49 ± 0.53	9.37 ± 0.44	10.00 ± 0.31
$\lvert\bar{k}^{(5)}_{(V)}\rvert$	$< 1 \times 10^{-23}$ GeV^{-1}	$< 7 \times 10^{-23}$ GeV^{-1}	$< 3 \times 10^{-23}$ GeV^{-1}	$< 1 \times 10^{-22}$ GeV^{-1}
$\lvert\bar{k}^{(7)}_{(V)}\rvert$	$< 2 \times 10^{-6}$ GeV^{-3}	$< 1 \times 10^{-5}$ GeV^{-3}	$< 4 \times 10^{-6}$ GeV^{-3}	$< 2 \times 10^{-5}$ GeV^{-3}
$\lvert\bar{k}^{(9)}_{(V)}\rvert$	$< 3 \times 10^{+11}$ GeV^{-5}	$< 4 \times 10^{+12}$ GeV^{-5}	$< 8 \times 10^{+11}$ GeV^{-5}	$< 6 \times 10^{+12}$ GeV^{-5}
$\lvert k^{(5)}_{(V)00}\rvert$	$< 5 \times 10^{-23}$ GeV^{-1}	$< 3 \times 10^{-22}$ GeV^{-1}	$< 1 \times 10^{-22}$ GeV^{-1}	$< 4 \times 10^{-22}$ GeV^{-1}
$\lvert k^{(7)}_{(V)00}\rvert$	$< 6 \times 10^{-6}$ GeV^{-3}	$< 3 \times 10^{-5}$ GeV^{-3}	$< 2 \times 10^{-5}$ GeV^{-3}	$< 8 \times 10^{-5}$ GeV^{-3}
$\lvert k^{(9)}_{(V)00}\rvert$	$< 1 \times 10^{+12}$ GeV^{-5}	$< 1 \times 10^{+13}$ GeV^{-5}	$< 3 \times 10^{+12}$ GeV^{-5}	$< 2 \times 10^{+13}$ GeV^{-5}
$\lvert\bar{k}^{(4)}_{(EB)}\rvert$	$\lesssim 7 \times 10^{-32}$	$\lesssim 2 \times 10^{-31}$	$\lesssim 2 \times 10^{-31}$	$\lesssim 3 \times 10^{-31}$
$\lvert\bar{k}^{(6)}_{(EB)}\rvert$	$\lesssim 5 \times 10^{-15}$ GeV^{-2}	$\lesssim 2 \times 10^{-14}$ GeV^{-2}	$\lesssim 1 \times 10^{-14}$ GeV^{-2}	$\lesssim 5 \times 10^{-14}$ GeV^{-2}
$\lvert\bar{k}^{(8)}_{(EB)}\rvert$	$\lesssim 2 \times 10^{+2}$ GeV^{-4}	$\lesssim 5 \times 10^{+3}$ GeV^{-4}	$\lesssim 4 \times 10^{+2}$ GeV^{-4}	$\lesssim 1 \times 10^{+4}$ GeV^{-4}

The upper portion of the table shows the vacuum dispersion coefficients $|\bar{c}^{(d)}_{(I)}|$ and corresponding isotropic coefficients $|c^{(d)}_{(I)00}|$ (see Fig. 3.1) as inferred from estimates of an upper bound on the time delay $\Delta t_\star$ between the observed photometry in both the *Lum* and I_c-bands as described in Sec. 3.2.5. The remaining rows show separate constraints from the maximum observed polarization fraction $p_\star$, which we correct for systematics from interstellar polarization ($p_{\rm sys,ISP}$) and instrumental polarization and zero point bias ($p_{\rm sys,inst}$), in each band via $p_{\star,cor} = p_\star - p_{\rm sys,ISP} - p_{\rm sys,inst}$, with corresponding statistical errors added in quadrature. To be conservative, we derive SME parameter upper bounds using the 2-σ errors for $\Delta t_\star$, $p_{\star,cor}$, and Redshift z. The lower rows show the vacuum birefringent coefficients $|\bar{k}^{(d)}_{(V)}|$ and their corresponding isotropic coefficients $|k^{(d)}_{(V)00}|$, each for the CPT-odd cases $d = 5, 7, 9$. The last three rows show the vacuum birefringence coefficients $|\bar{k}^{(d)}_{(EB)}|$ for the CPT-even cases $d = 4, 6, 8$. In each case, constraints from our observed broadband polarimetry using the wider *Lum*-band are tighter than for the I_c-band.

Table 3.3: Same as SME coefficient limits from maximum observed polarization from Table 3.2, but for the combined $Lum{+}I_c$-band (see Fig. 3.2).

Source	S5 B0716+714	BL Lacertae
(RA, DEC)	(110.47°, 71.34°)	(330.68°, 42.28°)
Redshift z	0.31 ± 0.08	0.0686 ± 0.0004
Maximum Observed Polarization	$Lum + I_c$	$Lum + I_c$
$p_\star$ [%]	8.64 ± 0.30	10.30 ± 0.28
$p_{\rm sys,ISP}$ [%]	0.77 ± 0.23	0.92 ± 0.07
$p_{\rm sys,inst}$ [%]	0.04	0.04
$p_{\star,cor}$ [%]	7.83 ± 0.38	9.34 ± 0.29
$\lvert\bar{k}^{(5)}_{(V)}\rvert \equiv \lvert\sum_{jm} Y_{jm}(\theta,\phi) k^{(5)}_{(V)jm}\rvert$	$< 2 \times 10^{-23}$ GeV^{-1}	$< 5 \times 10^{-23}$ GeV^{-1}
$\lvert\bar{k}^{(7)}_{(V)}\rvert \equiv \lvert\sum_{jm} Y_{jm}(\theta,\phi) k^{(7)}_{(V)jm}\rvert$	$< 4 \times 10^{-6}$ GeV^{-3}	$< 8 \times 10^{-6}$ GeV^{-3}
$\lvert\bar{k}^{(9)}_{(V)}\rvert \equiv \lvert\sum_{jm} Y_{jm}(\theta,\phi) k^{(9)}_{(V)jm}\rvert$	$< 8 \times 10^{+11}$ GeV^{-5}	$< 2 \times 10^{+12}$ GeV^{-5}
$\lvert k^{(5)}_{(V)00}\rvert$	$< 9 \times 10^{-23}$ GeV^{-1}	$< 2 \times 10^{-22}$ GeV^{-1}
$\lvert k^{(7)}_{(V)00}\rvert$	$< 1 \times 10^{-5}$ GeV^{-3}	$< 3 \times 10^{-5}$ GeV^{-3}
$\lvert k^{(9)}_{(V)00}\rvert$	$< 3 \times 10^{+12}$ GeV^{-5}	$< 7 \times 10^{+12}$ GeV^{-5}
$\lvert\bar{k}^{(4)}_{(EB)}\rvert \equiv \lvert\sum_{jm} {}_2Y_{jm}(\theta,\phi)(k^{(4)}_{(E)jm} + ik^{(4)}_{(B)jm})\rvert$	$\lesssim 8 \times 10^{-32}$	$\lesssim 2 \times 10^{-31}$
$\lvert\bar{k}^{(6)}_{(EB)}\rvert \equiv \lvert\sum_{jm} {}_2Y_{jm}(\theta,\phi)(k^{(6)}_{(E)jm} + ik^{(6)}_{(B)jm})\rvert$	$\lesssim 9 \times 10^{-15}$ GeV^{-2}	$\lesssim 5 \times 10^{-15}$ GeV^{-2}
$\lvert\bar{k}^{(8)}_{(EB)}\rvert \equiv \lvert\sum_{jm} {}_2Y_{jm}(\theta,\phi)(k^{(8)}_{(E)jm} + ik^{(8)}_{(B)jm})\rvert$	$\lesssim 2 \times 10^{+2}$ GeV^{-4}	$\lesssim 4 \times 10^{+2}$ GeV^{-4}

3.3 The Array Photo Polarimeter

The observing system used in this work, the Array Photo Polarimeter (APPOL) — maintained and operated by one of us (G. Cole) — uses dual beam inversion optical polarimetry with Savart plate analyzers rotated through an image sequence with various half-wave-plate (HWP) positions. See [85, 86, 87] for the basic procedures underlying dual beam polarimetry. This approach can be contrasted with quadruple beam analyzers with Wollaston prisms such as RoboPol (e.g. [88, 89, 90]) that can obtain all the Stokes parameters in a suitably calibrated single image.

The APPOL array employs an automated telescope, filter, and instrument control system with 5 co-located telescopes on two mounts. APPOL uses two small, Celestron 11 and 14 inch, primary telescopes (C11 and C14) for polarimetry with an effective collecting area equivalent to a larger 17.8 inch (0.45-m) telescope, with added capability to obtain simultaneous photometry or polarimetry on a third smaller telescope (Celestron 8 inch = C8), along with bright star photometry and/or guiding using a fourth and fifth 5 inch telescope.

APPOL is located at StarPhysics Observatory (Reno, Nevada) at an elevation of 1585 meters.

Earlier iterations of APPOL (e.g. [91]) have been progressively equipped with new automated instrumentation and image reduction software [92, 93, 94], and used for spectropolarimetry studies [95, 96], including a long observing campaign presenting polarimetry and photometry of the variable star Epsilon Aurigae [97, 98, 99]. APPOL's polarimeter designs also helped inform the planning and hardware implementation of the University of Denver DUSTPol instrument, an optical polarimeter with low instrumental polarization that has been used to study cool star systems, including RS CVn systems and Wolf-Rayet stars [100].

The first row of Fig. 3.8 shows the inputs to the total transmission vs. wavelength $T(\lambda)$ in Fig. 3.2 for our Lum and I_c-band polarimetry using APPOL, which can be used to compute $T(E)$ as used in § 3.2.2-3.2.5. The APPOL setup used in this work and the associated polarimetry data reduction and analysis methods will be described in more detail in a companion paper [101].

3.3.1 Observations and Systematics

All data in this paper were observed with APPOL over a short campaign in December 2017 - January 2018. Samples of the observed data for BL Lacertae and S5 B0716+714 are shown in Appendix 3.6.2 in Tables 3.5-3.6, with the full machine-readable polarimetry and photometry data available online and plotted in Figs. 3.9-3.11 for BL Lacertae and in Figs. 3.12-3.14 for S5 B0716+714. Image sequences with detected cosmic rays were identified as outliers and excluded. While we only use the maximum observed polarization to constrain birefringent SME models, we include the entire time series for completeness. By contrast, the full photometric time series was used to constrain the vacuum dispersion SME models using estimated time delays.

Optical photometric and polarimetric variability, correlations between flux and color, and searches for intra-band photometric time lags, have been studied extensively in the literature for AGN and BL Lacertae type objects [78, 102, 103, 104, 105, 106], including the

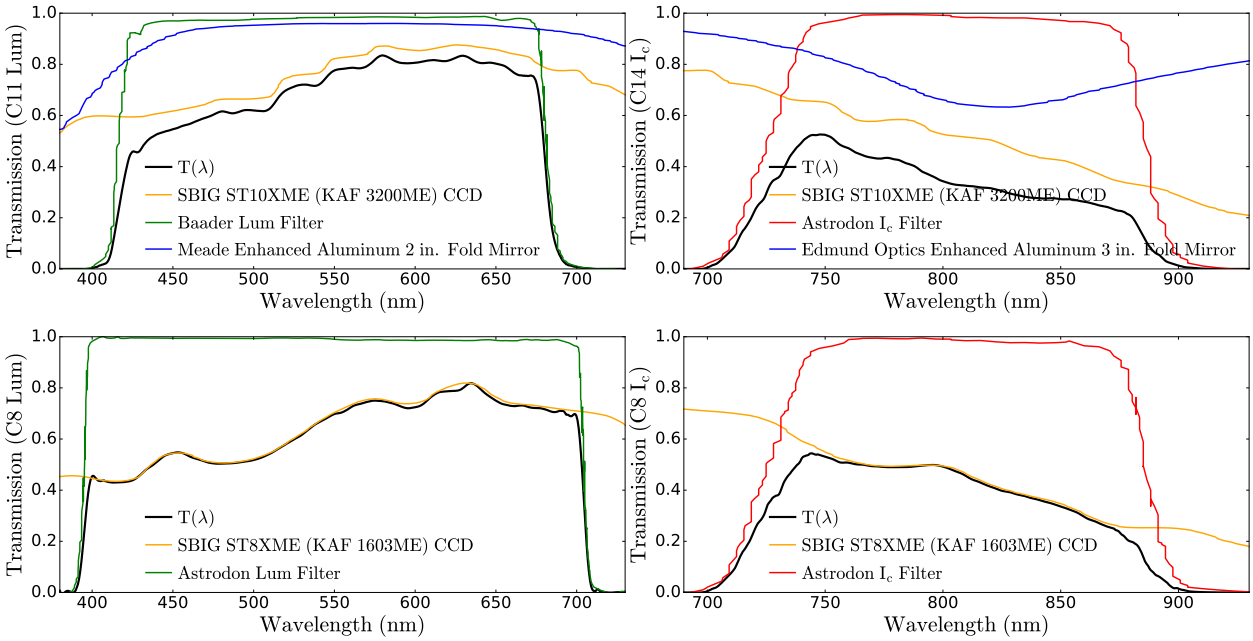

Figure 3.8: Array Photo Polarimeter transmission functions for the relevant optical components, filters, and CCD detectors.

The first row shows the C11 and C14 telescopes used for polarimetry in the *Lum* and I_c bands, respectively. The second row shows the C8 telescope used for photometry in both the I_c and *Lum* bands. The black curve shows $T(\lambda)$, the total transmission function, which can be used to compute $T(E)$ to constrain the SME parameters via maximum polarization measurements as in § 3.2.2-3.2.5. To simplify the analysis, we do not model the transmission functions of the Celestron StarBright coatings. We also do not model the transmission functions of the Savart Plates and the half-wave plates, which are fairly uniform throughout the relevant wavelength range. For similar reasons, we also neglect the atmospheric transmission and the source spectra. By comparison, the analysis in [40] only included the filter transmission function.

specific, well known AGN sources we observed: BL Lacertae [107, 108, 109, 110], and S5 B0716+714 [111, 112, 113, 114, 115, 116, 117, 118, 119]. Our analysis is restricted to testing SME models, but our photometric and polarimetric time series could be analyzed similarly in future work.[12]

Our data reduction pipeline removes systematic instrumental polarization using secondary flat-field self-calibration from the two sets of images taken at the 4 half wave plate positions (0°, 22.5°) and (45°, 67.5°), respectively, following [87]. Hundreds of previous APPOL measurements of unpolarized standard stars indicate that this procedure yields instrumental polarization systematics $\lesssim 0.03\%$ for targets with sufficient flux, while zero-point bias adjustments are typically $\lesssim 0.01\%$ for observed APPOL polarization fractions of greater than a few percent [98].[13] The APPOL HWP waveplate modulation efficiencies have been measured to be $\gtrsim 97\%$ and $\sim 90\%$ for Lum and I_c, respectively. Since imperfect modulation efficiency can only reduce the maximum observed polarization from its true value, to be conservative, we choose not to model these systematics here.[14] Previous tests indicate that other potential systematics including coordinate frame misalignment are negligible for APPOL [98].

The total optical polarization along arbitrary lines of sight toward galactic field stars can range from a fraction of a percent to several percent [126, 127, 128]. Previous work from the Large Interstellar Polarization Survey provided evidence that interstellar polarization (ISP) from multiple dust clouds along a given line of sight is smaller than from lines of sight passing through a single dust cloud [129, 128]. Since the presence of two or more clouds would therefore depolarize the incoming radiation, we assume that the ISP along the line of sight toward a galactic field star represents a conservative upper limit to the true ISP toward an AGN source that would have been measured through the full dust column of the galaxy,

[12]For reviews of the many other applications of optical polarimetry, see for example, [120, 121, 122, 123, 124, 125].

[13]We assume the same systematic error budget of 0.04% for the Lum, I_c, and $Lum + I_c$ bands including instrumental polarization and zero-point bias.

[14]HWP modulation efficiency systematics would not effect the measured polarization angles, although other relevant systematics are discussed in [98].

Table 3.4: Polarization measurements p_L (Lum) and p_I (I_c)

Star #	GAIA DR2 ID	RA IRCS(J2000)°	DEC IRCS(J2000)°	p_L (%)	p_I (%)
BL Lacertae					
1	1960066324769508992	330.68924090	+42.27652024	1.01 ± 0.03	0.55 ± 0.03
2	1960066329068001536	330.69304715	+42.28231354	0.92 ± 0.07	0.46 ± 0.07
S5 B0716+714					
1	1111278261916148224	110.47651216	+71.32247695	0.26 ± 0.43	0.89 ± 0.73
2	1111278158836933888	110.46803636	+71.30492029	0.21 ± 0.27	0.77 ± 0.23

Polarization measurements p_L (Lum) and p_I (I_c) of field stars in sample image sequences within 3 arcmin of the AGN sources BL Lacertae and S5 B0716+714, used to estimate upper limits on interstellar polarization for the systematic error budget used in Tables 3.2-3.3. Celestial coordinates and GAIA DR2 identifiers from Simbad/VizieR are included.

the intergalactic medium, and the AGN host galaxy.

Using a sample image sequence for each of our two AGN targets, we performed Lum and I_c-band polarimetry on the two closest field stars within 3 arcmin of the target AGN, finding polarizations of $1.01 \pm 0.03\%$ and $0.92 \pm 0.07\%$ in Lum and $0.55 \pm 0.03\%$ and $0.46 \pm 0.07\%$ in I_c for the field of BL Lacertae and $0.26 \pm 0.43\%$ and $0.21 \pm 0.27\%$ in Lum and $0.89 \pm 0.73\%$ and $0.77 \pm 0.23\%$ in I_c for the field of S5 B0716+714. See Table 3.4. For the combined $Lum + I_c$ band maximum polarization measurements, we use the largest ISP measurement from the Lum and I_c bands.

Assuming that our AGN max polarization measurements arise from a combination of instrumental polarization, zero point bias, ISP, and intrinsic source polarization, and that the ISP is approximately constant within 3 arcmin of the AGN target line of sight, we use the smaller of the two measured stellar polarizations to estimate conservative systematic upper limits for ISP ($p_{\rm sys,ISP}$) as listed in Tables 3.2-3.3. Finally, to obtain a polarization estimate corrected for systematics, $p_{\star,cor}$, we subtract these systematic error estimates for ISP ($p_{\rm sys,ISP}$) as well as the 0.04% systematic budget from instrumental polarization and zero point bias ($p_{\rm sys,inst}$) from our maximum observed polarization in the I_c, Lum, and $Lum + I_c$-bands to

obtain the SME constraints in Tables 3.2-3.3.[15]

3.4 Conclusions

In this work, we performed optical polarimetry and photometry of two well known AGN sources, BL Lacertae and S5 B0716+714 in both the Lum and I_c-bands, while implementing a procedure to obtain polarimetry in a wider effective passband with coverage from ∼400-900 nm by combining simultaneous photometry from two small, co-located telescopes. We used the "average polarization" method of [40], which analyzed polarimetric measurements from the literature, to analyze our own polarimetric measurements, thereby demonstrating a proof-of-principle method to use our own data to derive meaningful constraints, for individual lines of sight or isotropic models, on parameters from various subsets of the Standard Model Extension, a useful framework to test for new physics beyond the Standard Model including potential violation of Lorentz and CPT Invariance [39]. We demonstrated that maximum polarization measurements with our wider effective $Lum + I_c$ bandpass can yield SME constraints that are up to ∼10 or ∼30 times more sensitive that with our I_c-band filter, for $d = 5$ and $d = 6$ models, respectively.

To constrain SME parameters for a single source along a single line of sight, optical photometric measurements of AGN are not competitive with GRB gamma-ray and x-ray measurements in regard to timing resolution, energy, and redshift. Therefore, high energy GRB measurements are the best way to constrain SME parameters using observed time delays at different observed energies. Nevertheless, GRBs are transients both in their prompt gamma-ray emission and optical afterglows. Therefore, since AGN are the brightest continuous optical sources at cosmological distances, it is considerably easier to quickly obtain more complete sky coverage by observing many more AGN, in order to better constrain the anisotropic vacuum dispersion SME models. In addition, compared with gamma and x-ray polarimetry, optical

[15]Statistical errors from the polarization measurements for the AGN source and stars used to estimate ISP systematics are added in quadrature.

polarimetric measurements typically have smaller statistical uncertainties and independent systematics [40]. Optical polarimetry is also easier to obtain with ground based instruments than gamma-ray and x-ray polarimetry, which must be obtained from space (e.g. [61]).

Although the limits presented here were not intended to compete with other approaches using maximum polarization measurements integrated over an optical bandpass, the pilot program in this work nevertheless demonstrates that meaningful SME constraints can be obtained even with a small set of telescopes with an effective 0.45-m aperture, that are competitive — to within a factor of ∼1-10 in sensitivity for $d = 5$ models — even when compared to optical polarimetry from a 3.6-m telescope [78, 40]. Since $d = 6$ models were not analyzed in [40], it would be interesting to perform similar comparisons to our $d = 6$ constraints in future work, along with comparisons to the $d = 4$ models analyzed in [130]. As such, there is a strong science case to use the maximum observed polarization for a large sample of AGN with wide optical bandpasses to constrain the anisotropic vacuum birefringent SME models, which include the three families of other SME coefficients not constrained by time delay measurements.

Future work could improve upon existing SME constraints simply by using the methods in this work to analyze optical polarimetry from large published surveys of AGN and quasars (e.g [131, 132]) in addition to the AGN and GRB afterglow sources already studied by [40, 130]. In addition, state-of-the-art SME constraints could potentially be obtained by performing a new survey to significantly increase the number of high redshift sources with published optical polarimetry along independent lines of sight. The pilot program described in this work thus serves to motivate a dedicated optical AGN polarimetric survey similar to the Steward Observatory spectrapolarimetric AGN monitoring program [78], the RoboPol survey of gamma-ray selected blazars [88, 133, 131], or the La Silla Observatory survey of optical linear polarization of QSOs [78, 132], to name some relevant examples.

Such future surveys would obtain broadband optical polarimetry of each AGN source with a set of filters, optics, and detectors optimally chosen to improve upon the SME

constraints obtainable using the more standard optical filters employed by previous surveys. In addition to measuring sources along lines of sight without previously published polarimetry, where possible, polarimetric measurements of previously observed sources could still lead to tighter SME constraints by either observing a larger maximum polarization than what was reported in the literature, or by observing with a wider optical bandpass.

By duplicating this setup on one or more 1-meter class telescopes in each hemisphere, using the same data reduction software, such a survey could achieve the full sky coverage needed to fully constrain the more general anisotropic SME models at increasingly larger mass dimension $d \geq 4$. However, unlike previous surveys, it may only be necessary to observe a short duration time series for each AGN source, in order to maximize the number of sources with maximum polarization measurements, thereby optimizing a to-be-determined figure of merit which would quantify the improvement in constraints for specific SME models, during a given survey time period.

Since spectropolarimetry typically yields SME $d = 5$ model parameter constraints that are $\sim$2-3 orders of magnitude more sensitive than using a single, broadband, optical filter [40], it would also be interesting to investigate the costs and benefits of a full spectropolarimetric survey on $\gtrsim$ 2-m class telescopes versus a less expensive, shorter duration, survey on a set of 1-m class telescopes using multiple optical filters to test $d \geq 4$ SME models. Similarly, it would be worthwhile in future work to explore the tradeoffs for constraining SME models by using multiple, non-overlapping, narrow-band, optical filters to effectively perform low resolution spectropolarimetry versus combining two or more filters into a single, broadband filter, as demonstrated in this work.

Design feasibility studies for such a proposed survey will be analyzed in future work, with emphasis on the best path to quickly achieve the largest payoff for astrophysical tests of CPT and Lorentz Invariance violation without the time and expense required to perform an all sky spectrapolarimetric survey.

3.5 Acknowledgments

This work was originally inspired in part by conversations with Chris Stubbs. We thank Calvin Leung for sharing code to help compute transmission functions. A.S.F. acknowledges support from NSF INSPIRE Award PHYS 1541160. B.G.K. acknowledges support from UCSD's Ax Center for Experimental Cosmology. We gratefully made use of the NASA/IPAC Extragalactic Database (NED), which is operated by the Jet Propulsion Laboratory, California Institute of Technology, under contract with NASA. This research also made use of the Simbad and VizieR databases, operated at CDS, Strasbourg, France. We also acknowledge extensive use of the HPOL spectropolarimetric database, "http://www.sal.wisc.edu/HPOL/" for instrument development and calibration. We further acknowledge the variable star observations from the AAVSO International Database contributed by observers worldwide and used in this research.

Chapter 3, in full, is a reprint of material as it appears in A.S. Friedman, D. Leon, K.D. Crowley, D. Johnson, G. Teply, D. Tytler, B.G. Keating, and G.M. Cole, "Constraints on Lorentz invariance and CPT violation using optical photometry and polarimetry of active galaxies BL Lacertae and S5 B0716+714," Phys. Rev. D, 99, 035045, 2019 (arXiv:1809.08356) [2]. The dissertation author made essential contributions to this work.

3.6 Appendix

3.6.1 CPT-Even Q and U

We can calculate the Stokes Q and U parameters in the presence of CPT-even SME coefficients of the form $\bar{k}^{(d)}_{(EB),s}$ as defined in Eq. (3.12). As was written in Eq. (3.13), the phase delay between the two normal modes is given by the equation

$$\Phi(\omega) = 2\omega^{d-3} L^{(d)} \bar{k}^{(d)}_{(EB),s} \,, \tag{3.20}$$

where we denote the energy as ω as opposed to E in this case to distinguish it from the electric field.

The most conservative limits on SME coefficients are obtained when we assume a broadband source emitting a uniformly linearly polarized electric field along our line of sight $\hat{z}$ in the form

$$\vec{E}(\omega, t) = Ae^{i\omega t}\hat{n}\,, \tag{3.21}$$

where $\hat{n}$ makes an angle ψ_0 with respect to the detector reference angle. Then if the slow axis of this CPT-even Lorentz violation makes an angle ψ_b with respect to the detector reference angle so that we can define the quantity

$$\Psi = \psi_0 - \psi_b\,, \tag{3.22}$$

then the signal that reaches our detector along the slow and fast axes can be written

$$E_{slow}(\omega, t) = Ae^{i\omega t - i\Phi/2}\cos\Psi\,, \tag{3.23}$$

$$E_{fast}(\omega, t) = Ae^{i\omega t + i\Phi/2}\sin\Psi\,, \tag{3.24}$$

which, relative to our detector, is the electric field

$$\begin{aligned}\vec{E}(\omega, t) &= Ae^{i\omega t}\left[e^{-i\Phi/2}\cos\Psi\cos\psi_b - e^{i\Phi/2}\sin\Psi\sin\psi_b\right]\hat{x} \\ &+ Ae^{i\omega t}\left[e^{-i\Phi/2}\cos\Psi\sin\psi_b + e^{i\Phi/2}\sin\Psi\cos\psi_b\right]\hat{y}\,.\end{aligned} \tag{3.25}$$

Next we can define averaging over the transmission band $T(\omega)$ as the operation

$$\langle X\rangle_\omega = \frac{\int d\omega T(\omega)X(\omega)}{\int d\omega T(\omega)}\,, \tag{3.26}$$

so that the Stokes parameters in terms of the band averaged electric field $\vec{E}(t) = \left\langle \vec{E}(\omega, t) \right\rangle_\omega$ incident on our detector are

$$
\begin{aligned}
I &= |E_x|^2 + |E_y|^2 = |A|^2 \,, && (3.27)\\
Q &= |E_x|^2 - |E_y|^2 && (3.28)\\
&= I \cos 2\Psi \cos 2\psi_b - I |\left\langle \cos\Phi \right\rangle|^2 \sin 2\Psi \sin 2\psi_b \,, \\
U &= 2\ \mathrm{Re}(E_x E_y^*) && (3.29)\\
&= I \cos 2\Psi \sin 2\psi_b + I |\left\langle \cos\Phi \right\rangle|^2 \sin 2\Psi \cos 2\psi_b \,, \\
V &= 2\ \mathrm{Im}(E_x E_y^*) = I |\left\langle \sin\Phi \right\rangle|^2 \sin 2\Psi \,, && (3.30)
\end{aligned}
$$

therefore the normalized Stokes parameters $q = Q/I, u = U/I$ and total linear polarization fraction p are

$$
\begin{aligned}
q &= \cos 2\Psi \cos 2\psi_b - |\left\langle \cos\Phi \right\rangle|^2 \sin 2\Psi \sin 2\psi_b \,, && (3.31)\\
u &= \cos 2\Psi \sin 2\psi_b + |\left\langle \cos\Phi \right\rangle|^2 \sin 2\Psi \cos 2\psi_b \,, && (3.32)\\
p &= \sqrt{\cos^2 2\Psi + \left\langle \cos\Phi \right\rangle^2 \sin^2 2\Psi} \,. && (3.33)
\end{aligned}
$$

Due to the many unknowns in Eqs. (3.33), it is impractical to use time delays between each q and u time series, for example, to constrain SME vacuum birefringent parameters. Circular polarization measurements could potentially break certain degeneracies, but the maximum observed polarization approach will, in general, yield more sensitive SME constraints than any approaches using optical time delays.

3.6.2 Data Plots and Tables

All data in this paper were observed with APPOL during December 2017 - January 2018. Samples of the observed data for BL Lacertae and S5 B0716+714 are shown in Tables 3.5-3.8, with the full machine-readable data to be made available online at the journal

website. Polarimetry is plotted in Figs. 3.9-3.10 for BL Lacertae and in Figs. 3.12-3.13 for S5 B0716+714, with photometry in Figs. 3.11 and 3.14, respectively.

Table 3.5: Three nights of data for BL Lacertae were observed using APPOL on December 13, 14, and 17, 2017.

MJD (days)	p_L (%)	p_I (%)	ψ_L (deg)	ψ_I (deg)	q_L (%)	q_I (%)	u_L (%)	u_I (%)	m_L (mag)	m_I (mag)
58101.072	10.3 ± 0.6	9.5 ± 0.4	59.0 ± 2.0	59.0 ± 1.0	-4.9 ± 0.6	-4.4 ± 0.4	9.0 ± 0.5	8.4 ± 0.4	13.69 ± 0.03	12.93 ± 0.04
58101.079	9.0 ± 0.4	7.7 ± 0.3	63.0 ± 1.0	58.0 ± 1.0	-5.2 ± 0.4	-3.4 ± 0.3	7.3 ± 0.4	6.9 ± 0.3	13.82 ± 0.03	12.96 ± 0.04
58101.085	8.2 ± 0.4	7.9 ± 0.3	60.0 ± 1.0	59.0 ± 1.0	-4.1 ± 0.4	-3.7 ± 0.3	7.1 ± 0.4	7.0 ± 0.3	13.74 ± 0.03	12.95 ± 0.04

For each Modified Julian Date (MJD), we show our observed polarimetric and photometric data for both the Lum and I_c-bands, denoted by L and I subscripts, respectively. Columns include the observed polarization p (in %), the polarization angle ψ (in degrees), the intensity normalized Stokes parameters q and u (note that both can be negative, even when expressed as percentages), and the observed magnitude m. (A portion of this table is shown for guidance. This table is available in its entirety in machine-readable form.)

Table 3.6: Same as Table 3.5 but all data for S5 B0716+714, for which we observed data using APPOL over five nights on December 11-14 2017 and January 1, 2018. (A portion of this table is shown for guidance. This table is available in its entirety in machine-readable form.)

MJD (days)	p_L (%)	p_I (%)	ψ_L (deg)	ψ_I (deg)	q_L (%)	q_I (%)	u_L (%)	u_I (%)	m_L (mag)	m_I (mag)
58099.300	8.8 ± 0.7	8.3 ± 0.5	88.0 ± 2.0	92.0 ± 2.0	-8.8 ± 0.7	-8.3 ± 0.5	0.8 ± 0.7	-0.7 ± 0.5	14.93 ± 0.04	14.39 ± 0.05
58099.306	6.9 ± 0.7	5.3 ± 0.5	81.0 ± 3.0	88.0 ± 3.0	-6.6 ± 0.7	-5.3 ± 0.5	2.1 ± 0.8	0.3 ± 0.6	15.00 ± 0.04	14.39 ± 0.05
58099.319	8.5 ± 0.7	7.6 ± 0.5	84.0 ± 2.0	88.0 ± 2.0	-8.3 ± 0.7	-7.6 ± 0.5	1.9 ± 0.7	0.6 ± 0.5	14.93 ± 0.04	14.32 ± 0.05

Table 3.7: Same as Table 3.5 for BL Lacertae, but for the combined $Lum + I_c$-band. (A portion of this table is shown for guidance. This table is available in its entirety in machine-readable form.)

MJD (days)	p_{L+I} (%)	ψ_{L+I} (deg)	q_{L+I} (%)	u_{L+I} (%)
58101.072	9.9 ± 0.4	59.0 ± 1.0	-4.7 ± 0.4	8.8 ± 0.4
58101.079	8.4 ± 0.3	61.0 ± 1.0	-4.5 ± 0.3	7.1 ± 0.3
58101.085	8.1 ± 0.3	59.5 ± 0.9	-3.9 ± 0.3	7.1 ± 0.3

3.6.3 Linear Combination Notation

We have defined a shorthand notation for linear combinations of the SME coefficients throughout this work. In particular we use them in Table 3.2, and note here that they are defined as

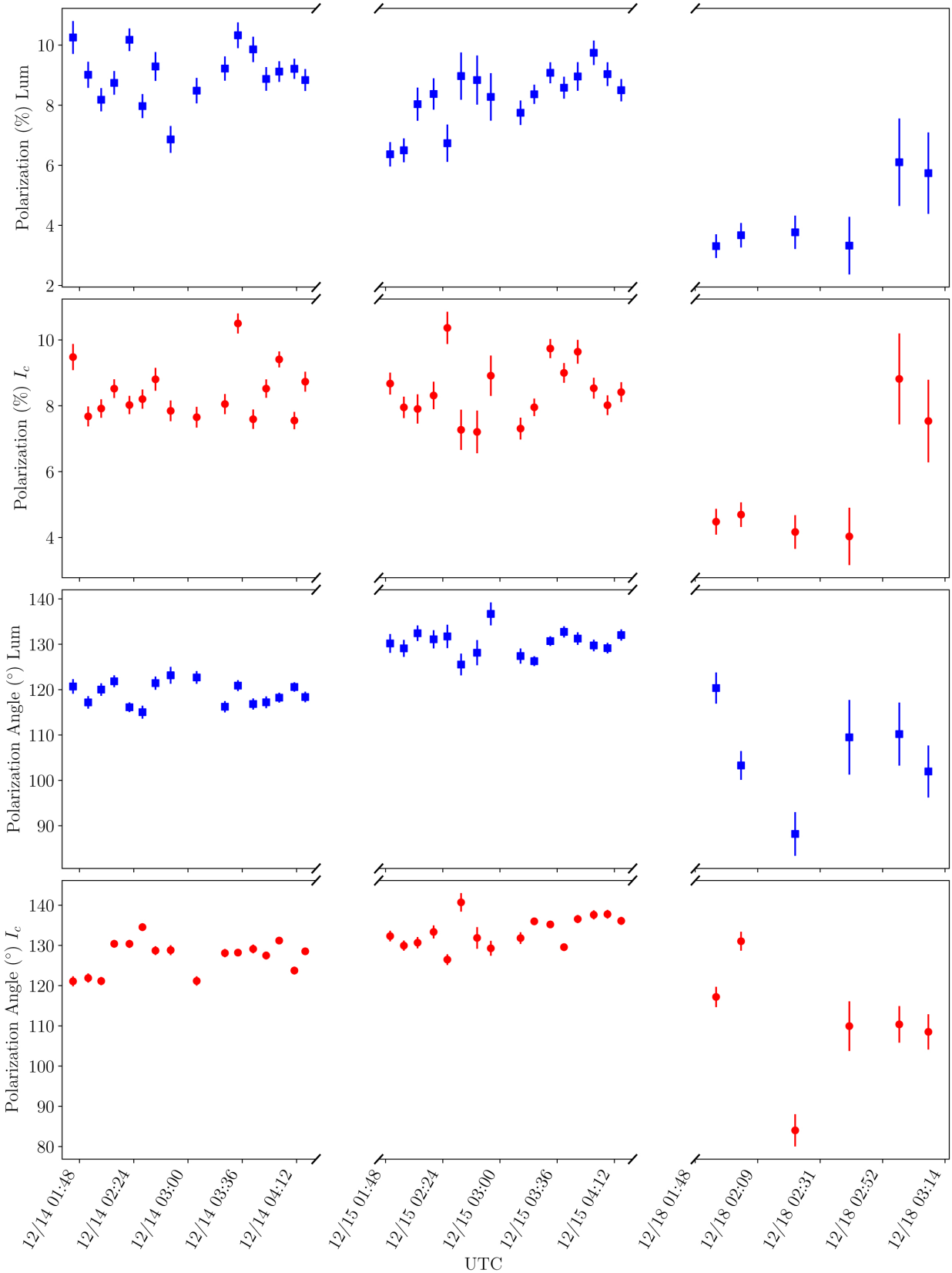

Figure 3.9: Polarization p (in %) and polarization angle ψ (in degrees) for BL Lacertae in the *Lum* and I_c bands. Intensity normalized Stokes parameters $q \equiv Q/I$, and $u \equiv U/I$ for both bands are available in the full machine readable tables.

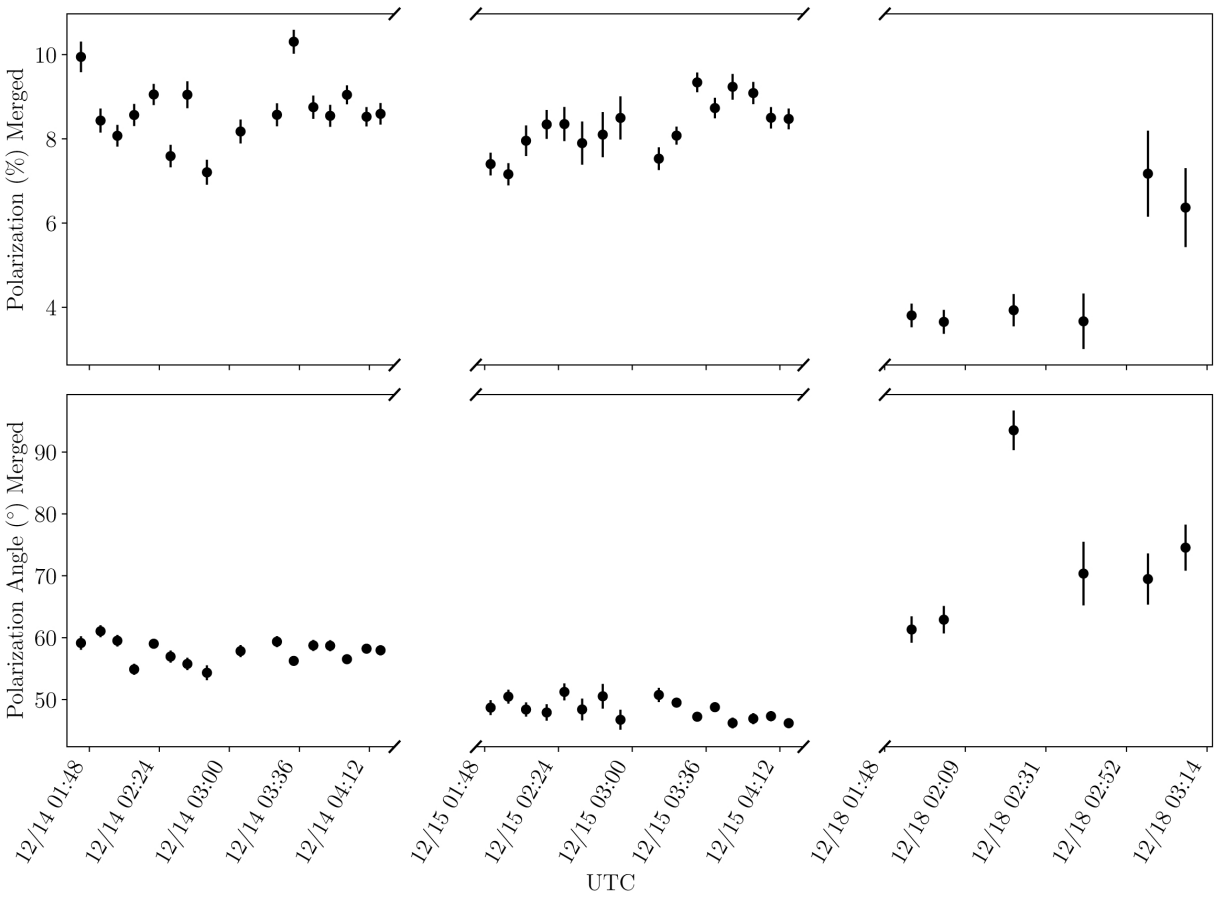

Figure 3.10: BL Lacertae light curves for polarization p (in %), polarization angle ψ (in degrees). Intensity normalized Stokes parameters $q \equiv Q/I$, and $u \equiv U/I$ for the *combined* $Lum + I_c$ band are available in the full machine readable tables.

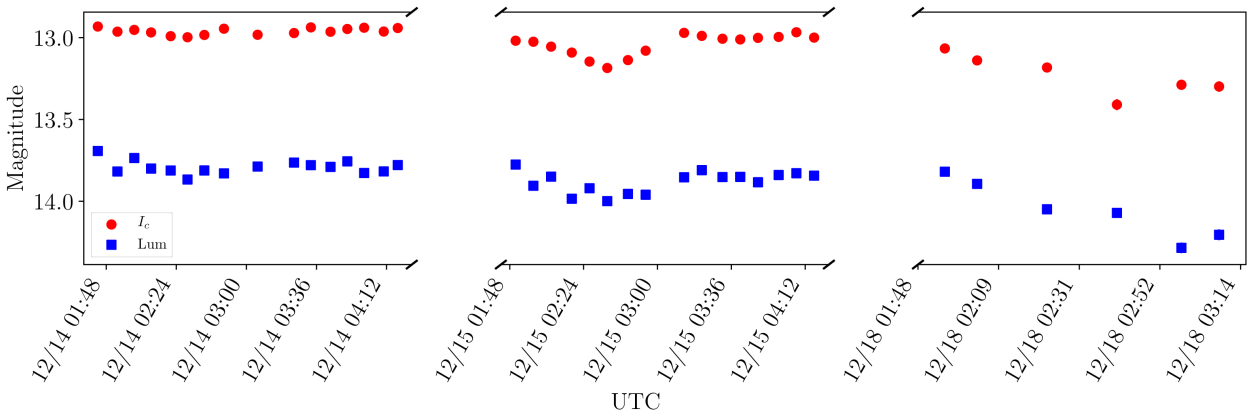

Figure 3.11: I_c and *Lum*-band Photometry for BL Lacertae.

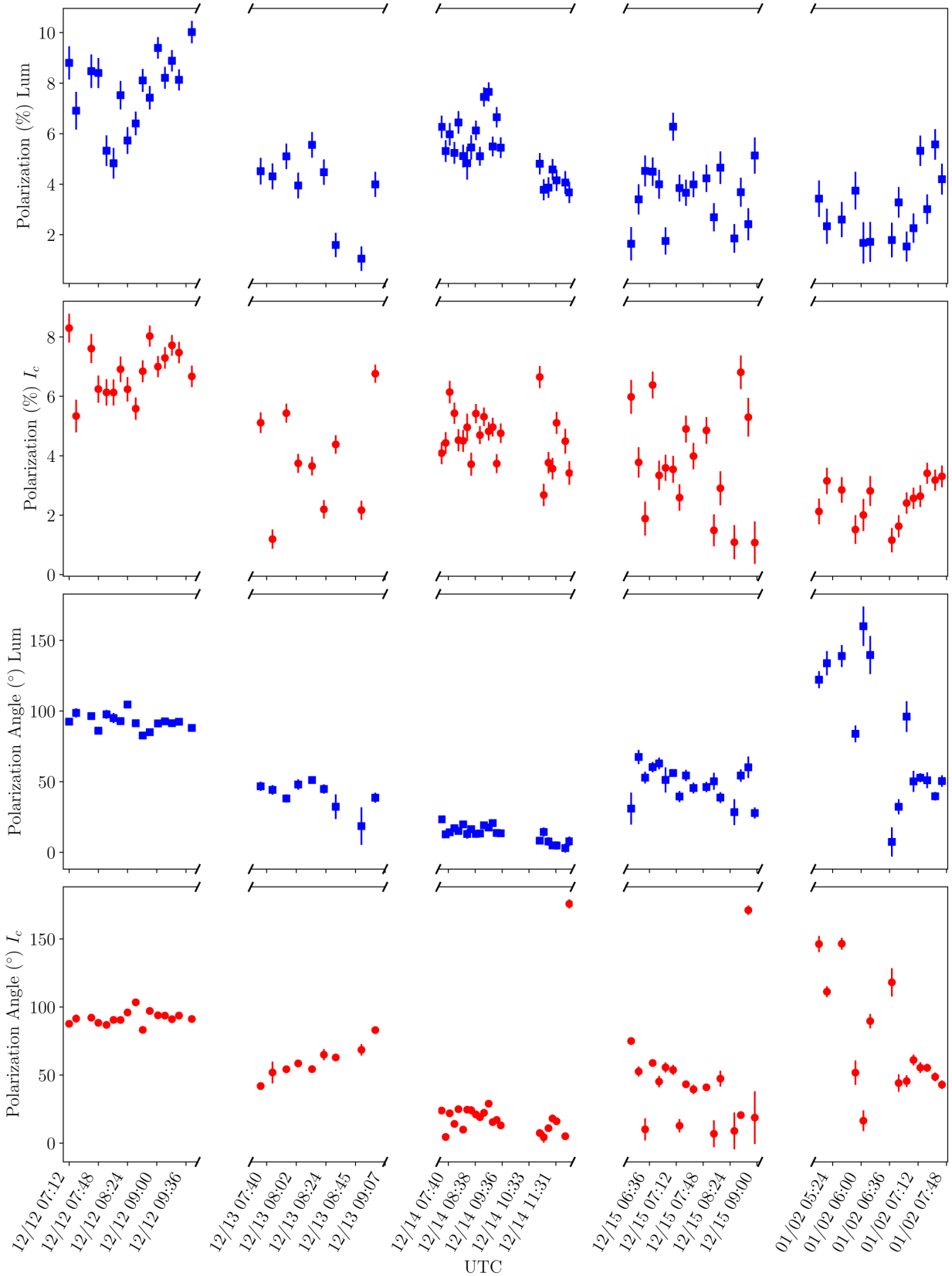

Figure 3.12: Polarization p (in %) and polarization angle ψ (in degrees) for S5 B0716+714 in the *Lum* and I_c bands. Intensity normalized Stokes parameters $q \equiv Q/I$, and $u \equiv U/I$ for both bands are available in the full machine readable tables.

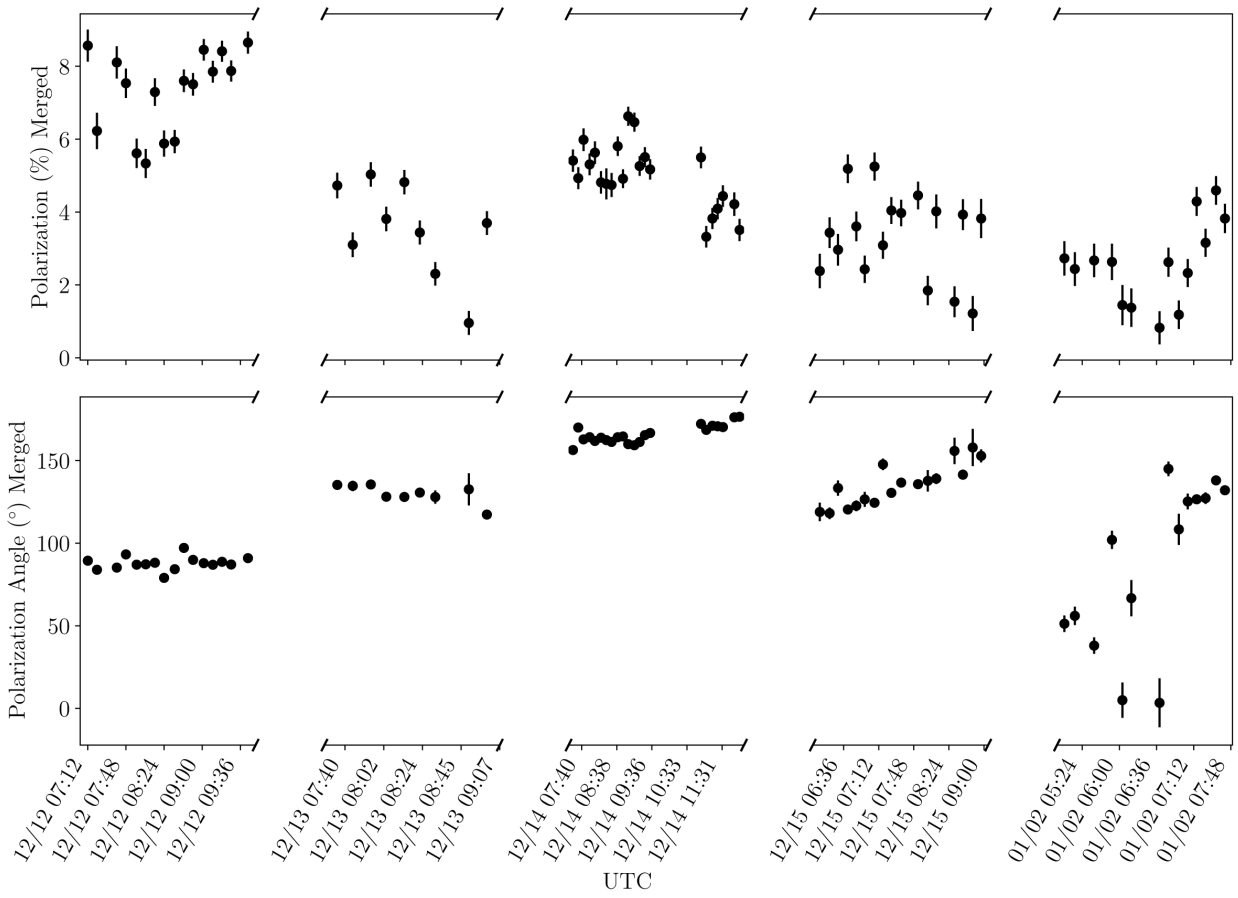

Figure 3.13: S5 B0716+714 light curves for polarization p (in %), polarization angle ψ (in degrees). Intensity normalized Stokes parameters $q \equiv Q/I$, and $u \equiv U/I$ in the *Merged Lum*+I_c band are available in the full machine readable tables.

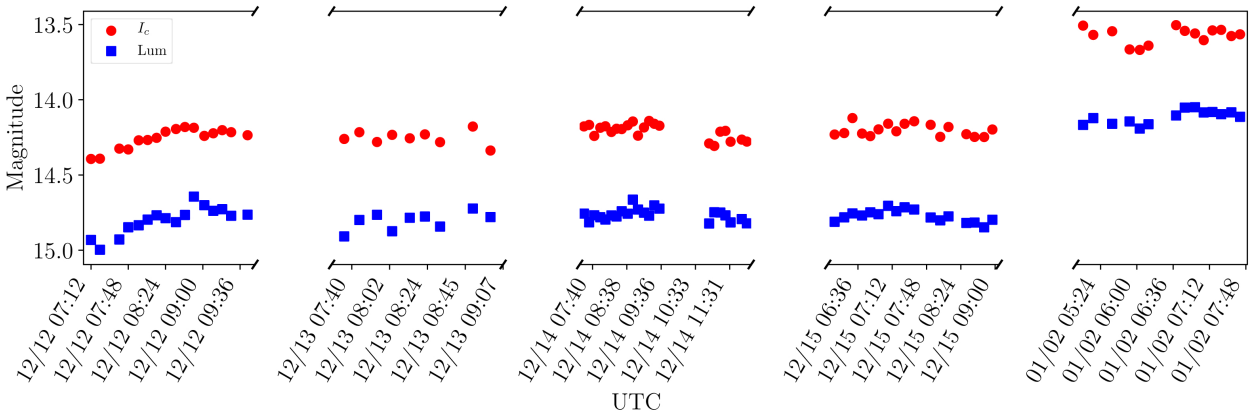

Figure 3.14: I_c and *Lum*-band Photometry for S5 B0716+714.

Table 3.8: Same as Table 3.6 for S5 B0716+714, but for the combined $Lum+I_c$-band. (A portion of this table is shown for guidance. This table is available in its entirety in machine-readable form.)

MJD (days)	p_{L+I} (%)	ψ_{L+I} (deg)	q_{L+I} (%)	u_{L+I} (%)
58099.300	8.6 ± 0.4	89.0 ± 1.0	-8.6 ± 0.4	0.2 ± 0.4
58099.306	6.2 ± 0.5	84.0 ± 2.0	-6.1 ± 0.5	1.3 ± 0.5
58099.319	8.1 ± 0.4	85.0 ± 2.0	-8.0 ± 0.4	1.3 ± 0.4

$$|\bar{c}^{(d)}_{(I)}| \equiv |\sum_{jm} Y_{jm}(\theta,\phi) c^{(d)}_{(I)jm}|, \tag{3.34}$$

$$|\bar{k}^{(d)}_{(V)}| \equiv |\sum_{jm} Y_{jm}(\theta,\phi) k^{(d)}_{(V)jm}|, \tag{3.35}$$

$$|\bar{k}^{(d)}_{(EB)}| \equiv |\sum_{jm} {}_2Y_{jm}(\theta,\phi)(k^{(d)}_{(E)jm} + ik^{(d)}_{(B)jm})|. \tag{3.36}$$

Chapter 4

Measurement of the Cosmic Microwave Background Polarization Lensing Power Spectrum from Two Years of Polarbear Data

We present a measurement of the gravitational lensing deflection power spectrum reconstructed with two seasons cosmic microwave background polarization data from the POLARBEAR experiment. Observations were taken at 150 GHz from 2012 to 2014 which survey three patches of sky totaling 30 square degrees. We test the consistency of the lensing spectrum with a Cold Dark Matter (CDM) cosmology and reject the no-lensing hypothesis at a confidence of 10.9σ including statistical and systematic uncertainties. We observe a value of $A_{\rm L} = 1.33 \pm 0.32$ (statistical) $\pm\, 0.02$ (systematic) $\pm\, 0.07$ (foreground) using all polarization lensing estimators, which corresponds to a 24% accurate measurement of the lensing amplitude. Compared to the analysis of the first year data, we have improved the breadth of both the suite of null tests and the error terms included in the estimation of systematic contamination.

4.1 Introduction

The polarization of the cosmic microwave background (CMB) not only gives us insight into the earliest stages in the evolution of the universe, it also allows us to probe the large scale structure (LSS) formed more recently in cosmological history. CMB polarization can be separated into even parity E-modes and odd parity B-modes, and while the E-modes can be sourced from the same scalar perturbations that dominate CMB temperature anisotropies, B-modes are not generated through this mechanism to first order in perturbations.

Much effort is being devoted to using CMB B-modes for signs of primordial gravitational waves, but another expected source of B-modes is the gravitational lensing of the CMB by LSS [134]. This signature appears in the B-mode power spectrum as a signal peaking at an angular scale $\ell \sim 1000$. By mapping the CMB polarization, we can extract information about the distribution of LSS through reconstruction of the CMB lensing potential.

The CMB lensing potential is a representation of the matter power spectrum, integrated along the line of sight of CMB photons, which can tell us how much a given photon will be gravitationally deflected. For a gravitational potential Ψ we can integrate along the line of sight to calculate the lensing potential ϕ [135],

$$\phi(\boldsymbol{n}) = -2 \int_0^{\chi_*} d\chi \frac{\chi_* - \chi}{\chi_* \chi} \Psi(\chi \boldsymbol{n}, \chi), \tag{4.1}$$

where χ is the comoving distance and χ_* is the comoving distance to the surface of last scattering. The lensing potential is related to the deflection field $\boldsymbol{d} = \boldsymbol{\nabla}\phi$, which tells us how much a photon of the CMB is gravitationally deflected across the sky as it travels from the surface of last scattering to our detector.

We are able to reconstruct the lensing potential by taking advantage of the statistical properties of the CMB. At the surface of last scattering, the CMB is well described as a statistically isotropic Gaussian random field, but gravitational lensing introduces non-Gaussianities that correlate CMB modes of different angular scale. This non-Gaussianity

allows us to reconstruct the underlying lensing potential ϕ by correlating E- and B-modes at varying angular scale [135].

The science of CMB lensing contains a wealth of information about the more recent evolution of the universe, including the formation of LSS and the physics of neutrinos [136]. The polarized CMB in particular is promising as a tracer of LSS because B-modes are not dominated by cosmic variance of the primordial CMB in the same way that the temperature and E-modes are at the present time. Additionally, polarization measurements are also less affected by many of the sources of contamination for the CMB temperature anisotropies, e.g. from the atmosphere or extragalactic foregrounds like the CIB and SZ-effects [137].

The lensing potential has been detected using both CMB temperature and polarization fluctuations by a number of experiments including POLARBEAR – from the first season dataset [138], BICEP2/*Keck Array* [139], ACTPOL [140], Planck [141], and SPTPOL [142].

Additionally, cross correlations between the CMB lensing potential with external tracers has been demonstrated in other POLARBEAR analyses including cross correlation with the cosmic shear measurement of the Subaru Hyper Suprime-Cam [143] and the sub-mm galaxy measurements of the *Herschel*-ATLAS [144] experiments. These cross correlations are valuable in that they can combine information from two independent tracers of LSS while avoiding instrument-specific systematic errors [145].

The search for CMB B-modes from gravitational waves can be improved if the B-mode signal from gravitational lensing is reduced. This "delensing" has been done using several methods. External tracers of the lensing potential have been combined with CMB observations [146, 147] to subtract templates of gravitational lensing and reduce the final B-mode power. Internal delensing has also been achieved in which the lensing potential and B-modes are constructed using the same dataset [148], and in another work we demonstrate internal delensing of the CMB using only polarization data [149]. Both of these delensing methods are useful, but of the two, internal delensing has been forecast to achieve the best performance for sufficiently low noise measurements [150].

In this work we show a reconstruction of the lensing potential power spectrum from observations by the POLARBEAR experiment. We have observed an area of ~ 30 square degrees with one of the lowest levels of arc-minute scale noise yet achieved. The lensing information is dominated by polarization rather than temperature anistotropies. This deep data set has enabled a polarization-only reconstruction of the lensing potential power spectrum, and has served as a useful dataset for additional cross correlation and delensing studies.

4.2 Lensing Power Spectrum Analysis

The polarization-sensitive POLARBEAR experiment is located at the James Ax Observatory in Northern Chile on Cerro Toco. It uses 1,274 transition-edge sensor bolometers to observe the CMB at 150 GHz and has a 2.5 meter primary mirror that produces a beam with a 3.5' full width at half maximum (FWHM).

We observe three sky patches over a time period of two years from 2012 to 2014, each with an extent of approximately $3^\circ \times 3^\circ$. They are centered in right ascension and declination at $(4^{\rm h}40^{\rm m}12^{\rm s}, -45^\circ 00')$, $(11^{\rm h}53^{\rm m}0^{\rm s}, -0^\circ 30')$ and $(23^{\rm h}1^{\rm m}48^{\rm s}, -32^\circ 48')$ which we will refer to with the respective names RA4.5, RA12 and RA23. More details on the receiver and telescope can be found in [151, 152]. One advantage of observing small patches is the ability to obtain deeper observations over a given amount of time. The effective white noise levels after accounting for beam and filter transfer functions are 10 μK-arcmin for RA4.5, 7 μK-arcmin for RA12 and 6 μK-arcmin for RA23.

This analysis builds on previous results from the POLARBEAR collaboration using the same dataset described above. We have shown evidence of B-mode power induced by gravitational lensing [153], which we will refer to as PB17. The CMB maps used in that analysis are also used here.

We also showed evidence of the lensing potential auto-power spectrum itself in a previous work [138] that used only our first season of observations. We will refer to that

paper as PB14. This paper improves upon that work by adding a second year of observations on the same set of three patches, which corresponds to an increase in data volume of 61% over PB14.

We also note that in PB14, we used a separate analysis pipeline from our B-mode analysis to generate simulations and perform null tests. This time our analysis uses the same pipeline to generate lensed and filtered CMB simulations as used in PB17, so that the details of our mapmaking and instrumental systematic estimation are consistent across both publications. This has the advantage that our simulations now accurately model our mapmaking procedure starting at the timestream level and include the anisotropic effects of our timestream filters in the lensing reconstruction step. Additionally we have included a set of data split null tests not present in our first season lensing analysis, these are described in more detail in Section 4.3.1.

In our data analysis pipeline, we start with Q and U CMB maps to obtain weighted E- and B-modes using the data model

$$d_i = P_{ik} s_k + n_i, \tag{4.2}$$

where d_i contains the pixelized real space Q and U maps, n_i are the pixelized map domain noise contributions, and s_k are the E- and B-mode fields. P_{ik} is the matrix operator that encodes effects from the beam and timestream filtering, and transforms from Fourier space to real space. The index i includes Q/U and pixel indices $i = (M, p)$, and the index k includes E/B and mode indices $k = (X, \boldsymbol{\ell})$.

We obtain inverse-variance Wiener-filtered CMB E- and B-modes, $\overline{X}(\boldsymbol{\ell})$, from the observed Q and U maps, d, using the matrix equation

$$\overline{X} = S^{-1} \left[S^{-1} + P^\dagger N^{-1} P \right]^{-1} P^\dagger N^{-1} d, \tag{4.3}$$

where $S_{kk'} = \delta_{XX'} \delta_{\boldsymbol{\ell}\boldsymbol{\ell}'} C_\ell^{XX}$ and $N_{ii'} = \delta_{MM'} \delta_{pp'} N_p^M$. C_ℓ^{XX} are the fiducial CMB power spectra

for $X \in \{E, B\}$ and N_p^M is the noise map where p labels a given pixel in the map and $M \in \{Q, U\}$. Our noise weighting also includes a cutoff for pixels with noise levels above 55 μK-arcmin and point source masking for sources above 25 mJy in intensity. The CMB power spectra used for this Wiener filter are generated using the freely available software package CAMB [1], and use the Planck 2015 best fit cosmological parameters [154] [2], which is the same parameter set used in PB17.

From the inverse variance weighted modes $\overline{X}(\boldsymbol{\ell})$ we then reconstruct the lensing potential using the quadratic estimator

$$\hat{\phi}^{XY}(\boldsymbol{L}) = A(\boldsymbol{L}) \int d^2\boldsymbol{\ell}\ \overline{X}(\boldsymbol{\ell})\ \overline{Y}^*(\boldsymbol{\ell} - \boldsymbol{L})\ F_{XY}(\boldsymbol{\ell}, \boldsymbol{\ell} - \boldsymbol{L}), \tag{4.4}$$

where the normalization is defined by

$$A^{-1}(\boldsymbol{L}) = \int d^2\boldsymbol{\ell}\ f_{XY}(\boldsymbol{\ell}, \boldsymbol{\ell} - \boldsymbol{L}) F_{XY}(\boldsymbol{\ell}, \boldsymbol{\ell} - \boldsymbol{L}), \tag{4.5}$$

and the weights $f_{XY}(\boldsymbol{\ell}, \boldsymbol{\ell} - \boldsymbol{L})$ and $F_{XY}(\boldsymbol{\ell}, \boldsymbol{\ell} - \boldsymbol{L})$ are described in detail in [155].

In addition to our data we also use a set of 500 Monte Carlo (MC) simulations in our analysis to estimate the lensing mean field, noise bias, transfer function and covariance matrix. We generate realizations of lensed CMB signal that are mock observed using the same pointing, noise level and scan strategy as our real observations. These timestreams are then run through our mapmaking pipeline and the resulting Q and U maps are used as inputs to our lensing pipeline as described in the above equations.

The process of going from quadratic estimates of the lensing potential $\hat{\phi}^{XY}(\boldsymbol{L})$ to power spectra follows the method we used in PB14. First we estimate the mean field from our set of MC simulations and subtract that from $\hat{\phi}^{XY}(\boldsymbol{L})$. Next we correlate two reconstructed lensing maps $\hat{\phi}^{UV}(\boldsymbol{L})$ and $\hat{\phi}^{XY}(\boldsymbol{L})$ to construct the pseudospectra $\hat{C}_L^{UVXY}$, where the indices

[1] camb.info

[2] in the `base_plikHM_TT_lowTEB_lensing` configuration

UV, XY indicate the type of estimator (EE or EB). We follow the [156] and [157] to estimate the realization-dependent noise bias $N_L^{(0),UVXY}$ using lensing reconstructions of our data and MC simulations. Once bias subtracted spectra from simulations are constructed, we then estimate the transfer function by taking the ratio between the mean of these reconstructed lensing power spectra and the input theory power spectrum used to generate them. And finally, this transfer function is used to correct the lensing potential power spectrum estimate of our data giving us our final spectra as defined by the equation,

$$C_L^{UVXY} = \left(\hat{C}_L^{UVXY} - N_L^{(0),UVXY}\right) \Big/ T_L. \tag{4.6}$$

Here, T_L is the transfer function that corrects for the effects of filtering and weighting in our pipeline and C_L is the lensing potential power spectrum. The lensing estimators are labeled here by $UV, XY \in \{EE, EB\}$. Additionally, while we only used C_L^{EEEB} and C_L^{EBEB} in PB14, we include the power spectrum estimator C_L^{EEEE} in this analysis.

To estimate the amplitude of lensing, we use 500 MC simulations to construct the covariance between our three C_L^{UVXY} estimators. If we label the estimator $\alpha = UVXY \in \{EEEE, EEEB, EBEB\}$, and the covariance matrix $\mathcal{C}_{L\alpha,L'\alpha'}$ represents the covariance between the bandpower C_L^{α} and $C_{L'}^{\alpha'}$, then the lensing amplitude is

$$A_{\rm L} = \frac{\sum_{L\alpha L'\alpha'} C_L^{\alpha(\rm th)} \mathcal{C}^{-1}_{L\alpha,L'\alpha'} C_{L'}^{\alpha'}}{\sum_{L\alpha L'\alpha'} C_L^{\alpha(\rm th)} \mathcal{C}^{-1}_{L\alpha,L'\alpha'} C_{L'}^{\alpha'(\rm th)}}, \tag{4.7}$$

and the inverse variance on the amplitude is given by

$$(\sigma_A)^{-2} = \sum_{L\alpha L'\alpha'} C_L^{\alpha(\rm th)} \mathcal{C}^{-1}_{L\alpha,L'\alpha'} C_{L'}^{\alpha'(\rm th)}, \tag{4.8}$$

where the (th) subscript denotes the theory power spectrum.

Finally we have also found that our observations are polarization dominated. While we do not include temperature in the results presented here, we have compared $N^{(0)}$ bias

curves from temperature-only information (the TT estimator) and from polarization-only information (the EE and EB estimators) and found lower noise in polarization.

4.3 Null Tests

We perform a blind analysis and therefore need a way to guard against unknown systematics and validate our error-bar estimation, which we address through a set of null tests. We only examined our final power spectra after all of our null tests satisfy passing criteria that demonstrate our analysis is performing as expected.

All of the simulations used in the following null tests are generated at the timestream level. They use the same pointing reconstruction used for real observations to mock simulate CMB signal sky observations, and include noise at the timestream level based on a white noise model consistent with the real observations of the second season in PB17. The resulting simulated timestreams are run through the same mapmaking and lensing reconstruction pipelines as is used for the real data.

4.3.1 Data Split Null Tests

We perform one suite of null tests constructed from splits in our data selection. We choose twelve splits to probe potential systematic errors that are not captured by the lensing analysis pipeline. The splits are listed in Table 4.1. These are the same data splits used in PB17, where more detailed description of the twelve data splits can be found.

For each of these twelve data splits we construct two sets of lensing estimates, $\hat{\phi}^{U_1V_1}(\boldsymbol{L})$ and $\hat{\phi}^{X_1Y_1}(\boldsymbol{L})$ for the first set of the split dataset and $\hat{\phi}^{U_2V_2}(\boldsymbol{L})$ and $\hat{\phi}^{X_2Y_2}(\boldsymbol{L})$ for the second set of the split dataset. We then construct the auto spectra of each of the two sets and the cross spectra between the two sets, including a noise bias subtraction for each of these

Table 4.1: Data split null test types.

First vs. second seasons of data collection
Close to sun vs. far from sun
Day vs. night
First half vs. second half by data volume
Rising vs. setting
High elevation vs. low elevation
High vs. low detector gain
Good vs. bad weather
Q vs. U pixels
Left vs. right side of the focal plane
Left vs. right scan direction
Close to moon vs. far from moon

The twelve ways that we split the dataset for null tests that probe potential unmodeled systematic errors.

component spectra. Finally we use these to construct the null spectrum

$$C_L^{\rm null} = C_L^{U_1V_1X_1Y_1} + C_L^{U_2V_2X_2Y_2} - C_L^{U_1V_1X_2Y_2} - C_L^{U_2V_2X_1Y_1}. \tag{4.9}$$

We evaluate this set of 108 null spectra (from 12 splits, 3 power spectrum estimators, and 3 sky patches) similarly to the procedure used in PB17.

Using nine equally spaced bins b in the multipole range $100 < L < 1900$ and an estimate of the standard deviation σ_b from MC simulations we construct the quantity $\chi_{\rm null}(b)$ $\equiv C_b^{\rm null}/\sigma_b$. For each patch, we then calculate the probability to exceed (PTE) value for five quantities: the average value of $\chi_{\rm null}(b)$, the worst value of $\chi^2_{\rm null}(b)$, the worst value of $\chi^2_{\rm null}$ by spectrum (summed over all bins), the worst value of $\chi^2_{\rm null}$ by test, and finally the total value of $\chi^2_{\rm null}$ for each patch. The simulated data which are generated from the simulated timestreams are split the same way as the observed data. The error bars σ_b are then estimated from an ensemble of 500 simulated data splits. The results from these null tests are summarized in Table 4.2.

Our unblinding criteria involves calculating a total PTE (labeled as "All stats" in

Table 4.2) for the five tests just described. We take the worst of the five χ^2 PTEs from the data, and then we compare to the worst PTE from a distribution of simulations. The "All stats" PTE is the fraction of the simulations that exceed the data and we require that this total PTE is above 5% before ever calculating the final power spectra from data. The results from these null tests are summarized in the rightmost column of Table 4.2.

For the PTEs involving χ^2 statistics we calculate $\chi^2_{\rm data}$ for our data and $\chi^2_{{\rm sim},i}$ for each of our 500 MC simulations. Our PTE value is then equal to the fraction of the simulations such that $\chi^2_{{\rm sim},i} > \chi^2_{\rm data}$. For the average $\chi_{\rm null}(b)$ statistic we evaluate the PTE slightly differently than the rest by performing a two sided test. We calculate the average $\chi_{\rm data}$ for the data and the average $\chi_{{\rm sim},i}$ for each simulation and the corresponding PTE is equal to the fraction of the simulations such that $\chi_{{\rm sim},i} > \chi_{\rm data}$.

Table 4.2: PTEs resulting from the data split null tests.

Patch	Average of $\chi_{\rm null}(b)$	Extreme of $\chi^2_{\rm null}(b)$	Extreme of $\chi^2_{\rm null}$ by spectrum	Extreme of $\chi^2_{\rm null}$ by test	Total $\chi^2_{\rm null}$	All stats
RA4.5	47.8%	58.8%	56.2%	92.6%	99.0%	75.0%
RA12	47.2%	43.8%	85.2%	76.8%	50.0%	73.0%
RA23	35.8%	78.2%	81.4%	69.6%	47.4%	61.2%

PTEs resulting from the data split null tests. The furthest right column capturing the results of all five tests are above 5% indicating that our dataset passes the null test criteria. We also checked to see if the distribution of all PTEs agree with a uniform distribution via the Kolmogorov-Smirnov test and found that for all of our patches the null PTEs are indeed consistent with a uniform distribution as expected. One notable feature of the table is a preponderance of high PTE values which is caused by our treatment of the noise bias subtraction. We elaborate on this in the appendix but otherwise we find no evidence for systematic biases in the data.

4.3.2 Curl and Cross-Patch Null Tests

Additionally we conduct a set of lensing specific null tests using the full dataset. First we generate curl reconstructions of the lensing deflection field $\boldsymbol{\nabla} \times \boldsymbol{d}(\hat{\boldsymbol{n}})$, which we expect to be vanishingly small and serve as a check on unmodeled systematics [158].

We also generate cross power spectra between lensing reconstructions from two different

observational patches. These independent measurements should lack any common signal, so any significant deviation from a null spectrum would indicate a misestimation of our error bars or a spurious correlation introduced by our analysis pipeline.

Both of these tests were also performed in PB14. Our passing criteria for these sets of tests are similar to our criteria for the data split null tests. We calculate the worst χ^2 PTEs corresponding to the average of $\chi_{\rm null}(b)$, extreme of $\chi^2_{\rm null}(b)$, extreme of $\chi^2_{\rm null}$ by spectrum, and a total $\chi^2_{\rm null}$, in addition to a combined PTE combining all four of those statistics. We consider the dataset to have passed these tests if the final PTE accounting for all statistics is greater than 5%. The results from this set of null tests are summarized in Table 4.3, in particular showing that the PTEs for all statistics are 53.0% for the curl tests and 60.2% for the cross-patch tests. We also note that these null tests do not require a noise bias subtraction and thus are not affected by the noise bias calculation subtlety described in the Appendix.

Table 4.3: PTEs resulting from the curl and cross-patch null tests.

Test	Average of $\chi_{\rm null}(b)$	Extreme of $\chi^2_{\rm null}(b)$	Extreme of $\chi^2_{\rm null}$ by spectrum	Total $\chi^2_{\rm null}$	All stats
curl	48.6%	23.8%	58.6%	64.8%	53.0%
cross	95.4%	16.0%	27.4%	16.2%	60.2%

PTEs resulting from the curl and cross-patch null tests. Again we see that all of the individual worst $\chi^2_{\rm null}$ criteria and the PTE combining all stats in the rightmost column are all above the required null test threshold. Like the data split tests, we also tested the distribution of PTEs and found they are consistent with a uniform distribution via the Kolmogorov-Smirnov test.

4.4 Contamination

We use a difference spectrum framework to evaluate the effect of instrumental systematic and foreground contamination to the lensing spectrum by looking at the effect on $A_{\rm L}$.

Using a set of MC simulations, we calculate two lensing power spectra for each CMB realization. The first spectrum is created with the fiducial pipeline while the second spectrum

is created by adding a realization of the contamination at map level to our Q and U maps. The difference between these two is used as our estimate of contamination,

$$\Delta C_L^c = C_L^c - C_L, \tag{4.10}$$

where C_L^c denotes the lensing power spectrum calculated including contamination while C_L is the spectrum calculated without contamination.

4.4.1 Instrumental Systematics

In PB17 we used simulations of systematic effects to estimate their contributions to the C_ℓ^{BB} power spectrum. This systematics pipeline was incorporated into our main analysis pipeline and generated contamination at the timestream level that modeled a number of different instrumental systematic effects. We use that same systematic simulation pipeline here to estimate contributions to the lensing power spectrum.

For each instrumental systematic effect we use 100 MC estimates of ΔC_L^c. The mean value of these spectra and their covariance are then used to calculate an effective lensing amplitude due to systematic contamination, $A_{\rm L}^c \pm \sigma_A^c$. To evaluate any bias introduced to $A_{\rm L}$ by a given systematic effect, we calculate an upper limit $\Delta A_{\rm L}^c$ on the lensing amplitude given by

$$\Delta A_{\rm L}^c = |A_{\rm L}^c| + \frac{\sigma_A^c}{\sqrt{100}}. \tag{4.11}$$

In addition to limits on systematic bias to the lensing power spectrum, we also account for the extra variance introduced by systematic effects through their effects on σ_A. We add in quadrature all the values of σ_A^c in our final estimation of $A_{\rm L}$.

A summary of the contributions σ_A^c and $\Delta A_{\rm L}^c$ from each systematic effect is shown in Table 4.4, in particular showing that the total contribution to σ_A^c is 0.02 and our upper limit on systematic bias from all modeled effects is 0.006.

Table 4.4: Contributions to $A_{\rm L}$ from instrumental systematic effects.

Effect [$\times 10^{-3}$]	$A_{\rm L}^c$	σ_A^c	$\Delta A_{\rm L}^c$
Crosstalk	-0.28	1.9	0.47
Pointing	3.60	21.2	5.72
Beam Ellipticity	0.54	1.5	0.69
Beam Size	0.16	1.8	0.34
Gain Drift	0.14	2.7	0.41
Relative Gain	-0.67	4.9	1.16
Total		22.1	5.92

All values have been multiplied by a factor of 10^3 for display in this table. The resulting total contribution to our uncertainty on the lensing amplitude is $\sigma_A^c = 0.022$, and our upper limit on the total systematic bias is $\Delta A_{\rm L}^c = 0.006$.

4.4.2 Foregrounds

We use the Planck 2015 frequency maps to estimate the impact that foregrounds have on our reconstruction of gravitational lensing [159, 160]. In particular, we use the Planck 30 GHz and 353 GHz all sky intensity maps as tracers of synchrotron and dust foreground power, respectively. Our observational patches were chosen, in part, because they have very low foreground power. Thus, the Planck polarization maps are dominated by noise in the regions of the sky that we observed. Therefore, to estimate a conservative upper limit on foreground power, we use a polarization fraction of $p = 20\%$ and constant polarization angle in combination with Planck intensity maps to generate maps of polarized foregrounds in our three patches.

The amplitudes of these Planck maps are scaled to 150 GHz assuming a modified blackbody spectral dependence for thermal dust and a power law for synchrotron [161, 162], and then simulated timestreams are produced and run through our analysis pipeline in order to include the scan strategy, time stream processing, filtering, and other effects that are incorporated in our real observations.

Finally, contributions to the lensing power spectrum ΔC_L^c for our dust and synchrotron estimates are constructed using the same method as the instrumental systematics, and contributions to the bias and uncertainty on $A_{\rm L}$ are calculated and listed in Table 4.5.

Table 4.5: Contributions to $A_{\rm L}$ from foreground contamination.

Effect $[\times 10^{-3}]$	$A_{\rm L}^c$	σ_A^c	$\Delta A_{\rm L}^c$
Dust	3.16	65.1	9.67
Synchrotron	-0.42	7.6	1.18
Total		65.5	9.74

All values have been multiplied by a factor of 10^3 for display in this table. The resulting total contribution to our uncertainty on the lensing amplitude is $\sigma_A^c = 0.066$, and our upper limit on the total systematic bias is $\Delta A_{\rm L}^c = 0.0097$.

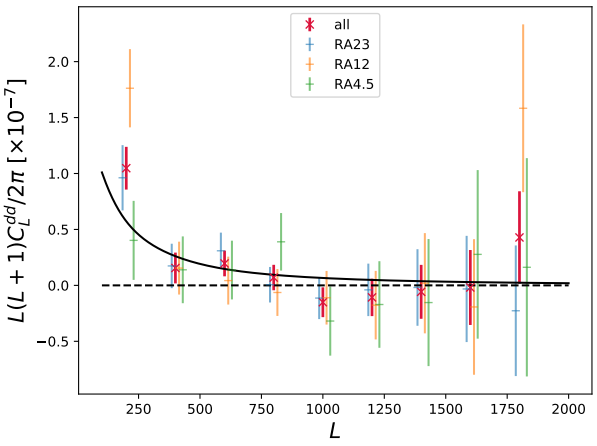

Figure 4.1: Minimum variance lensing deflection power spectrum, with variance taken from the diagonal elements of the covariance matrix.

The black solid curve represents the power spectrum for $A_{\rm L}$= 1. Red data points are the minimum variance POLARBEAR power spectrum from a combination of our three observational patches and three power spectrum estimators, C_L^{EEEE}, C_L^{EEEB} and C_L^{EBEB}. The blue, orange, and green points represent the power spectra for each of the three patches (RA23, RA12, and RA4.5 respectively) and are offset in L in the above plot for clarity.

4.5 Results

We present the minimum variance power spectrum in Figure 4.1, which combines power spectra from our three observational patches and the three polarized estimators. The bandpowers and error bars are listed in Table 4.6. The statistical uncertainty on our measurement of $A_{\rm L}$ is calculated from the standard deviation of the distribution of simulated $A_{\rm L}$ from 500 signal-plus-noise MC simulations. Including uncertainty from instrumental systematics and foreground contamination, our measurement of the lensing amplitude is 1.33 ± 0.32 (statistical) ± 0.02 (systematic) ± 0.07 (foreground), corresponding to a significance

of 4.1σ.

Table 4.6: Minimum variance spectrum bandpowers.

Central L	$D_L[\times 10^{-8}]$
200	10.47 ± 1.91
400	1.55 ± 1.38
600	1.96 ± 1.15
800	0.70 ± 1.14
1000	-1.51 ± 1.33
1200	-1.08 ± 1.67
1400	-0.58 ± 2.41
1600	-0.19 ± 3.35
1800	4.28 ± 4.13

The minimum variance power spectrum $D_L = L(L+1)C_L/2\pi$ with 1σ error bars, multiplied by a factor of 10^8 in this table for display purposes.

Additionally, we examine the no-lensing hypothesis using a set of 500 MC simulations that do not include gravitational lensing. The distribution of unlensed simulations has a width of $\sigma_A = 0.12$, corresponding to a forecasted significance of 8.3σ. As was the case in PB14, the suboptimal weighting in the lensing estimator due to the assumption of no-lensing has the effect of shifting the value of the lensing amplitude. The power spectrum calculated under the no-lensing assumption on our data has an estimated amplitude of $A_{\rm L} = 1.52$. Including uncertainty from systematics and foregrounds and our observed value of $A_{\rm L}$, we reject the no-lensing hypothesis at a significance of 10.9σ, which is a considerable improvement upon the 4.2σ rejection from our earlier work in PB14. Distributions of the $A_{\rm L}$ calculated from simulations in the lensed and unlensed cases are shown in Figure 4.2.

We evaluate the consistency of our three patches by comparing the patchwise minimum variance power spectra $C_L^p, p \in \{\mathrm{RA23}, \mathrm{RA12}, \mathrm{RA4.5}\}$ between pairs of patches using PTEs of the quantities $C_L^p - C_L^{p'}$. Additionally, we note that the first bin in the power spectrum for RA12 is considerably higher than the other two so we also evaluate PTEs specifically comparing the values in the first bin of each of our three patches. The results of these tests are summarized in Table 4.7 which confirm that the three patches are consistent with each

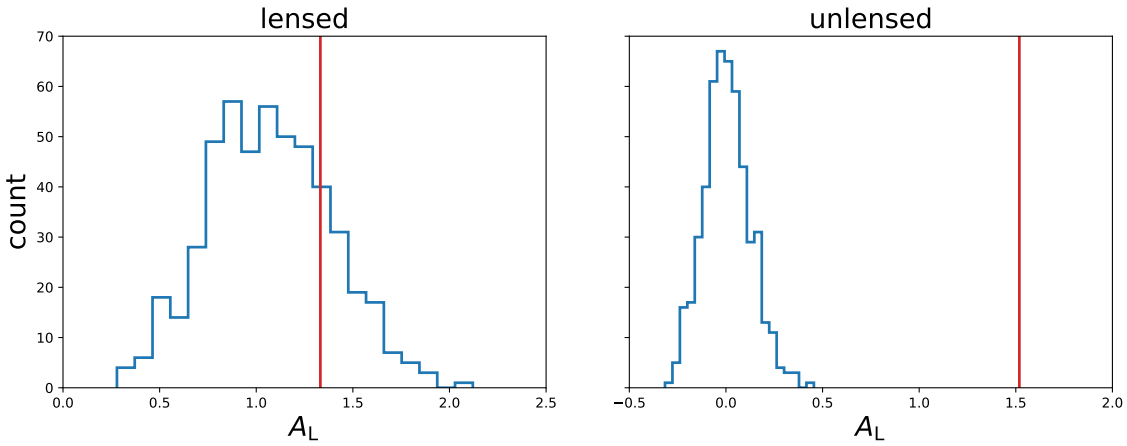

Figure 4.2: Distribution of A_L from 500 MC simulations compared to the observed amplitude.

The right plot assumes no lensing while the left plot uses lensed CMB simulations. In both cases, the blue histogram represents the distribution of A_L and the red vertical line marks our observed value. As in PB14, different weighting in the lensing estimator under the lensing/no-lensing cases results in different values of A_L.

other.

Table 4.7: PTEs comparing pairs of observational patches.

	full spectra	first bins only
RA23 vs. RA12	24.8%	35.6%
RA12 vs. RA4.5	49.6%	8.0%
RA4.5 vs. RA23	89.2%	56.2%

We evaluate the consistency of our three patches with PTE values for the quantity $C_L^p - C_L^{p'}$.

This modest excess of power in RA12 is also seen in cross correlation analyses with *Herschel*-ATLAS and Subaru Hyper Suprime-Cam [143, 144], both of which use independent analysis pipelines. In particular when looking at the *Herschel*-ATLAS galaxy auto-power spectra of RA23 and RA12 patches, we see that RA12 has a modest excess in power in the lowest multipole bin similar to what we see in the present analysis. This gives further support to the interpretation that the larger power in RA12 at low multipoles is due to cosmic variance.

We test the consistency of this result with the ΛCDM cosmology using cosmological

parameters from [82]. We evaluate PTE values for the χ^2 statistic

$$\chi^2 = \sum_{L\alpha L'\alpha'} \left(C_L^{\alpha} - A_{\rm L} C_L^{\alpha({\rm th})}\right) \mathcal{C}^{-1}_{L\alpha,L'\alpha'} \left(C_{L'}^{\alpha'} - A_{\rm L} C_{L'}^{\alpha'({\rm th})}\right), \tag{4.12}$$

which is summed over power spectra for all estimators and patches, nine in total. Relative to our best fit value of $A_{\rm L} = 1.33$ that we achieve from the POLARBEAR dataset, we find a PTE of 58.8%, and relative to the value of $A_{\rm L} = 1$ expected from ΛCDM we find a PTE of 5.0%, which indicate that our results agree with our current understanding of the cosmological standard model.

We can also consider our result in light of recent results for $A_{\rm L}$ from Planck. The lensing smoothing effect on the Planck temperature and polarization CMB power spectra give a value of $A_{\rm L} = 1.180 \pm 0.065$ [163] which differs from $A_{\rm L} = 1$ by 2.8σ, while the measurement from Planck lensing reconstruction [141] is consistent with ΛCDM with the value $A_{\rm L} = 1.011 \pm 0.028$. While our own value is also consistent with ΛCDM, we note that our estimate of $A_{\rm L}$ is consistent with both of these Planck estimates of the lensing amplitude.

4.6 Conclusion

We have presented a measurement of gravitational lensing of the polarized CMB. This work was performed using a blind analysis framework that subjected our dataset to a suite of null tests to validate error-bars and show that our data selection and analysis pipeline are not contaminated by unknown systematic errors. We include the impact of known foreground and instrumental systematic errors in our final estimations, and we reject the no-lensing hypothesis at a significance of 10.9σ. The lensing power spectrum derived using a minimum-variance estimator from the second season data is measured as $A_{\rm L} = 1.33 \pm 0.32$ (statistical) ± 0.02 (systematic) ± 0.07 (foreground), which is a 4.1σ measurement and is consistent with the current ΛCDM cosmology.

The lensing information in the POLARBEAR data presented here is derived from

polarization information. Polarization measurements of gravitational lensing will become increasingly more relevant as more experiments are dominated by polarization rather than temperature information. This work joins our other cross correlation [144, 143] and delensing [149] analyses in exploring signals of gravitational lensing present in CMB polarization.

4.7 Acknowledgements

The POLARBEAR project is funded by the National Science Foundation under Grants No. AST-0618398 and No. AST-1212230. The James Ax Observatory operates in the Parque Astronómico Atacama in Northern Chile under the auspices of the Comisión Nacional de Investigación Cient´ifica y Tecnológica de Chile (CONICYT). This research used resources of the Central Computing System, owned and operated by the Computing Research Center at KEK, the HPCI system (Project ID:hp150132), the National Energy Research Scientific Computing Center, a DOE Office of Science User Facility supported by the Office of Science of the U.S. Department of Energy under Contract No. DE-AC02-05CH11231, and the Open Science Grid, which is supported by the National Science Foundation and the U.S. Department of Energy's Office of Science. In Japan, this work was supported by MEXT KAKENHI Grant Numbers JP15H05891, 21111002, JSPS KAKENHI Grant Numbers JP26220709, JP24111715, JP26800125, and JP18H05539. This work was supported by World Premier International Research Center Initiative (WPI), MEXT, Japan. This work was supported by JSPS Core-to-Core program. In Italy, this work was supported by the RADIOFOREGROUNDS grant of the European Union's Horizon 2020 research and innovation programme (COMPET-05-2015, grant agreement number 687312) as well as by the INDARK INFN Initiative and the COSMOS network of the Italian Space Agency (cosmosnet.it). The McGill authors acknowledge funding from the Natural Sciences and Engineering Research Council of Canada and the Canadian Institute for Advanced Research. Support from the Ax Center for Experimental Cosmology at UC San Diego is gratefully acknowledged. The Melbourne group acknowledges support

from the University of Melbourne and an Australian Research Council's Future Fellowship (FT150100074). Work at LBNL is supported in part by the U.S. Department of Energy, Office of Science, Office of High Energy Physics, under contract No. DE-AC02-05CH11231. This work was supported by the Moore Foundation, the Templeton Foundation and the Simons Foundation.

GF acknowledges the support of the European Research Council under the European Union's Seventh Framework Programme (FP/2007-2013) / ERC Grant Agreement No. [616170] and of the UK STFC grant ST/P000525/1. MA acknowledges support from CONICYT UC Berkeley-Chile Seed Grant (CLAS fund) Number 77047, Fondecyt project 1130777 and 1171811, DFI postgraduate scholarship program and DFI Postgraduate Competitive Fund for Support in the Attendance to Scientific Events. MH acknowledges the support from the JSPS KAKENHI Grant Numbers JP26220709 and JP15H05891. JC acknowledges support from the European Research Council under the European Union's Seventh Framework Programme (FP/2007-2013) / ERC Grant Agreement No. [616170] YC acknowledges the support from the JSPS KAKENHI Grant Number 18K13558 and 18H04347. AK acknowledges the support by JSPS Leading Initiative for Excellent Young Researchers (LEADER) and by the JSPS KAKENHI Grant Number JP16K21744. BDS acknowledges funding from the European Research Council (ERC) under the European Union's Horizon 2020 research and innovation programme and support from an STFC Ernest Rutherford Fellowship. OT acknowledges the support from the JSPS KAKENHI Grant Number JP26105519.

Chapter 4, in full, is a reprint of material as it appears in M. Aguilar Faúndez, K. Arnold, C. Baccigalupi, D. Barron, D. Beck, S. Beckman, F. Bianchini, J. Carron, K. Cheung, Y. Chinone, H. El Bouhargani, T. Elleflot, J. Errard, G. Fabbian, C. Feng, T. Fujino, N. Goeckner-Wald, T. Hamada, M. Hasegawa, M. Hazumi, C.A. Hill, H. Hirose, O. Jeong, N. Katayama, B. Keating, S. Kikuchi, A. Kusaka, A.T. Lee, D. Leon, E. Linder, L.N. Lowry, F. Matsuda, T. Matsumura, Y. Minami, M. Navaroli, H. Nishino, A.T.P. Pham, D. Poletti, G. Puglisi, C.L. Reichardt, Y. Segawa, B.D. Sherwin, M. Silva-Feaver, P. Siritanasak, R. Stompor,

A. Suzuki, O. Tajima, S. Takatori, D. Tanabe, G.P. Teply, and C. Tsai, "Measurement of the Cosmic Microwave Background Polarization Lensing Power Spectrum from Two Years of POLARBEAR Data" ApJ, 893, 85, 2020 (arXiv:1911.10980) [3]. The dissertation author was the primary author of this work.

Chapter 5

Constraints on Scalar and Tensor Spectra from $N_{\rm eff}$

At the linear level, the gravitational wave (GW) spectrum predicted by inflation, and many of its alternatives, can have arbitrarily small amplitude and consequently an unconstrained tilt. However, at second order, tensor fluctuations are sourced by scalar fluctuations that have been measured in the cosmic microwave background (CMB). These second order fluctuations generically produce a minimum amount of tensor perturbations corresponding to a tensor-to-scalar ratio of $r \sim 10^{-6}$. Inverting this relationship yields a bound on the tensor tilt sourced by scalar fluctuations. Since this induced GW spectrum depends on the scalar spectrum, we derive a new indirect bound that involves *all scales* of the scalar spectrum based on CMB observations. This bound comes from the constraint on the number of effective relativistic degrees of freedom, $N_{\rm eff}$. The bound forces the running and running of running to conform to standard slow-roll predictions of $\alpha, \beta \lesssim (n_s - 1)^2$, improving on current CMB measurements by an order of magnitude. Performing a likelihood analysis including this new constraint, we find that positive α and/or β are disfavored at least at 1σ. Even using conservative analysis $\beta + 0.074\ \alpha > 8.6 \times 10^{-4}$ are ruled out at 3σ.

5.1 Power Spectra and N_{eff}

A stochastic gravitational wave background (GW), could be produced by a multitude of physical phenomena on different eons and scales ranging from Early Universe scenarios through phase transitions to incoherent accumulation of binary black hole coalescence [164, 165, 166, 163, 167, 168]. The fractional energy density stored in GW is therefore an invaluable probe of these physical phenomena. One can probe the energy density of the stochastic gravitational wave background in several ways in different epochs and on different wavelengths. Cosmic Microwave Background Radiation (CMB) observations, and specifically the B-mode polarization measurements, have persistently probed GW on the largest possible scales and have tested Early Universe scenarios, most notably inflation [165, 166]. Such measurements probe the GW energy density at the time of decoupling.

Early Universe models based on quantum fluctuations, whether inflation or bounce, predict a primordial scalar/density spectrum and a tensor/GW spectrum. Our focus henceforth will be on these spectra and on ways to constrain them. CMB and BAO measurements have measured the scalar spectrum on scales $H_0 < k < 1Mpc^{-1}$ to be

$$P_S = A_s \left(\frac{k}{k_0}\right)^{n_s-1}, \quad A_s = 2.1 \times 10^{-9}, \quad n_s = 0.965 \tag{5.1}$$

and have placed an upper bound on the similarly defined GW spectrum $P_T = A_T \left(\frac{k}{k_0}\right)^{n_T}$ in the form of the scalar to tensor ratio r, [165, 166]:

$$r \equiv \frac{P_T}{P_S}|_{k_0} \leq 0.06 \tag{5.2}$$

k_0 is the so called pivot scale that somewhat differs from one experiment to the other, but for our purposes we shall take it to be $k_0 = 0.05\ Mpc^{-1}$. In the following, $k_{eq} = 0.01\ Mpc^{-1}$ in compliance with Planck 2018 analysis.

The GW energy density contributes to the number of effective relativistic d.o.f. at the

time of decoupling, $N_{\rm eff}$. The dependence of $N_{\rm eff}$ on the GW spectrum was derived in [169].

$$\Delta N_{\rm eff} = \left(N_{\rm eff} + \frac{8}{7} \left(\frac{11}{4} \right)^{4/3} \right) \frac{1}{12} \int d \ln k \, P_T \tag{5.3}$$

where $N_{\rm eff} = 3.046$ is the Standard Model prediction and current 68% confidence level suggest $\Delta N_{\rm eff} \leq 0.19$. Thus, $N_{\rm eff}$ provides an indirect probe of all scales of the GW spectrum. It is important to note that as long as r is not measured, (5.3) holds limited promise, as the amplitude A_T and therefore r can be arbitrarily small. Bouncing models, for instance, predict $r < 10^{-30}$, and only a handful suggest an observable r [170, 171].

A similar situation of inaccessibility occurs for the scalar spectrum, where we have so far probed only 8 out of the expected $50-60$ 'e-folds' of inflation. This limit is not expected to improve in the near future, due to built-in non-linearities. Nevertheless, indirect probes have provided useful indications and constraints on the scalar spectrum [172, 173, 174, 175, 176, 177] on scales beyond primary CMB scales.

The above discussion implicitly assumed full decoupling between the scalar and tensor modes. It is valid in first order in perturbation theory. However, at second order, scalar fluctuations act as sources of tensor fluctuations [178, 179, 180]. These induced, second order tensor fluctuations are related to the scalar (first order) spectrum via $P_T^{(2)} \sim P_S^2$. Given the already measured scalar spectrum (5.1), one is guaranteed a tensor signal at the level of $r \sim 10^{-6}$ on CMB scales. If, in the distant future, such a signal is not measured, we have misinterpreted our Early Universe paradigm or detected violations of general relativity. Analysis related to this second order GW spectrum and its phenomenological consequences has recently been discussed in [181, 182, 183, 184]

By adapting (5.3) to the induced spectrum, it will also contribute to $N_{\rm eff}$. $N_{\rm eff}$ will now be sensitive to *all scales* of the *scalar spectrum*. Hence, we have novel probes of the scalar power spectrum at scales inaccessible to primary CMB constraints. Moreover this indirect $N_{\rm eff}$ constraint is based on CMB data alone. Given that $N_{\rm eff}$ will include an integral

over all scales it will be sensitive to enhancements of the spectrum and to the smallest scales, i.e. the UV cut-off. We find that $N_{\rm eff}$ strongly constrains deviations from the constant n_s spectrum. In particular it forces the running and the running-of-running to conform to the standard slow-roll hierarchy, $\alpha, \beta \lesssim (n_s - 1)^2$. Such a constraint rules out a large portion of the parameter space allowed by Planck. We perform a likelihood analysis including the $N_{\rm eff}$ constraint and find that positive α, β are disfavored by at least 1σ and $\beta + 0.074\,\alpha > 8.6 \times 10^{-4}$ are ruled out at 3σ.

5.2 Forecasted Limits from CMB

Here we look to the future and list different CMB experiments and their forecasts for relevant parameters including the tensor to scalar ratio r, uncertainty on the effective number of neutrinos $\sigma N_{\rm eff}$, and the GW energy density Ω_{GW}. These CMB observations probe the GW energy density at the time of decoupling. Usually this is specified in terms of r, the tensor-to scalar ratio and wavenumber k. These measurements probe the GW energy density on largest scales, $k \lesssim k_{eq}$, in addition to $N_{\rm eff}$. In Table 5.1 we list the different experiments and their forecasted sensitivities. The relation between P_T and present day Ω_{GW} is [180]:

$$\Omega_{GW} = 4.2 \times 10^{-2} r A_s \left(\frac{k}{k_0}\right)^{n_T} \frac{a_{eq}}{a(\eta_0)} \,. \tag{5.4}$$

Carrying out the CMB experiments up to Stage 4 will decisively constrain a narrow space of allowed inflationary models, or will rule out all large field models. Besides specifying the forecasts for various experiments, we performed a Fisher matrix analysis of cosmic variance limited (CVL) CMB polarization measurement. The analysis predicts $\sigma(r) = 2.2 \times 10^{-6}$ for $f_{sky} = 0.8$ with no delensing and ignoring beam systematics. Such value seems very close to the induced second order GW spectrum prediction of $r \sim 10^{-6}$, which is close to a guaranteed signal.

Table 5.1: The forecast of constraints on r and $\Delta N_{\rm eff}$ for different experiments. The details were taken from [185]. The quoted bound on r for the CMB future probes is the forecast for $\sigma(r)$. The CVL result is based on a Fisher matrix analysis.

Experimental stage	$r <$	$\sigma N_{\rm eff}$	$\Omega_{GW} <$
present	0.06	0.19	1.6×10^{-15}
S2	0.035	0.14	9.1×10^{-16}
SO	0.006	0.04	1.6×10^{-16}
S4	0.0005	0.027	1.3×10^{-17}
CVL	2.2×10^{-6}	3.1×10^{-6}	5.6×10^{-20}

5.3 Constraining the scalar spectrum using $N_{\rm eff}$

From calculations done in [178, 179, 180], the induced tensor power due to the scalar power spectrum has the form

$$P_T(k) = \frac{A_{GW}}{3} P_S^2(k), \tag{5.5}$$

which results in a change to $N_{\rm eff}$ induced by this second order effect

$$\Delta N_{\rm eff} = \left(N_{\rm eff} + \frac{8}{7}\left(\frac{11}{4}\right)^{4/3} \right) \frac{A_{GW}}{36} \int d\ln k \, P_S^2(k). \tag{5.6}$$

While the scalar power spectrum is well described by the simple power law form parameterized by n_s, the above integral covers all scales and is subject to a UV cutoff. This gives us extraordinary leverage to use CMB measurements of $N_{\rm eff}$ to constrain $P_S(k)$ for modes much smaller than the relevant CMB scales. For this reason we consider a power spectrum parameterized by the running α and the running of running β,

$$\ln P_{S,run}(k) = \ln A_S + \ln\left(\frac{k}{k_0}\right)\left[n_s - 1 + \frac{1}{2}\alpha \ln\left(\frac{k}{k_0}\right) + \frac{1}{6}\beta \ln^2\left(\frac{k}{k_0}\right)\right]. \tag{5.7}$$

To get an idea of the constraining power that Equation 5.6 has on this parametrization of the scalar spectrum we can numerically solve the integral for values of α and β and compare to the Planck 2018 uncertainty on $N_{\rm eff}$ of $\sigma N_{eff} = 0.19$ [165, 166]. Figure 5.1, taken from Planck 2015 data with $n_s = 0.97, k_{UV}/k_0 = 10^{21}$, shows the likelihood contours from Planck

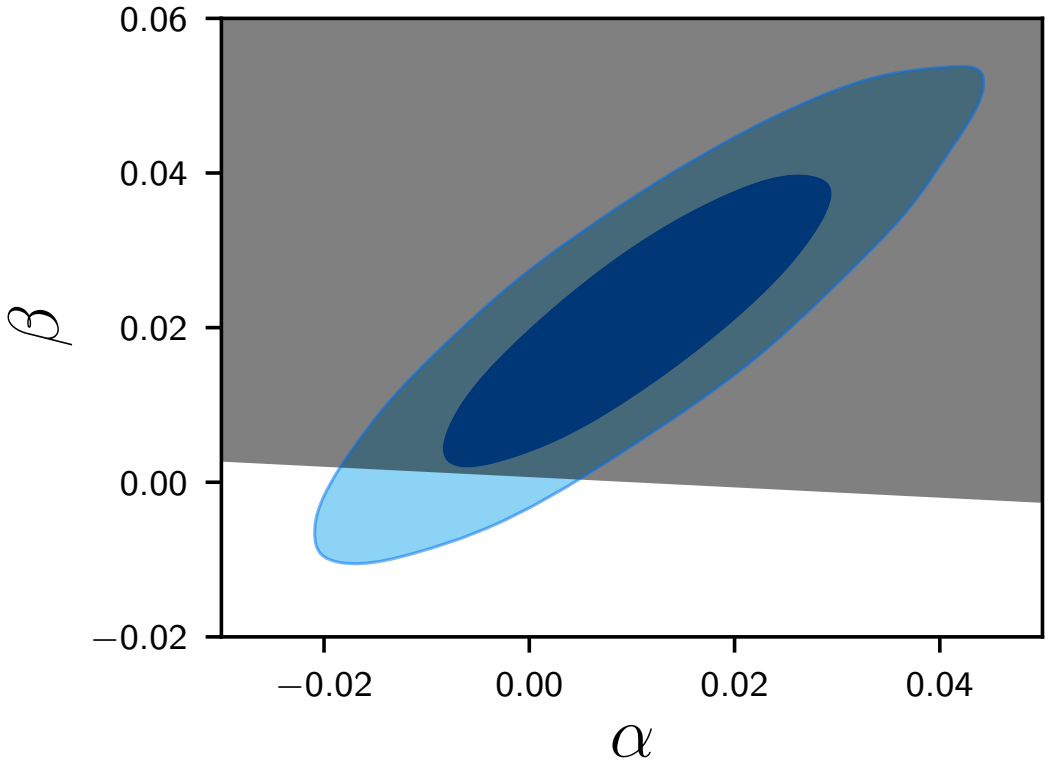

Figure 5.1: Planck 2015 constraints on running α and running of running β. Taking into account the contribution of 2nd order tensors to $N_{\rm eff}$, the shaded region is ruled out assuming $k_{UV}/k_0 = 10^{21}$ and $n_s = 0.97$.

data alone. The gray shaded region is excluded by this second order integral contribution to $N_{\rm eff}$, which severely limits the parameter space, especially for positive values of β.

Thus, slow-roll hierarchy must be maintained, and in particular having either α or $\beta \sim (n_s - 1)$ will violate the $N_{\rm eff}$ bound. Hence, our result confirms that the only valid models are the ones where the slow-roll hierarchy is maintained and at most $\alpha, \beta \lesssim few \times (n_s - 1)^2$ for positive running.

5.4 Likelihood Analysis

A proper estimation of cosmological parameters requires a likelihood analysis allowing several parameters to vary with proper priors. We have seen that the bound is most useful

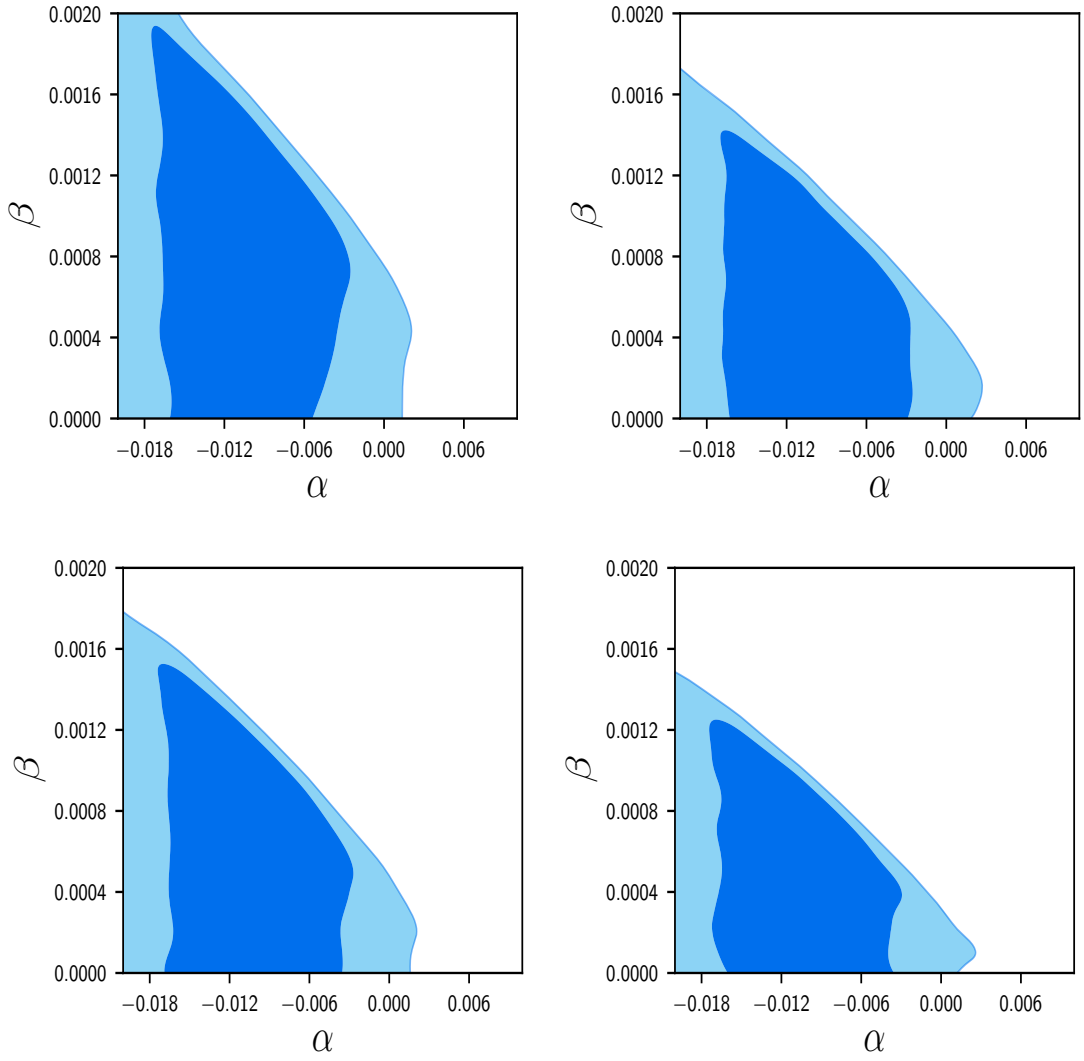

Figure 5.2: Top panel: 68% and 95% confidence level contours of α, β taking into account the bound on $2\Delta N_{\rm eff} \leq 0.46$ for $n_s(k_0) = 0.95$ and $k_{UV}/k_0 = 10^{21}$ (top left), $k_{UV}/k_0 = 10^{24}$ (top right). Bottom panel: Same as top panel with $n_s(k_0) = 0.97$.

in constraining the running α and the running of running β. We therefore ran a CosmoMC analysis allowing the variation of α, β and we considered spectral tilts $n_s = 0.95, 0.97$ and various cut-offs $k_{UV}/k_0 = 10^{21}, 10^{24}$ corresponding roughly to two decades beyond the LIGO band and 60 e-folds of inflation respectively.

Our likelihood analysis uses data from BICEP2, Planck, HST, BAO and the KECK/Planck cross correlation analysis [165, 166, 186]. In addition to the base CosmoMC software distribution [187], we created an additional likelihood module to calculate ΔN_{eff} as a function of our running parameters,

$$\Delta N_{\text{eff}}(\alpha, \beta) = \left(N_{\text{eff}} + \frac{8}{7} \left(\frac{11}{4} \right)^{4/3} \right) \frac{A_{GW}^{(2)}}{36} \int^{k_{UV}} d \ln k \; P_{S,run}^2(k; \alpha, \beta), \tag{5.8}$$

where $P_{S,run}$ is defined in (5.7). In the absence of a closed form solution to the integral for ΔN_{eff}, we precomputed a grid of values for different inputs of α, β that are then used in the MCMC analysis. The likelihood plots corresponding to each pair of $(n_s(k_0), k_{UV}/k_0)$ are plotted in Figure 5.2. They are the results of running our modified version of CosmoMC with its own precomputed grid of N_{eff} values. We use spacings of $\Delta\alpha = 4 \times 10^{-4}, \Delta\beta = 2 \times 10^{-5}$ and compute $N_{\text{eff}}(\alpha, \beta)$ using bilinear interpolation for generic values of α, β.

It is clear that both parameters are severely constrained with $\alpha, \beta < 0.002$. This is an order of magnitude improvement over compared to Planck bounds, and in accord with standard slow-roll predictions of $\alpha \sim (n_s - 1)^2$ and $\beta \sim (n_s - 1)^3$. Using the likelihood data from this analysis, we can place upper limits on linear combinations of α and β for each distribution. Table 5.2 summarizes the 68% 95% and 99.7% upper limits for each distribution shown in Figure 5.2. The most conservative analysis (3σ) gives the following bound $\beta + 0.074\ \alpha < 8.6 \times 10^{-4}$. It would be interesting to include the LIGO data in a future likelihood analysis, potentially strengthening these bounds.

Table 5.2: Upper Limits on combinations of α and β obtained from our CosmoMC likelihood distributions

$n_s(k_0)$	k_{UV}/k_0	parameter	68% u.l.	95% u.l.	99.7% u.l.
0.95	10^{21}	$\beta + 0.074\ \alpha$	3.8×10^{-4}	7.7×10^{-4}	8.6×10^{-4}
0.95	10^{24}	$\beta + 0.063\ \alpha$	2.1×10^{-4}	5.0×10^{-4}	5.5×10^{-4}
0.97	10^{21}	$\beta + 0.067\ \alpha$	2.1×10^{-4}	5.1×10^{-4}	5.7×10^{-4}
0.97	10^{24}	$\beta + 0.059\ \alpha$	1.2×10^{-4}	3.6×10^{-4}	4.1×10^{-4}

5.5 Acknowledgements

Chapter 5, in part, contains a reprint of material as it appears in I. Ben-Dayan, B. Keating, D. Leon and I. Wolfson, "Constraints on scalar and tensor spectra from N_{eff}," J. Cosmology Astropart. Phys., 2019, 007, 2019 (arXiv:1903.11843) [4]. The dissertation author made essential contributions to this work.

Chapter 6

Conclusion

We have seen in the previous chapters a few of the many ways that cosmological information can give us insight into the evolution of the universe and let us search for physics beyond our current theories. Among the work presented here are a number of noteworthy results.

Optical polarimetry of two AGN in Lum and Ic bands placed upper limits on SME coefficients corresponding to birefringent effects, and combining these two bands can increase the power of our constraints in some cases by more than a factor of 10 compared to the Ic alone.

Observations of the polarized CMB from the POLARBEAR experiment have demonstrated a detection of gravitational lensing in a polarization-dominated CMB dataset from small, deep observational patches. A measurement of the lensing amplitude at 4.1σ significance and rejection of the no-lensing hypothesis at 10.9σ contribute to a future of using CMB polarization to understand the cosmos.

A treatment of second order tensor perturbations combined with a likelihood analysis of the CMB have greatly improved limits on a running scalar power spectrum compared to the limits from CMB alone. Stringent bounds on positive values of α and β provide guidance on evaluating models of inflation and other early universe physics.

Looking to future experiments, the Simons Array will expand on the work of POLARBEAR by studing CMB polarization with roughly an order of magnitude more detectors and observations in multiple frequency bands. [188] The Simons Observatory furthers these goals with the addition of new large and small aperture telescopes. [185]

The work here to place limits on the SME also continues. Applying lessons from using multiple simultaneous broadband measurements to larger aperture telescopes promises to further improve upon existing constraints. [189] Similarly, leveraging the relative abundance of optical polarimetry measurements shows that using many lines of sight not only improves constraints but allows the consideration of SME coefficients of higher dimensions. [190]

Taken altogether, the results presented in this dissertation demonstrate that there are still many ways to explore the universe when we look into the distance.

Bibliography

[1] D. Leon, J. Kaufman, B. Keating, and M. Mewes. The cosmic microwave background and pseudo-Nambu-Goldstone bosons: Searching for Lorentz violations in the cosmos. Mod. Phys. Lett. A, 32:1730002, January 2017.

[2] Andrew S. Friedman, David Leon, Kevin D. Crowley, Delwin Johnson, Grant Teply, David Tytler, Brian G. Keating, and Gary M. Cole. Constraints on lorentz invariance and *cpt* violation using optical photometry and polarimetry of active galaxies bl lacertae and s5 B0716 + 714. Phys. Rev. D, 99:035045, Feb 2019.

[3] M. Aguilar Faúndez, K. Arnold, C. Baccigalupi, D. Barron, D. Beck, S. Beckman, F. Bianchini, J. Carron, K. Cheung, Y. Chinone, H. El Bouhargani, T. Elleflot, J. Errard, G. Fabbian, C. Feng, T. Fujino, N. Goeckner-Wald, T. Hamada, M. Hasegawa, M. Hazumi, C. A. Hill, H. Hirose, O. Jeong, N. Katayama, B. Keating, S. Kikuchi, A. Kusaka, A. T. Lee, D. Leon, E. Linder, L. N. Lowry, F. Matsuda, T. Matsumura, Y. Minami, M. Navaroli, H. Nishino, A. T. P. Pham, D. Poletti, G. Puglisi, C. L. Reichardt, Y. Segawa, B. D. Sherwin, M. Silva-Feaver, P. Siritanasak, R. Stompor, A. Suzuki, O. Tajima, S. Takatori, D. Tanabe, G. P. Teply, and C. Tsai and. Measurement of the cosmic microwave background polarization lensing power spectrum from two years of POLARBEAR data. The Astrophysical Journal, 893(1):85, apr 2020.

[4] Ido Ben-Dayan, Brian Keating, David Leon, and Ira Wolfson. Constraints on scalar and tensor spectra from neff. Journal of Cosmology and Astroparticle Physics, 2019(06):007–007, jun 2019.

[5] V. A. Kostelecký and M. Mewes. Astrophysical Tests of Lorentz and CPT Violation with Photons. ApJ, 689:L1–L4, December 2008.

[6] P. Sikivie. Axion Cosmology. In M. Kuster, G. Raffelt, and B. Beltrán, editors, Axions, volume 741 of Lecture Notes in Physics, Berlin Springer Verlag, page 19, 2008.

[7] B. Ratra and P. J. E. Peebles. Cosmological consequences of a rolling homogeneous scalar field. Phys. Rev. D, 37:3406–3427, June 1988.

[8] L. J. Rosenberg and G. Rybka. Axions and other similar particles. The Review of Particle Physics, April 2014.

[9] S. C. Cindy Ng and D. L. Wiltshire. Properties of cosmologies with dynamical pseudo Nambu-Goldstone bosons. Phys. Rev. D, 63(2):023503, January 2001.

[10] R. Z. Ferreira and M. S. Sloth. Universal constraints on axions from inflation. Journal of High Energy Physics, 12:139, December 2014.

[11] The POLARBEAR Collaboration. A Measurement of the Cosmic Microwave Background B-mode Polarization Power Spectrum at Sub-degree Scales with POLARBEAR. ApJ, 794:171, October 2014.

[12] R. D. Peccei. QCD, strong CP and axions. Journal of Korean Physical Society, 29:199, September 1996.

[13] C. T. Hill and A. K. Leibovich. Natural theories of ultralow mass pseudo Nambu-Goldstone bosons: Axions and quintessence. Phys. Rev. D, 66(7):075010, October 2002.

[14] V. Gluscevic. CMB as a Probe of New Physics and Old Times. PhD thesis, California Institute of Technology, 2013.

[15] D. Colladay and V. A. Kostelecký. CPT violation and the standard model. Phys. Rev. D, 55:6760–6774, June 1997.

[16] D. Colladay and V. A. Kostelecký. Lorentz-violating extension of the standard model. Phys. Rev. D, 58(11):116002, December 1998.

[17] V. A. Kostelecký. Gravity, Lorentz violation, and the standard model. Phys. Rev. D, 69(10):105009, May 2004.

[18] V. A. Kostelecký and M. Mewes. Signals for Lorentz violation in electrodynamics. Phys. Rev. D, 66(5):056005, September 2002.

[19] V. A. Kostelecký and M. Mewes. Electrodynamics with Lorentz-violating operators of arbitrary dimension. Phys. Rev. D, 80(1):015020, July 2009.

[20] V. A. Kostelecký and M. Mewes. Lorentz-Violating Electrodynamics and the Cosmic Microwave Background. Physical Review Letters, 99(1):011601, July 2007.

[21] The Polarbear Collaboration: P. A. R. Ade, Y. Akiba, A. E. Anthony, K. Arnold, M. Atlas, D. Barron, D. Boettger, J. Borrill, S. Chapman, Y. Chinone, M. Dobbs, T. Elleflot, J. Errard, G. Fabbian, C. Feng, D. Flanigan, A. Gilbert, W. Grainger, N. W. Halverson, M. Hasegawa, K. Hattori, M. Hazumi, W. L. Holzapfel, Y. Hori, J. Howard, P. Hyland, Y. Inoue, G. C. Jaehnig, A. H. Jaffe, B. Keating, Z. Kermish, R. Keskitalo, T. Kisner, M. Le Jeune, A. T. Lee, E. M. Leitch, E. Linder, M. Lungu, F. Matsuda, T. Matsumura, X. Meng, N. J. Miller, H. Morii, S. Moyerman, M. J. Myers, M. Navaroli, H. Nishino, A. Orlando, H. Paar, J. Peloton, D. Poletti, E. Quealy, G. Rebeiz, C. L. Reichardt, P. L. Richards, C. Ross, I. Schanning, D. E. Schenck, B. D. Sherwin, A. Shimizu, C. Shimmin, M. Shimon, P. Siritanasak, G. Smecher, H. Spieler, N. Stebor, B. Steinbach, R. Stompor, A. Suzuki, S. Takakura, T. Tomaru, B. Wilson, A. Yadav, and O. Zahn. A Measurement of the Cosmic Microwave Background B-mode Polarization Power Spectrum at Sub-degree Scales with POLARBEAR. ApJ, 794:171, October 2014.

[22] B. G. Keating, M. Shimon, and A. P. S. Yadav. Self-calibration of Cosmic Microwave Background Polarization Experiments. ApJ, 762:L23, January 2013.

[23] J. P. Kaufman, B. G. Keating, and B. R. Johnson. Precision tests of parity violation over cosmological distances. MNRAS, 455:1981–1988, January 2016.

[24] V. A. Kostelecký and N. Russell. Data tables for Lorentz and CPT violation. Rev. Mod. Phys., 83:11–32, January 2011.

[25] R. C. Myers and M. Pospelov. Ultraviolet Modifications of Dispersion Relations in Effective Field Theory. Phys. Rev. Lett., 90(21):211601, May 2003.

[26] G. Amelino-Camelia, D. Guetta, and T. Piran. ICECUBE Neutrinos and Lorentz Invariance Violation. ApJ, 806:269, June 2015.

[27] U. Jacob and T. Piran. Neutrinos from gamma-ray bursts as a tool to explore quantum-gravity-induced Lorentz violation. Nature Phys., 3:87–90, February 2007.

[28] U. Jacob and T. Piran. Lorentz-violation-induced arrival delays of cosmological particles. J. Cosmology Astropart. Phys., 1:031, January 2008.

[29] S. Chakraborty, A. Mirizzi, and G. Sigl. Testing Lorentz invariance with neutrino bursts from supernova neutronization. Phys. Rev. D, 87(1):017302, January 2013.

[30] F. W. Stecker and S. T. Scully. Propagation of superluminal PeV IceCube neutrinos: A high energy spectral cutoff or new constraints on Lorentz invariance violation. Phys. Rev. D, 90(4):043012, August 2014.

[31] S. T. Scully and F. W. Stecker. Lorentz invariance violation and the observed spectrum of ultrahigh energy cosmic rays. Astropart. Phys., 31:220–225, April 2009.

[32] F. W. Stecker. Gamma-ray and Cosmic-ray Tests of Lorentz Invariance Violation and Quantum Gravity Models and Their Implications. In C. Cecchi, S. Ciprini, P. Lubrano, and G. Tosti, editors, Amer. Inst. Phys. Conf. Ser., volume 1223, pages 192–206, March 2010.

[33] W. Bietenholz. Cosmic rays and the search for a Lorentz Invariance Violation. Phys. Rep., 505:145–185, August 2011.

[34] R. Cowsik, T. Madziwa-Nussinov, S. Nussinov, and U. Sarkar. Testing violations of Lorentz invariance with cosmic rays. Phys. Rev. D, 86(4):045024, August 2012.

[35] R. G. Lang and V. de Souza. Astroparticle Physics Tests of Lorentz Invariance Violation. In J. Phys. Conf. Ser., volume 866, page 012008, June 2017.

[36] V. A. Kostelecký and M. Mewes. Astrophysical Tests of Lorentz and CPT Violation with Photons. ApJ, 689:L1, December 2008.

[37] C. Pfeifer. Redshift and lateshift from homogeneous and isotropic modified dispersion relations. Phys. Lett. B, 780:246–250, May 2018.

[38] S. M. Carroll, G. B. Field, and R. Jackiw. Limits on a Lorentz- and parity-violating modification of electrodynamics. Phys. Rev. D, 41:1231–1240, February 1990.

[39] V. A. Kostelecký and M. Mewes. Electrodynamics with Lorentz-violating operators of arbitrary dimension. Phys. Rev. D, 80(1):015020, July 2009.

[40] F. Kislat and H. Krawczynski. Planck-scale constraints on anisotropic Lorentz and C P T invariance violations from optical polarization measurements. Phys. Rev. D, 95(8):083013, April 2017.

[41] K. Nilsson, T. Pursimo, A. Sillanpää, L. O. Takalo, and E. Lindfors. Detection of the host galaxy of S5 0716+714. A&A, 487:L29–L32, August 2008.

[42] C. W. Danforth, K. Nalewajko, K. France, and B. A. Keeney. A Fast Flare and Direct Redshift Constraint in Far-ultraviolet Spectra of the Blazar S5 0716+714. ApJ, 764:57, February 2013.

[43] R. C. Vermeulen, P. M. Ogle, H. D. Tran, I. W. A. Browne, M. H. Cohen, A. C. S. Readhead, G. B. Taylor, and R. W. Goodrich. When Is BL Lac Not a BL Lac? ApJ, 452:L5, October 1995.

[44] G. Amelino-Camelia. Doubly-Special Relativity: Facts, Myths and Some Key Open Issues, pages 123–170. World Scientific Publishing Co, 2010.

[45] L. Smolin. Classical paradoxes of locality and their possible quantum resolutions in deformed special relativity. Gen. Rel. Grav., 43:3671–3691, December 2011.

[46] E. Komatsu, J. Dunkley, M. R. Nolta, C. L. Bennett, B. Gold, G. Hinshaw, N. Jarosik, D. Larson, M. Limon, L. Page, D. N. Spergel, M. Halpern, R. S. Hill, A. Kogut, S. S. Meyer, G. S. Tucker, J. L. Weiland, E. Wollack, and E. L. Wright. Five-Year Wilkinson Microwave Anisotropy Probe Observations: Cosmological Interpretation. ApJS, 180:330–376, February 2009.

[47] G. Gubitosi, L. Pagano, G. Amelino-Camelia, A. Melchiorri, and A. Cooray. A constraint on Planck-scale modifications to electrodynamics with CMB polarization data. J. Cosmology Astropart. Phys., 8:021, August 2009.

[48] T. Kahniashvili, R. Durrer, and Y. Maravin. Testing Lorentz invariance violation with Wilkinson Microwave Anisotropy Probe five year data. Phys. Rev. D, 78(12):123009, December 2008.

[49] J. P. Kaufman, B. G. Keating, and B. R. Johnson. Precision tests of parity violation over cosmological distances. MNRAS, 455:1981–1988, January 2016.

[50] J. Kaufman, D. Leon, and B. Keating. Using the Crab Nebula as a high precision calibrator for cosmic microwave background polarimeters. Int. J. Mod. Phys. D, 25:1640008, March 2016.

[51] J. P. Kaufman, N. J. Miller, M. Shimon, D. Barkats, C. Bischoff, I. Buder, B. G. Keating, J. M. Kovac, P. A. R. Ade, R. Aikin, J. O. Battle, E. M. Bierman, J. J. Bock, H. C. Chiang, C. D. Dowell, L. Duband, J. Filippini, E. F. Hivon, W. L. Holzapfel, V. V. Hristov, W. C. Jones, S. S. Kernasovskiy, C. L. Kuo, E. M. Leitch, P. V. Mason, T. Matsumura, H. T. Nguyen, N. Ponthieu, C. Pryke, S. Richter, G. Rocha, C. Sheehy, M. Su, Y. D. Takahashi, J. E. Tolan, and K. W. Yoon. Self-calibration of BICEP1 three-year data and constraints on astrophysical polarization rotation. Phys. Rev. D, 89(6):062006, March 2014.

[52] G. Amelino-Camelia, J. Ellis, N. E. Mavromatos, D. V. Nanopoulos, and S. Sarkar. Tests of quantum gravity from observations of γ-ray bursts. Nature, 393:763–765, June 1998.

[53] S. E. Boggs, C. B. Wunderer, K. Hurley, and W. Coburn. Testing Lorentz Invariance with GRB 021206. ApJ, 611:L77–L80, August 2004.

[54] J. Ellis, N. E. Mavromatos, D. V. Nanopoulos, A. S. Sakharov, and E. K. G. Sarkisyan. Robust limits on Lorentz violation from gamma-ray bursts. Astropart. Phys., 25:402–411, July 2006.

[55] M. Rodr´iguez Mart´inez and T. Piran. Constraining Lorentz violations with gamma ray bursts. J. Cosmology Astropart. Phys., 4:006, April 2006.

[56] T. Kahniashvili, G. Gogoberidze, and B. Ratra. Gamma ray burst constraints on ultraviolet Lorentz invariance violation. Phys. Lett. B, 643:81–85, December 2006.

[57] M. Biesiada and A. Piórkowska. Gamma-ray burst neutrinos, Lorenz invariance violation and the influence of background cosmology. J. Cosmology Astropart. Phys., 5:011, May 2007.

[58] Z. Xiao and B.-Q. Ma. Constraints on Lorentz invariance violation from gamma-ray burst GRB090510. Phys. Rev. D, 80(11):116005, December 2009.

[59] P. Laurent, D. Götz, P. Binétruy, S. Covino, and A. Fernandez-Soto. Constraints on Lorentz Invariance Violation using integral/IBIS observations of GRB041219A. Phys. Rev. D, 83(12):121301, June 2011.

[60] F. W. Stecker. A new limit on Planck scale Lorentz violation from γ-ray burst polarization. Astropart. Phys., 35:95–97, September 2011.

[61] K. Toma, S. Mukohyama, D. Yonetoku, T. Murakami, S. Gunji, T. Mihara, Y. Morihara, T. Sakashita, T. Takahashi, Y. Wakashima, H. Yonemochi, and N. Toukairin. Strict Limit on CPT Violation from Polarization of γ-Ray Bursts. Phys. Rev. Lett., 109(24):241104, December 2012.

[62] V. A. Kostelecký and M. Mewes. Constraints on Relativity Violations from Gamma-Ray Bursts. Phys. Rev. Lett., 110(20):201601, May 2013.

[63] V. Vasileiou, A. Jacholkowska, F. Piron, J. Bolmont, C. Couturier, J. Granot, F. W. Stecker, J. Cohen-Tanugi, and F. Longo. Constraints on Lorentz invariance violation from Fermi-Large Area Telescope observations of gamma-ray bursts. Phys. Rev. D, 87(12):122001, June 2013.

[64] Y. Pan, Y. Gong, S. Cao, H. Gao, and Z.-H. Zhu. Constraints on the Lorentz Invariance Violation with Gamma-Ray Bursts via a Markov Chain Monte Carlo Approach. ApJ, 808:78, July 2015.

[65] S. Zhang and B.-Q. Ma. Lorentz violation from gamma-ray bursts. Astropart. Phys., 61:108–112, February 2015.

[66] Z. Chang, X. Li, H.-N. Lin, Y. Sang, P. Wang, and S. Wang. Constraining Lorentz invariance violation from the continuous spectra of short gamma-ray bursts. Chin. Phys. C, 40(4):045102, April 2016.

[67] H.-N. Lin, X. Li, and Z. Chang. Gamma-ray burst polarization reduction induced by the Lorentz invariance violation. MNRAS, 463:375–381, November 2016.

[68] J.-J. Wei, B.-B. Zhang, L. Shao, X.-F. Wu, and P. Mészáros. A New Test of Lorentz Invariance Violation: The Spectral Lag Transition of GRB 160625B. ApJ, 834:L13, January 2017.

[69] S. D. Biller, A. C. Breslin, J. Buckley, M. Catanese, M. Carson, D. A. Carter-Lewis, M. F. Cawley, D. J. Fegan, J. P. Finley, J. A. Gaidos, A. M. Hillas, F. Krennrich, R. C. Lamb, R. Lessard, C. Masterson, J. E. McEnery, B. McKernan, P. Moriarty, J. Quinn, H. J. Rose, F. Samuelson, G. Sembroski, P. Skelton, and T. C. Weekes. Limits to Quantum Gravity Effects on Energy Dependence of the Speed of Light from Observations of TeV Flares in Active Galaxies. Phys. Rev. Lett., 83:2108–2111, September 1999.

[70] MAGIC Collaboration, J. Albert, E. Aliu, H. Anderhub, L. A. Antonelli, P. Antoranz, M. Backes, C. Baixeras, J. A. Barrio, H. Bartko, D. Bastieri, J. K. Becker, W. Bednarek, K. Berger, E. Bernardini, C. Bigongiari, A. Biland, R. K. Bock, G. Bonnoli, P. Bordas, V. Bosch-Ramon, T. Bretz, I. Britvitch, M. Camara, E. Carmona, A. Chilingarian, S. Commichau, J. L. Contreras, J. Cortina, M. T. Costado, S. Covino, V. Curtef, F. Dazzi, A. de Angelis, E. de Cea Del Pozo, C. Delgado Mendez, R. de Los Reyes, B. de Lotto, M. de Maria, F. de Sabata, A. Dominguez, D. Dorner, M. Doro, M. Errando, M. Fagiolini, D. Ferenc, E. Fernández, R. Firpo, M. V. Fonseca, L. Font, N. Galante, R. J. Garc´ia López, M. Garczarczyk, M. Gaug, F. Goebel, M. Hayashida, A. Herrero, D. Höhne, J. Hose, C. C. Hsu, S. Huber, T. Jogler, D. Kranich, A. La Barbera, A. Laille, E. Leonardo, E. Lindfors, S. Lombardi, F. Longo, M. López, E. Lorenz, P. Majumdar, G. Maneva, N. Mankuzhiyil, K. Mannheim, L. Maraschi, M. Mariotti, M. Mart´inez, D. Mazin, M. Meucci, M. Meyer, J. M. Miranda, R. Mirzoyan, M. Moles, A. Moralejo, D. Nieto, K. Nilsson, J. Ninkovic, N. Otte, I. Oya, M. Panniello, R. Paoletti, J. M. Paredes, M. Pasanen, D. Pascoli, F. Pauss, R. G. Pegna, M. A. Perez-Torres, M. Persic, L. Peruzzo, A. Piccioli, F. Prada, E. Prandini, N. Puchades, A. Raymers, W. Rhode,

M. Ribó, J. Rico, M. Rissi, A. Robert, S. Rügamer, A. Saggion, T. Y. Saito, M. Salvati, M. Sanchez-Conde, P. Sartori, K. Satalecka, V. Scalzotto, V. Scapin, R. Schmitt, T. Schweizer, M. Shayduk, K. Shinozaki, N. Sidro, A. Sierpowska-Bartosik, A. Sillanpää, D. Sobczynska, F. Spanier, A. Stamerra, L. S. Stark, L. Takalo, F. Tavecchio, P. Temnikov, D. Tescaro, M. Teshima, M. Tluczykont, D. F. Torres, N. Turini, H. Vankov, A. Venturini, V. Vitale, R. M. Wagner, W. Wittek, V. Zabalza, F. Zandanel, R. Zanin, J. Zapatero, J. Ellis, N. E. Mavromatos, D. V. Nanopoulos, A. S. Sakharov, and E. K. G. Sarkisyan. Probing quantum gravity using photons from a flare of the active galactic nucleus Markarian 501 observed by the MAGIC telescope. Phys. Lett. B, 668:253–257, October 2008.

[71] F. Aharonian, A. G. Akhperjanian, U. Barres de Almeida, A. R. Bazer-Bachi, Y. Becherini, B. Behera, M. Beilicke, W. Benbow, K. Bernlöhr, C. Boisson, A. Bochow, V. Borrel, I. Braun, E. Brion, J. Brucker, P. Brun, R. Bühler, T. Bulik, I. Büsching, T. Boutelier, S. Carrigan, P. M. Chadwick, A. Charbonnier, R. C. G. Chaves, L.-M. Chounet, A. C. Clapson, G. Coignet, L. Costamante, M. Dalton, B. Degrange, C. Deil, H. J. Dickinson, A. Djannati-Ata¨i, W. Domainko, L. O. '. Drury, F. Dubois, G. Dubus, J. Dyks, K. Egberts, D. Emmanoulopoulos, P. Espigat, C. Farnier, F. Feinstein, A. Fiasson, A. Förster, G. Fontaine, M. Füßling, S. Gabici, Y. A. Gallant, L. Gérard, B. Giebels, J. F. Glicenstein, B. Glück, P. Goret, C. Hadjichristidis, D. Hauser, M. Hauser, S. Heinz, G. Heinzelmann, G. Henri, G. Hermann, J. A. Hinton, A. Hoffmann, W. Hofmann, M. Holleran, S. Hoppe, D. Horns, A. Jacholkowska, O. C. de Jager, I. Jung, K. Katarzyński, S. Kaufmann, E. Kendziorra, M. Kerschhaggl, D. Khangulyan, B. Khélifi, D. Keogh, N. Komin, K. Kosack, G. Lamanna, J.-P. Lenain, T. Lohse, V. Marandon, J. M. Martin, O. Martineau-Huynh, A. Marcowith, D. Maurin, T. J. L. McComb, C. Medina, R. Moderski, E. Moulin, M. Naumann-Godo, M. de Naurois, D. Nedbal, D. Nekrassov, J. Niemiec, S. J. Nolan, S. Ohm, J.-F. Olive, E. de Oña Wilhelmi, K. J. Orford, J. L. Osborne, M. Ostrowski, M. Panter, G. Pedaletti, G. Pelletier, P.-O. Petrucci, S. Pita, G. Pühlhofer, M. Punch, A. Quirrenbach, B. C. Raubenheimer, M. Raue, S. M. Rayner, M. Renaud, F. Rieger, J. Ripken, L. Rob, S. Rosier-Lees, G. Rowell, B. Rudak, J. Ruppel, V. Sahakian, A. Santangelo, R. Schlickeiser, F. M. Schöck, R. Schröder, U. Schwanke, S. Schwarzburg, S. Schwemmer, A. Shalchi, J. L. Skilton, H. Sol, D. Spangler, Ł. Stawarz, R. Steenkamp, C. Stegmann, G. Superina, P. H. Tam, J.-P. Tavernet, R. Terrier, O. Tibolla, C. van Eldik, G. Vasileiadis, C. Venter, J. P. Vialle, P. Vincent, M. Vivier, H. J. Völk, F. Volpe, S. J. Wagner, M. Ward, A. A. Zdziarski, A. Zech, and H.E.S.S. Collaboration. Limits on an Energy Dependence of the Speed of Light from a Flare of the Active Galaxy PKS 2155-304. Phys. Rev. Lett., 101(17):170402, October 2008.

[72] L. Shao, Z. Xiao, and B.-Q. Ma. Lorentz violation from cosmological objects with very high energy photon emissions. Astropart. Phys., 33:312–315, June 2010.

[73] M. Fairbairn, A. Nilsson, J. Ellis, J. Hinton, and R. White. The CTA sensitivity to Lorentz-violating effects on the gamma-ray horizon. J. Cosmology Astropart. Phys., 6:005, June 2014.

[74] F. Tavecchio and G. Bonnoli. On the detectability of Lorentz invariance violation through anomalies in the multi-TeV γ-ray spectra of blazars. A&A, 585:A25, January 2016.

[75] M. Biesiada and A. Piórkowska. Gravitational lensing time delays as a tool for testing Lorentz-invariance violation. MNRAS, 396:946–950, June 2009.

[76] L. Shao. Tests of Local Lorentz Invariance Violation of Gravity in the Standard Model Extension with Pulsars. Phys. Rev. Lett., 112(11):111103, March 2014.

[77] G. D. Schmidt, H. S. Stockman, and P. S. Smith. Discovery of a sub-megagauss magnetic white dwarf through spectropolarimetry. ApJ, 398:L57–L60, October 1992.

[78] D. Sluse, D. Hutsemékers, H. Lamy, R. Cabanac, and H. Quintana. New optical polarization measurements of quasi-stellar objects. The data. A&A, 433:757–764, April 2005.

[79] P. S. Smith, E. Montiel, S. Rightley, J. Turner, G. D. Schmidt, and B. T. Jannuzi. Coordinated Fermi/Optical Monitoring of Blazars and the Great 2009 September Gamma-ray Flare of 3C 454.3. ArXiv e-prints, December 2009.

[80] V. Piirola, A. Berdyugin, and S. Berdyugina. DIPOL-2: a double image high precision polarimeter. In Ground-based and Airborne Instrumentation for Astronomy V, volume 9147 of Proc. SPIE, page 91478I, August 2014.

[81] A. G. Riess, L. M. Macri, S. L. Hoffmann, D. Scolnic, S. Casertano, A. V. Filippenko, B. E. Tucker, M. J. Reid, D. O. Jones, J. M. Silverman, R. Chornock, P. Challis, W. Yuan, P. J. Brown, and R. J. Foley. A 2.4% Determination of the Local Value of the Hubble Constant. ApJ, 826:56, July 2016.

[82] Planck Collaboration, Ade, P. A. R., Aghanim, N., Arnaud, M., Ashdown, M., Aumont, J., Baccigalupi, C., Banday, A. J., Barreiro, R. B., Bartlett, J. G., Bartolo, N., Battaner, E., Battye, R., Benabed, K., Beno$\hat{}$it, A., Benoit-Lévy, A., Bernard, J.-P., Bersanelli, M., Bielewicz, P., Bock, J. J., Bonaldi, A., Bonavera, L., Bond, J. R., Borrill, J., Bouchet, F. R., Boulanger, F., Bucher, M., Burigana, C., Butler, R. C., Calabrese, E., Cardoso, J.-F., Catalano, A., Challinor, A., Chamballu, A., Chary, R.-R., Chiang, H. C., Chluba, J., Christensen, P. R., Church, S., Clements, D. L., Colombi, S., Colombo, L. P. L., Combet, C., Coulais, A., Crill, B. P., Curto, A., Cuttaia, F., Danese, L., Davies, R. D., Davis, R. J., de Bernardis, P., de Rosa, A., de Zotti, G., Delabrouille, J., Désert, F.-X., Di Valentino, E., Dickinson, C., Diego, J. M., Dolag, K., Dole, H., Donzelli, S., Doré, O., Douspis, M., Ducout, A., Dunkley, J., Dupac, X., Efstathiou, G., Elsner, F., Enßlin, T. A., Eriksen, H. K., Farhang, M., Fergusson, J., Finelli, F., Forni, O., Frailis, M., Fraisse, A. A., Franceschi, E., Frejsel, A., Galeotta, S., Galli, S., Ganga, K., Gauthier, C., Gerbino, M., Ghosh, T., Giard, M., Giraud-Héraud, Y., Giusarma, E., Gjerløw, E., González-Nuevo, J., Górski, K. M., Gratton, S., Gregorio, A., Gruppuso, A., Gudmundsson, J. E., Hamann, J., Hansen, F. K., Hanson, D., Harrison, D. L., Helou, G., Henrot-Versillé, S., Hernández-Monteagudo, C., Herranz,

D., Hildebrandt, S. R., Hivon, E., Hobson, M., Holmes, W. A., Hornstrup, A., Hovest, W., Huang, Z., Huffenberger, K. M., Hurier, G., Jaffe, A. H., Jaffe, T. R., Jones, W. C., Juvela, M., Keihänen, E., Keskitalo, R., Kisner, T. S., Kneissl, R., Knoche, J., Knox, L., Kunz, M., Kurki-Suonio, H., Lagache, G., Lähteenmäki, A., Lamarre, J.-M., Lasenby, A., Lattanzi, M., Lawrence, C. R., Leahy, J. P., Leonardi, R., Lesgourgues, J., Levrier, F., Lewis, A., Liguori, M., Lilje, P. B., Linden-Vørnle, M., López-Caniego, M., Lubin, P. M., Mac´ias-Pérez, J. F., Maggio, G., Maino, D., Mandolesi, N., Mangilli, A., Marchini, A., Maris, M., Martin, P. G., Martinelli, M., Mart´inez-González, E., Masi, S., Matarrese, S., McGehee, P., Meinhold, P. R., Melchiorri, A., Melin, J.-B., Mendes, L., Mennella, A., Migliaccio, M., Millea, M., Mitra, S., Miville-Deschênes, M.-A., Moneti, A., Montier, L., Morgante, G., Mortlock, D., Moss, A., Munshi, D., Murphy, J. A., Naselsky, P., Nati, F., Natoli, P., Netterfield, C. B., Nørgaard-Nielsen, H. U., Noviello, F., Novikov, D., Novikov, I., Oxborrow, C. A., Paci, F., Pagano, L., Pajot, F., Paladini, R., Paoletti, D., Partridge, B., Pasian, F., Patanchon, G., Pearson, T. J., Perdereau, O., Perotto, L., Perrotta, F., Pettorino, V., Piacentini, F., Piat, M., Pierpaoli, E., Pietrobon, D., Plaszczynski, S., Pointecouteau, E., Polenta, G., Popa, L., Pratt, G. W., Prézeau, G., Prunet, S., Puget, J.-L., Rachen, J. P., Reach, W. T., Rebolo, R., Reinecke, M., Remazeilles, M., Renault, C., Renzi, A., Ristorcelli, I., Rocha, G., Rosset, C., Rossetti, M., Roudier, G., Rouillé d´Orfeuil, B., Rowan-Robinson, M., Rubiño-Mart´in, J. A., Rusholme, B., Said, N., Salvatelli, V., Salvati, L., Sandri, M., Santos, D., Savelainen, M., Savini, G., Scott, D., Seiffert, M. D., Serra, P., Shellard, E. P. S., Spencer, L. D., Spinelli, M., Stolyarov, V., Stompor, R., Sudiwala, R., Sunyaev, R., Sutton, D., Suur-Uski, A.-S., Sygnet, J.-F., Tauber, J. A., Terenzi, L., Toffolatti, L., Tomasi, M., Tristram, M., Trombetti, T., Tucci, M., Tuovinen, J., Türler, M., Umana, G., Valenziano, L., Valiviita, J., Van Tent, F., Vielva, P., Villa, F., Wade, L. A., Wandelt, B. D., Wehus, I. K., White, M., White, S. D. M., Wilkinson, A., Yvon, D., Zacchei, A., and Zonca, A. Planck 2015 results - xiii. cosmological parameters. A&A, 594:A13, 2016.

[83] R. A. Edelson and J. H. Krolik. The discrete correlation function - A new method for analyzing unevenly sampled variability data. ApJ, 333:646–659, October 1988.

[84] D. R. S. Robertson, L. C. Gallo, A. Zoghbi, and A. C. Fabian. Searching for correlations in simultaneous X-ray and UV emission in the narrow-line Seyfert 1 galaxy 1H 0707-495. MNRAS, 453:3455–3460, November 2015.

[85] J. Tinbergen. Astronomical Polarimetry. August 2005.

[86] D. S. Berry, T. M. Gledhill, J. S. Greaves, and T. Jenness. POLPACK—An Imaging Polarimetry Reduction Package. In A. Adamson, C. Aspin, C. Davis, and T. Fujiyoshi, editors, Astronomical Polarimetry: Current Status and Future Directions, volume 343 of Astron. Soc. Pac. Conf. Ser., page 71, December 2005.

[87] D. S. Berry and T. M. Gledhill. POLPACK: Imaging polarimetry reduction package. Astrophys. Source Code Lib., May 2014.

[88] O. G. King, D. Blinov, A. N. Ramaprakash, I. Myserlis, E. Angelakis, M. Baloković, R. Feiler, L. Fuhrmann, T. Hovatta, P. Khodade, A. Kougentakis, N. Kylafis, A. Kus, D. Modi, E. Paleologou, G. Panopoulou, I. Papadakis, I. Papamastorakis, G. Paterakis, V. Pavlidou, B. Pazderska, E. Pazderski, T. J. Pearson, C. Rajarshi, A. C. S. Readhead, P. Reig, A. Steiakaki, K. Tassis, and J. A. Zensus. The RoboPol pipeline and control system. MNRAS, 442:1706–1717, August 2014.

[89] G. Panopoulou, K. Tassis, D. Blinov, V. Pavlidou, O. G. King, E. Paleologou, A. Ramaprakash, E. Angelakis, M. Baloković, H. K. Das, R. Feiler, T. Hovatta, P. Khodade, S. Kiehlmann, A. Kus, N. Kylafis, I. Liodakis, A. Mahabal, D. Modi, I. Myserlis, I. Papadakis, I. Papamastorakis, B. Pazderska, E. Pazderski, T. J. Pearson, C. Rajarshi, A. C. S. Readhead, P. Reig, and J. A. Zensus. Optical polarization map of the Polaris Flare with RoboPol. MNRAS, 452:715–726, September 2015.

[90] R. Skalidis, G. V. Panopoulou, K. Tassis, V. Pavlidou, D. Blinov, I. Komis, and I. Liodakis. Local measurements of the mean interstellar polarization at high Galactic latitudes. A&A, 616:A52, August 2018.

[91] G. M. Cole. Developing a Polarimeter to Support the Epsilon Aurigae Campaign. Soc. Astron. Sci. Ann. Symp., 29:37–42, 2010.

[92] G. M. Cole. A Pellicle Autoguider for the DSS-7 Spectrograph. Soc. Astron. Sci. Ann. Symp., 26:153, May 2007.

[93] G. M. Cole. Automating a Telescope for Spectroscopy. Soc. Astron. Sci. Ann. Symp., 27:103, May 2008.

[94] G. M. Cole. A New Instrument Selector for Small Telescopes. In Am. Astron. Soc. Meet. Abs., volume 214, page 672, May 2009.

[95] G. Cole. A Spectropolarimeter Based On The SBIG Spectrometer. International Amateur-Professional Photoelectric Photometry Communications, 84:13, June 2001.

[96] G. M. Cole. Small Telescope Spectropolarimetry: Instruments and Observations. Soc. Astron. Sci. Ann. Symp., 35:37–47, May 2016.

[97] G. M. Cole and R. E. Stencel. Polarimetry of Epsilon Aurigae from Mid Eclipse to Third Contact. Soc. Astron. Sci. Ann. Symp., 30:103–108, May 2011.

[98] G. M. Cole. Polarimetry of epsilon Aurigae, From November 2009 to January 2012. J. Am. Assoc. Var. Star Obs., 40:787, June 2012.

[99] G. M. Cole. Long Term Broadband Polarimetry of Epsilon Aurigae and Field Stars. In Giants of Eclipse, volume 45, July 2013.

[100] T. M. Wolfe, R. Stencel, and G. Cole. Commissioning Results of a New Polarimeter: Denver University Small Telescope Polarimeter (DUSTPol). In K. N. Nagendra, S. Bagnulo, R. Centeno, and M. Jesús Mart´inez González, editors, Polarimetry, volume 305 of IAU Symposium, pages 200–206, October 2015.

[101] A. S. Friedman and G. M. Cole *in preparation*. The Array Photo Polarimeter. 2019.

[102] M. Uemura, K. S. Kawabata, M. Sasada, Y. Ikejiri, K. Sakimoto, R. Itoh, M. Yamanaka, T. Ohsugi, S. Sato, and M. Kino. Bayesian approach to find a long-term trend in erratic polarization variations observed in blazars. In 38th COSPAR Scientific Assembly, volume 38 of COSPAR Meeting, page 2, 2010.

[103] R. Falomo, E. Pian, and A. Treves. An optical view of BL Lacertae objects. A&A Rev., 22:73, September 2014.

[104] T. Hovatta, E. Lindfors, D. Blinov, V. Pavlidou, K. Nilsson, S. Kiehlmann, E. Angelakis, V. Fallah Ramazani, I. Liodakis, I. Myserlis, G. V. Panopoulou, and T. Pursimo. Optical polarization of high-energy BL Lacertae objects. A&A, 596:A78, December 2016.

[105] M. Kokubo. Constraints on the optical polarization source in the luminous non-blazar quasar 3C 323.1 (PG 1545+210) from the photometric and polarimetric variability. MNRAS, 467:3723–3736, May 2017.

[106] M. I. Carnerero, C. M. Raiteri, M. Villata, J. A. Acosta-Pulido, V. M. Larionov, P. S. Smith, F. D'Ammando, I. Agudo, M. J. Arévalo, R. Bachev, J. Barnes, S. Boeva, V. Bozhilov, D. Carosati, C. Casadio, W. P. Chen, G. Damljanovic, E. Eswaraiah, E. Forné, G. Gantchev, J. L. Gómez, P. A. González-Morales, A. B. Griñón-Mar´in, T. S. Grishina, M. Holden, S. Ibryamov, M. D. Joner, B. Jordan, S. G. Jorstad, M. Joshi, E. N. Kopatskaya, E. Koptelova, O. M. Kurtanidze, S. O. Kurtanidze, E. G. Larionova, L. V. Larionova, G. Latev, C. Lázaro, R. Ligustri, H. C. Lin, A. P. Marscher, C. Mart´inez-Lombilla, B. McBreen, B. Mihov, S. N. Molina, J. W. Moody, D. A. Morozova, M. G. Nikolashvili, K. Nilsson, E. Ovcharov, C. Pace, N. Panwar, A. Pastor Yabar, R. L. Pearson, F. Pinna, C. Protasio, N. Rizzi, F. J. Redondo-Lorenzo, G. Rodr´iguez-Coira, J. A. Ros, A. C. Sadun, S. S. Savchenko, E. Semkov, L. Slavcheva-Mihova, N. Smith, A. Strigachev, Y. V. Troitskaya, I. S. Troitsky, A. A. Vasilyev, and O. Vince. Dissecting the long-term emission behaviour of the BL Lac object Mrk 421. MNRAS, 472:3789–3804, December 2017.

[107] R. L. Moore, J. R. P. Angel, R. Duerr, M. J. Lebofsky, W. Z. Wisniewski, G. H. Rieke, D. J. Axon, J. Bailey, J. M. Hough, and J. T. McGraw. The noise of BL Lacertae. ApJ, 260:415–436, September 1982.

[108] Y. Ikejiri, M. Uemura, M. Sasada, R. Ito, M. Yamanaka, K. Sakimoto, A. Arai, Y. Fukazawa, T. Ohsugi, K. S. Kawabata, M. Yoshida, S. Sato, and M. Kino. Photopolarimetric Monitoring of Blazars in the Optical and Near-Infrared Bands with the Kanata Telescope. I. Correlations between Flux, Color, and Polarization. PASJ, 63:639–675, June 2011.

[109] Y.-H. Zhang, F.-Y. Bian, J.-Z. Li, and R.-C. Shang. Optical observations of BL Lacertae in 2004-2005. MNRAS, 432:1189–1195, June 2013.

[110] Y. H. Zhang, L. Xu, and J. C. Li. Search for hard lags with intra-night optical observations of BL Lacertae. Astronomische Nachrichten, 337:286, March 2016.

[111] C. D. Impey, V. Bychkov, S. Tapia, Y. Gnedin, and S. Pustilnik. Rapid Polarization Variability in the BL Lacertae Object S5 0716+714. AJ, 119:1542–1561, April 2000.

[112] R. Nesci, E. Massaro, and F. Montagni. Intraday Optical Variability of S5 0716+714. PASA, 19:143–146, 2002.

[113] M. Sasada, M. Uemura, A. Arai, Y. Fukazawa, K. S. Kawabata, T. Ohsugi, T. Yamashita, M. Isogai, S. Sato, and M. Kino. Detection of Polarimetric Variations Associated with the Shortest Time-Scale Variability in S5 0716+714. PASJ, 60:L37–L41, December 2008.

[114] V. M. Larionov, S. G. Jorstad, A. P. Marscher, D. A. Morozova, D. A. Blinov, V. A. Hagen-Thorn, T. S. Konstantinova, E. N. Kopatskaya, L. V. Larionova, E. G. Larionova, and I. S. Troitsky. The Outburst of the Blazar S5 0716+71 in 2011 October: Shock in a Helical Jet. ApJ, 768:40, May 2013.

[115] S. Chandra, H. Zhang, P. Kushwaha, K. P. Singh, M. Bottcher, N. Kaur, and K. S. Baliyan. Multi-wavelength Study of Flaring Activity in BL Lac Object S5 0716+714 during the 2015 Outburst. ApJ, 809:130, August 2015.

[116] G. Bhatta, A. Goyal, M. Ostrowski, Ł. Stawarz, H. Akitaya, A. A. Arkharov, R. Bachev, E. Ben´itez, G. A. Borman, D. Carosati, A. D. Cason, G. Damljanovic, S. Dhalla, A. Frasca, S.-M. Hu, R. Itoh, S. Jorstad, D. Jableka, K. S. Kawabata, S. A. Klimanov, O. Kurtanidze, V. M. Larionov, D. Laurence, G. Leto, A. Markowitz, A. P. Marscher, J. W. Moody, Y. Moritani, J. M. Ohlert, A. Di Paola, C. M. Raiteri, N. Rizzi, A. C. Sadun, M. Sasada, S. Sergeev, A. Strigachev, K. Takaki, I. S. Troitsky, T. Ui, M. Villata, O. Vince, J. R. Webb, M. Yoshida, S. Zola, and D. Hiriart. Discovery of a Highly Polarized Optical Microflare in Blazar S5 0716+714 during the 2014 WEBT Campaign. ApJ, 809:L27, August 2015.

[117] G. Bhatta, Ł. Stawarz, M. Ostrowski, A. Markowitz, H. Akitaya, A. A. Arkharov, R. Bachev, E. Ben´itez, G. A. Borman, D. Carosati, A. D. Cason, R. Chanishvili, G. Damljanovic, S. Dhalla, A. Frasca, D. Hiriart, S.-M. Hu, R. Itoh, D. Jableka, S. Jorstad, M. D. Jovanovic, K. S. Kawabata, S. A. Klimanov, O. Kurtanidze, V. M. Larionov, D. Laurence, G. Leto, A. P. Marscher, J. W. Moody, Y. Moritani, J. M. Ohlert, A. Di Paola, C. M. Raiteri, N. Rizzi, A. C. Sadun, M. Sasada, S. Sergeev, A. Strigachev, K. Takaki, I. S. Troitsky, T. Ui, M. Villata, O. Vince, J. R. Webb, M. Yoshida, and S. Zola. Multifrequency Photo-polarimetric WEBT Observation Campaign on the Blazar S5 0716+714: Source Microvariability and Search for Characteristic Timescales. ApJ, 831:92, November 2016.

[118] V. T. Doroshenko and N. N. Kiselev. Polarization and brightness of the blazar S5 0716+714 in 1991-2004. Astron. Lett., 43:365–387, June 2017.

[119] Y.-H. Yuan, J.-h. Fan, J. Tao, B.-C. Qian, D. Costantin, H.-B. Xiao, Z.-Y. Pei, and C. Lin. Optical monitoring of BL Lac object S5 0716+714 and FSRQ 3C 273 from 2000 to 2014. A&A, 605:A43, September 2017.

[120] J. H. Hough. Polarimetry Techniques at Optical and Infrared Wavelengths. In A. Adamson, C. Aspin, C. Davis, and T. Fujiyoshi, editors, Astronomical Polarimetry: Current Status and Future Directions, volume 343 of Astron. Soc. Pac. Conf. Ser., page 3, December 2005.

[121] J. Hough. Polarimetry: a powerful diagnostic tool in astronomy. Astron. Geophys., 47(3):3.31–3.35, June 2006.

[122] J. H. Hough. New opportunities for astronomical polarimetry. J. Quant. Spec. Radiat. Transf., 106:122–132, July 2007.

[123] J Hough. High sensitivity polarimetry: techniques and applications. Polarimetric Detection, Characterization and Remote Sensing, pages 177–204, 2011.

[124] S. Bagnulo, M. Landolfi, J. D. Landstreet, E. Landi Degl'Innocenti, L. Fossati, and M. Sterzik. Stellar Spectropolarimetry with Retarder Waveplate and Beam Splitter Devices. PASP, 121:993, September 2009.

[125] H. Canovas, M. Rodenhuis, S. V. Jeffers, M. Min, and C. U. Keller. Data-reduction techniques for high-contrast imaging polarimetry. Applications to ExPo. A&A, 531:A102, July 2011.

[126] A. J. Weitenbeck. Stars with ISM Polarization Observed with HPOL. III. Acta Astron., 58:433, December 2008.

[127] M. R. Meade, B. A. Whitney, B. L. Babler, K. H. Nordsieck, K. S. Bjorkman, and J. P. Wisniewski. HPOL: World's largest database of optical spectropolarimetry. In J. L. Hoffman, J. Bjorkman, and B. Whitney, editors, American Institute of Physics Conference Series, volume 1429 of American Institute of Physics Conference Series, pages 226–229, May 2012.

[128] R. Siebenmorgen, N. V. Voshchinnikov, S. Bagnulo, N. L. J. Cox, J. Cami, and C. Peest. Large Interstellar Polarisation Survey. II. UV/optical study of cloud-to-cloud variations of dust in the diffuse ISM. A&A, 611:A5, March 2018.

[129] S. Bagnulo, N. L. J. Cox, A. Cikota, R. Siebenmorgen, N. V. Voshchinnikov, F. Patat, K. T. Smith, J. V. Smoker, S. Taubenberger, L. Kaper, J. Cami, and LIPS Collaboration. Large Interstellar Polarisation Survey (LIPS). I. FORS2 spectropolarimetry in the Southern Hemisphere. A&A, 608:A146, December 2017.

[130] Fabian Kislat. Constraints on lorentz invariance violation from optical polarimetry of astrophysical objects. Symmetry, 10(11), 2018.

[131] E. Angelakis, T. Hovatta, D. Blinov, V. Pavlidou, S. Kiehlmann, I. Myserlis, M. Böttcher, P. Mao, G. V. Panopoulou, I. Liodakis, O. G. King, M. Baloković, A. Kus, N. Kylafis, A. Mahabal, A. Marecki, E. Paleologou, I. Papadakis, I. Papamastorakis, E. Pazderski, T. J. Pearson, S. Prabhudesai, A. N. Ramaprakash, A. C. S. Readhead, P. Reig, K. Tassis, M. Urry, and J. A. Zensus. RoboPol: the optical polarization of gamma-ray-loud and gamma-ray-quiet blazars. MNRAS, 463:3365–3380, December 2016.

[132] D. Hutsemékers, P. Hall, and D. Sluse. Optical linear polarization measurements of quasars obtained with the 3.6 m telescope at the La Silla Observatory. A&A, 606:A101, October 2017.

[133] D. Blinov, V. Pavlidou, I. Papadakis, S. Kiehlmann, G. Panopoulou, I. Liodakis, O. G. King, E. Angelakis, M. Baloković, H. Das, R. Feiler, L. Fuhrmann, T. Hovatta, P. Khodade, A. Kus, N. Kylafis, A. Mahabal, I. Myserlis, D. Modi, B. Pazderska, E. Pazderski, I. Papamastorakis, T. J. Pearson, C. Rajarshi, A. Ramaprakash, P. Reig, A. C. S. Readhead, K. Tassis, and J. A. Zensus. RoboPol: first season rotations of optical polarization plane in blazars. MNRAS, 453:1669–1683, October 2015.

[134] Antony Lewis and Anthony Challinor. Weak gravitational lensing of the CMB. Phys. Rep., 429(1):1–65, Jun 2006.

[135] W. Hu and T. Okamoto. Mass Reconstruction with Cosmic Microwave Background Polarization. ApJ, 574:566–574, August 2002.

[136] Kendrick M. Smith, Asantha Cooray, Sudeep Das, Olivier Doré, Duncan Hanson, Chris Hirata, Manoj Kaplinghat, Brian Keating, Marilena Loverde, Nathan Miller, Graça Rocha, Meir Shimon, and Oliver Zahn. Gravitational Lensing. In Scott Dodelson, Daniel Baumann, Asantha Cooray, Joanna Dunkley, Aurelien Fraisse, Mark G. Jackson, Alan Kogut, Lawrence Krauss, Matias Zaldarriaga, and Kendrick Smith, editors, American Institute of Physics Conference Series, volume 1141 of American Institute of Physics Conference Series, pages 121–178, Jun 2009.

[137] Stephen Osborne, Duncan Hanson, and Olivier Doré. Extragalactic foreground contamination in temperature-based cmb lens reconstruction. Journal of Cosmology and Astroparticle Physics, 2014, 10 2013.

[138] The Polarbear Collaboration. Measurement of the Cosmic Microwave Background Polarization Lensing Power Spectrum with the POLARBEAR experiment. Phys. Rev. Lett., 113:021301, Jul 2014.

[139] P. A. R. Ade, Z. Ahmed, R. W. Aikin, K. D. Alexander, D. Barkats, S. J. Benton, C. A. Bischoff, J. J. Bock, R. Bowens-Rubin, J. A. Brevik, I. Buder, E. Bullock, V. Buza, J. Connors, B. P. Crill, L. Duband, C. Dvorkin, J. P. Filippini, S. Fliescher, J. Grayson, M. Halpern, S. Harrison, S. R. Hildebrandt, G. C. Hilton, H. Hui, K. D. Irwin, J. Kang, K. S. Karkare, E. Karpel, J. P. Kaufman, B. G. Keating, S. Kefeli, S. A. Kernasovskiy, J. M. Kovac, C. L. Kuo, E. M. Leitch, M. Lueker, K. G. Megerian, T. Namikawa, C. B. Netterfield, H. T. Nguyen, R. O'Brient, R. W. Ogburn IV, A. Orlando, C. Pryke, S. Richter, R. Schwarz, C. D. Sheehy, Z. K. Staniszewski, B. Steinbach, R. V. Sudiwala, G. P. Teply, K. L. Thompson, J. E. Tolan, C. Tucker, A. D. Turner, A. G. Vieregg, A. C. Weber, D. V. Wiebe, J. Willmert, C. L. Wong, W. L. K. Wu, and K. W. Yoon and. Bicep2/KECK ARRAYVIII: MEASUREMENT OF GRAVITATIONAL LENSING FROM LARGE-SCALEB-MODE POLARIZATION. The Astrophysical Journal, 833(2):228, dec 2016.

[140] Blake D. Sherwin, Alexander van Engelen, Neelima Sehgal, Mathew Madhavacheril, Graeme E. Addison, Simone Aiola, Rupert Allison, Nicholas Battaglia, Daniel T. Becker, James A. Beall, J. Richard Bond, Erminia Calabrese, Rahul Datta, Mark J. Devlin, Rolando Dünner, Joanna Dunkley, Anna E. Fox, Patricio Gallardo, Mark Halpern, Matthew Hasselfield, Shawn Henderson, J. Colin Hill, Gene C. Hilton, Johannes Hubmayr, John P. Hughes, Adam D. Hincks, Renée Hlozek, Kevin M. Huffenberger, Brian Koopman, Arthur Kosowsky, Thibaut Louis, Lo¨ic Maurin, Jeff McMahon, Kavilan Moodley, Sigurd Naess, Federico Nati, Laura Newburgh, Michael D. Niemack, Lyman A. Page, Jonathan Sievers, David N. Spergel, Suzanne T. Staggs, Robert J. Thornton, Jeff Van Lanen, Eve Vavagiakis, and Edward J. Wollack. Two-season atacama cosmology telescope polarimeter lensing power spectrum. Phys. Rev. D, 95:123529, Jun 2017.

[141] Planck Collaboration VIII. Planck 2018 results. VIII. Gravitational lensing. arXiv e-prints, page arXiv:1807.06210, Jul 2018.

[142] W. L. K. Wu, L. M. Mocanu, P. A. R. Ade, A. J. Anderson, J. E. Austermann, J. S. Avva, J. A. Beall, A. N. Bender, B. A. Benson, F. Bianchini, L. E. Bleem, J. E. Carlstrom, C. L. Chang, H. C. Chiang, R. Citron, C. Corbett Moran, T. M. Crawford, A. T. Crites, T. de Haan, M. A. Dobbs, W. Everett, J. Gallicchio, E. M. George, A. Gilbert, N. Gupta, N. W. Halverson, N. Harrington, J. W. Henning, G. C. Hilton, G. P. Holder, W. L. Holzapfel, Z. Hou, J. D. Hrubes, N. Huang, J. Hubmayr, K. D. Irwin, L. Knox, A. T. Lee, D. Li, A. Lowitz, A. Manzotti, J. J. McMahon, S. S. Meyer, M. Millea, J. Montgomery, A. Nadolski, T. Natoli, J. P. Nibarger, G. I. Noble, V. Novosad, Y. Omori, S. Padin, S. Patil, C. Pryke, C. L. Reichardt, J. E. Ruhl, B. R. Saliwanchik, J. T. Sayre, K. K. Schaffer, C. Sievers, G. Simard, G. Smecher, A. A. Stark, K. T. Story, C. Tucker, K. Vanderlinde, T. Veach, J. D. Vieira, G. Wang, N. Whitehorn, and V. Yefremenko. A measurement of the cosmic microwave background lensing potential and power spectrum from 500 deg2 of SPTpol temperature and polarization data. The Astrophysical Journal, 884(1):70, oct 2019.

[143] T. Namikawa, Y. Chinone, H. Miyatake, M. Oguri, R. Takahashi, A. Kusaka, N. Katayama, S. Adachi, M. Aguilar, H. Aihara, A. Ali, R. Armstrong, K. Arnold, C. Baccigalupi, D. Barron, D. Beck, S. Beckman, F. Bianchini, D. Boettger, J. Borrill, K. Cheung, L. Corbett, K. T. Crowley, H. El Bouhargani, T. Elleflot, J. Errard, G. Fabbian, C. Feng, N. Galitzki, N. Goeckner-Wald, J. Groh, T. Hamada, M. Hasegawa, M. Hazumi, C. A. Hill, L. Howe, O. Jeong, D. Kaneko, B. Keating, A. T. Lee, D. Leon, E. Linder, L. N. Lowry, A. Mangu, F. Matsuda, Y. Minami, S. Miyazaki, H. Murayama, M. Navaroli, H. Nishino, A. J. Nishizawa, A. T. P. Pham, D. Poletti, G. Puglisi, C. L. Reichardt, B. D. Sherwin, M. Silva-Feaver, P. Siritanasak, J. S. Speagle, R. Stompor, A. Suzuki, P. J. Tait, O. Tajima, M. Takada, S. Takakura, S. Takatori, D. Tanabe, M. Tanaka, G. P. Teply, C. Tsai, C. Vergés, B. Westbrook, and Y. Zhou and. Evidence for the cross-correlation between cosmic microwave background polarization lensing from polarbear and cosmic shear from subaru hyper suprime-cam. The Astrophysical Journal, 882(1):62, sep 2019.

[144] The Polarbear Collaboration. Cross-correlation of POLARBEAR CMB Polarization Lensing with High-z Sub-mm Herschel-ATLAS galaxies. 2019.

[145] F. Bianchini, P. Bielewicz, A. Lapi, J. Gonzalez-Nuevo, C. Baccigalupi, G. de Zotti, L. Danese, N. Bourne, A. Cooray, L. Dunne, S. Dye, S. Eales, R. Ivison, S. Maddox, M. Negrello, D. Scott, M. W. L. Smith, and E. Valiante. CROSS-CORRELATION BETWEEN THE CMB LENSING POTENTIAL MEASURED BYPLANCKAND HIGH-zSUBMILLIMETER GALAXIES DETECTED BY THEHERSCHEL-ATLAS SURVEY. The Astrophysical Journal, 802(1):64, mar 2015.

[146] A. Manzotti, K. T. Story, W. L. K. Wu, J. E. Austermann, J. A. Beall, A. N. Bender, B. A. Benson, L. E. Bleem, J. J. Bock, J. E. Carlstrom, C. L. Chang, H. C. Chiang, H-M. Cho, R. Citron, A. Conley, T. M. Crawford, A. T. Crites, T. de Haan, M. A. Dobbs, S. Dodelson, W. Everett, J. Gallicchio, E. M. George, A. Gilbert, N. W. Halverson, N. Harrington, J. W. Henning, G. C. Hilton, G. P. Holder, W. L. Holzapfel, S. Hoover, Z. Hou, J. D. Hrubes, N. Huang, J. Hubmayr, K. D. Irwin, R. Keisler, L. Knox, A. T. Lee, E. M. Leitch, D. Li, J. J. McMahon, S. S. Meyer, L. M. Mocanu, T. Natoli, J. P. Nibarger, V. Novosad, S. Padin, C. Pryke, C. L. Reichardt, J. E. Ruhl, B. R. Saliwanchik, J. T. Sayre, K. K. Schaffer, G. Smecher, A. A. Stark, K. Vanderlinde, J. D. Vieira, M. P. Viero, G. Wang, N. Whitehorn, V. Yefremenko, and M. Zemcov. CMB PolarizationB-mode delensing with SPTpol andHerschel. The Astrophysical Journal, 846(1):45, aug 2017.

[147] Blake D. Sherwin and Marcel Schmittfull. Delensing the cmb with the cosmic infrared background. Phys. Rev. D, 92:043005, Aug 2015.

[148] Julien Carron, Antony Lewis, and Anthony Challinor. Internal delensing of planck CMB temperature and polarization. Journal of Cosmology and Astroparticle Physics, 2017(05):035–035, may 2017.

[149] The Polarbear Collaboration. Internal delensing of cosmic microwave background polarization B-modes with the POLARBEAR experiment. arXiv e-prints, page arXiv:1909.13832, Sep 2019.

[150] Julien Carron. Optimal constraints on primordial gravitational waves from the lensed cmb. Phys. Rev. D, 99:043518, Feb 2019.

[151] K. Arnold, P. A. R. Ade, A. E. Anthony, D. Barron, D. Boettger, J. Borrill, S. Chapman, Y. Chinone, M. A. Dobbs, J. Errard, G. Fabbian, D. Flanigan, G. Fuller, A. Ghribi, W. Grainger, N. Halverson, M. Hasegawa, K. Hattori, M. Hazumi, W. L. Holzapfel, J. Howard, P. Hyland, A. Jaffe, B. Keating, Z. Kermish, T. Kisner, M. Le Jeune, A. T. Lee, E. Linder, M. Lungu, F. Matsuda, T. Matsumura, N. J. Miller, X. Meng, H. Morii, S. Moyerman, M. J. Myers, H. Nishino, H. Paar, E. Quealy, C. Reichardt, P. L. Richards, C. Ross, A. Shimizu, C. Shimmin, M. Shimon, M. Sholl, P. Siritanasak, H. Spieler, N. Stebor, B. Steinbach, R. Stompor, A. Suzuki, T. Tomaru, C. Tucker, and O. Zahn. The bolometric focal plane array of the POLARBEAR CMB experiment. In Society of Photo-Optical Instrumentation Engineers (SPIE) Conference Series, volume

8452 of Society of Photo-Optical Instrumentation Engineers (SPIE) Conference Series, September 2012.

[152] Z. D. Kermish, P. Ade, A. Anthony, K. Arnold, D. Barron, D. Boettger, J. Borrill, S. Chapman, Y. Chinone, M. A. Dobbs, J. Errard, G. Fabbian, D. Flanigan, G. Fuller, A. Ghribi, W. Grainger, N. Halverson, M. Hasegawa, K. Hattori, M. Hazumi, W. L. Holzapfel, J. Howard, P. Hyland, A. Jaffe, B. Keating, T. Kisner, A. T. Lee, M. Le Jeune, E. Linder, M. Lungu, F. Matsuda, T. Matsumura, X. Meng, N. J. Miller, H. Morii, S. Moyerman, M. J. Myers, H. Nishino, H. Paar, E. Quealy, C. L. Reichardt, P. L. Richards, C. Ross, A. Shimizu, M. Shimon, C. Shimmin, M. Sholl, P. Siritanasak, H. Spieler, N. Stebor, B. Steinbach, R. Stompor, A. Suzuki, T. Tomaru, C. Tucker, and O. Zahn. The POLARBEAR experiment. In Society of Photo-Optical Instrumentation Engineers (SPIE) Conference Series, volume 8452 of Society of Photo-Optical Instrumentation Engineers (SPIE) Conference Series, September 2012.

[153] The POLARBEAR Collaboration. A Measurement of the Cosmic Microwave Background B-Mode Polarization Power Spectrum at Sub-Degree Scales from 2 years of POLARBEAR Data. Astrophys. J., 848(2):121, 2017.

[154] Planck Collaboration XIII. Planck 2015 results - xiii. cosmological parameters. A&A, 594:A13, 2016.

[155] Wayne Hu and Takemi Okamoto. Mass reconstruction with cosmic microwave background polarization. The Astrophysical Journal, 574(2):566–574, aug 2002.

[156] D. Hanson, A. Challinor, G. Efstathiou, and P. Bielewicz. CMB temperature lensing power reconstruction. Phys. Rev. D, 83(4):043005, February 2011.

[157] T. Namikawa, D. Hanson, and R. Takahashi. Bias-hardened CMB lensing. MNRAS, 431:609–620, May 2013.

[158] Asantha Cooray, Marc Kamionkowski, and Robert Caldwell. Cosmic shear of the microwave background: The curl diagnostic. Physical Review D, 71, 02 2005.

[159] Planck Collaboration IX. Planck 2015 results. IX. Diffuse component separation: CMB maps. A&A, 594:A9, September 2016.

[160] Planck Collaboration X. Planck 2015 results. X. Diffuse component separation: Foreground maps. A&A, 594:A10, September 2016.

[161] N. Krachmalnicoff, E. Carretti, C. Baccigalupi, G. Bernardi, S. Brown, B. M. Gaensler, M. Haverkorn, M. Kesteven, F. Perrotta, S. Poppi, and L. Staveley-Smith. S-PASS view of polarized Galactic synchrotron at 2.3 GHz as a contaminant to CMB observations. A&A, 618:A166, October 2018.

[162] Planck Collaboration XI. Planck 2018 results. XI. Polarized dust foregrounds. arXiv e-prints, page arXiv:1801.04945, Jan 2018.

[163] Planck Collaboration, N. Aghanim, Y. Akrami, M. Ashdown, J. Aumont, C. Baccigalupi, M. Ballardini, A. J. Banday, R. B. Barreiro, N. Bartolo, S. Basak, R. Battye, K. Benabed, J.-P. Bernard, M. Bersanelli, P. Bielewicz, J. J. Bock, J. R. Bond, J. Borrill, F. R. Bouchet, F. Boulanger, M. Bucher, C. Burigana, R. C. Butler, E. Calabrese, J.-F. Cardoso, J. Carron, A. Challinor, H. C. Chiang, J. Chluba, L. P. L. Colombo, C. Combet, D. Contreras, B. P. Crill, F. Cuttaia, P. de Bernardis, G. de Zotti, J. Delabrouille, J.-M. Delouis, E. Di Valentino, J. M. Diego, O. Doré, M. Douspis, A. Ducout, X. Dupac, S. Dusini, G. Efstathiou, F. Elsner, T. A. Enßlin, H. K. Eriksen, Y. Fantaye, M. Farhang, J. Fergusson, R. Fernandez-Cobos, F. Finelli, F. Forastieri, M. Frailis, E. Franceschi, A. Frolov, S. Galeotta, S. Galli, K. Ganga, R. T. Génova-Santos, M. Gerbino, T. Ghosh, J. González-Nuevo, K. M. Górski, S. Gratton, A. Gruppuso, J. E. Gudmundsson, J. Hamann, W. Handley, D. Herranz, E. Hivon, Z. Huang, A. H. Jaffe, W. C. Jones, A. Karakci, E. Keihänen, R. Keskitalo, K. Kiiveri, J. Kim, T. S. Kisner, L. Knox, N. Krachmalnicoff, M. Kunz, H. Kurki-Suonio, G. Lagache, J.-M. Lamarre, A. Lasenby, M. Lattanzi, C. R. Lawrence, M. Le Jeune, P. Lemos, J. Lesgourgues, F. Levrier, A. Lewis, M. Liguori, P. B. Lilje, M. Lilley, V. Lindholm, M. López-Caniego, P. M. Lubin, Y.-Z. Ma, J. F. Mac´ias-Pérez, G. Maggio, D. Maino, N. Mandolesi, A. Mangilli, A. Marcos-Caballero, M. Maris, P. G. Martin, M. Martinelli, E. Mart´inez-González, S. Matarrese, N. Mauri, J. D. McEwen, P. R. Meinhold, A. Melchiorri, A. Mennella, M. Migliaccio, M. Millea, S. Mitra, M.-A. Miville-Deschênes, D. Molinari, L. Montier, G. Morgante, A. Moss, P. Natoli, H. U. Nørgaard-Nielsen, L. Pagano, D. Paoletti, B. Partridge, G. Patanchon, H. V. Peiris, F. Perrotta, V. Pettorino, F. Piacentini, L. Polastri, G. Polenta, J.-L. Puget, J. P. Rachen, M. Reinecke, M. Remazeilles, A. Renzi, G. Rocha, C. Rosset, G. Roudier, J. A. Rubiño-Mart´in, B. Ruiz-Granados, L. Salvati, M. Sandri, M. Savelainen, D. Scott, E. P. S. Shellard, C. Sirignano, G. Sirri, L. D. Spencer, R. Sunyaev, A.-S. Suur-Uski, J. A. Tauber, D. Tavagnacco, M. Tenti, L. Toffolatti, M. Tomasi, T. Trombetti, L. Valenziano, J. Valiviita, B. Van Tent, L. Vibert, P. Vielva, F. Villa, N. Vittorio, B. D. Wandelt, I. K. Wehus, M. White, S. D. M. White, A. Zacchei, and A. Zonca. Planck 2018 results. VI. Cosmological parameters. ArXiv e-prints, July 2018.

[164] B. P. Abbott, R. Abbott, T. D. Abbott, M. R. Abernathy, F. Acernese, K. Ackley, C. Adams, T. Adams, P. Addesso, R. X. Adhikari, V. B. Adya, C. Affeldt, M. Agathos, K. Agatsuma, N. Aggarwal, O. D. Aguiar, L. Aiello, A. Ain, P. Ajith, B. Allen, A. Allocca, P. A. Altin, A. Ananyeva, S. B. Anderson, W. G. Anderson, S. Appert, K. Arai, M. C. Araya, J. S. Areeda, N. Arnaud, K. G. Arun, S. Ascenzi, G. Ashton, M. Ast, S. M. Aston, P. Astone, P. Aufmuth, C. Aulbert, A. Avila-Alvarez, S. Babak, P. Bacon, M. K. M. Bader, P. T. Baker, F. Baldaccini, G. Ballardin, S. W. Ballmer, J. C. Barayoga, S. E. Barclay, B. C. Barish, D. Barker, F. Barone, B. Barr, L. Barsotti, M. Barsuglia, D. Barta, J. Bartlett, I. Bartos, R. Bassiri, A. Basti, J. C. Batch, C. Baune, V. Bavigadda, M. Bazzan, C. Beer, M. Bejger, I. Belahcene, M. Belgin, A. S. Bell, B. K. Berger, G. Bergmann, C. P. L. Berry, D. Bersanetti, A. Bertolini, J. Betzwieser, S. Bhagwat, R. Bhandare, I. A. Bilenko, G. Billingsley, C. R. Billman, J. Birch, R. Birney, O. Birnholtz, S. Biscans, A. S. Biscoveanu, A. Bisht, M. Bitossi, C. Biwer, M. A. Bizouard, J. K. Blackburn, J. Blackman, C. D. Blair, D. G. Blair, R. M.

Blair, S. Bloemen, O. Bock, M. Boer, G. Bogaert, A. Bohe, F. Bondu, R. Bonnand, B. A. Boom, R. Bork, V. Boschi, S. Bose, Y. Bouffanais, A. Bozzi, C. Bradaschia, P. R. Brady, V. B. Braginsky, M. Branchesi, J. E. Brau, T. Briant, A. Brillet, M. Brinkmann, V. Brisson, P. Brockill, J. E. Broida, A. F. Brooks, D. A. Brown, D. D. Brown, N. M. Brown, S. Brunett, C. C. Buchanan, A. Buikema, T. Bulik, H. J. Bulten, A. Buonanno, D. Buskulic, C. Buy, R. L. Byer, M. Cabero, L. Cadonati, G. Cagnoli, C. Cahillane, J. Calderón Bustillo, T. A. Callister, E. Calloni, J. B. Camp, W. Campbell, M. Canepa, K. C. Cannon, H. Cao, J. Cao, C. D. Capano, E. Capocasa, F. Carbognani, S. Caride, J. Casanueva Diaz, C. Casentini, S. Caudill, M. Cavaglià, F. Cavalier, R. Cavalieri, G. Cella, C. B. Cepeda, L. Cerboni Baiardi, G. Cerretani, E. Cesarini, S. J. Chamberlin, M. Chan, S. Chao, P. Charlton, E. Chassande-Mottin, B. D. Cheeseboro, H. Y. Chen, Y. Chen, H.-P. Cheng, A. Chincarini, A. Chiummo, T. Chmiel, H. S. Cho, M. Cho, J. H. Chow, N. Christensen, Q. Chu, A. J. K. Chua, S. Chua, S. Chung, G. Ciani, F. Clara, J. A. Clark, F. Cleva, C. Cocchieri, E. Coccia, P.-F. Cohadon, A. Colla, C. G. Collette, L. Cominsky, M. Constancio, L. Conti, S. J. Cooper, T. R. Corbitt, N. Cornish, A. Corsi, S. Cortese, C. A. Costa, E. Coughlin, M. W. Coughlin, S. B. Coughlin, J.-P. Coulon, S. T. Countryman, P. Couvares, P. B. Covas, E. E. Cowan, D. M. Coward, M. J. Cowart, D. C. Coyne, R. Coyne, J. D. E. Creighton, T. D. Creighton, J. Cripe, S. G. Crowder, T. J. Cullen, A. Cumming, L. Cunningham, E. Cuoco, T. Dal Canton, S. L. Danilishin, S. D'Antonio, K. Danzmann, A. Dasgupta, C. F. Da Silva Costa, V. Dattilo, I. Dave, M. Davier, G. S. Davies, D. Davis, E. J. Daw, B. Day, R. Day, S. De, D. DeBra, G. Debreczeni, J. Degallaix, M. De Laurentis, S. Deléglise, W. Del Pozzo, T. Denker, T. Dent, V. Dergachev, R. De Rosa, R. T. DeRosa, R. DeSalvo, J. Devenson, R. C. Devine, S. Dhurandhar, M. C. D´iaz, L. Di Fiore, M. Di Giovanni, T. Di Girolamo, A. Di Lieto, S. Di Pace, I. Di Palma, A. Di Virgilio, Z. Doctor, V. Dolique, F. Donovan, K. L. Dooley, S. Doravari, I. Dorrington, R. Douglas, M. Dovale Álvarez, T. P. Downes, M. Drago, R. W. P. Drever, J. C. Driggers, Z. Du, M. Ducrot, S. E. Dwyer, T. B. Edo, M. C. Edwards, A. Effler, H.-B. Eggenstein, P. Ehrens, J. Eichholz, S. S. Eikenberry, R. C. Essick, Z. Etienne, T. Etzel, M. Evans, T. M. Evans, R. Everett, M. Factourovich, V. Fafone, H. Fair, S. Fairhurst, X. Fan, S. Farinon, B. Farr, W. M. Farr, E. J. Fauchon-Jones, M. Favata, M. Fays, H. Fehrmann, M. M. Fejer, A. Fernández Galiana, I. Ferrante, E. C. Ferreira, F. Ferrini, F. Fidecaro, I. Fiori, D. Fiorucci, R. P. Fisher, R. Flaminio, M. Fletcher, H. Fong, S. S. Forsyth, J.-D. Fournier, S. Frasca, F. Frasconi, Z. Frei, A. Freise, R. Frey, V. Frey, E. M. Fries, P. Fritschel, V. V. Frolov, P. Fulda, M. Fyffe, H. Gabbard, B. U. Gadre, S. M. Gaebel, J. R. Gair, L. Gammaitoni, S. G. Gaonkar, F. Garufi, G. Gaur, V. Gayathri, N. Gehrels, G. Gemme, E. Genin, A. Gennai, J. George, L. Gergely, V. Germain, S. Ghonge, Abhirup Ghosh, Archisman Ghosh, S. Ghosh, J. A. Giaime, K. D. Giardina, A. Giazotto, K. Gill, A. Glaefke, E. Goetz, R. Goetz, L. Gondan, G. González, J. M. Gonzalez Castro, A. Gopakumar, M. L. Gorodetsky, S. E. Gossan, M. Gosselin, R. Gouaty, A. Grado, C. Graef, M. Granata, A. Grant, S. Gras, C. Gray, G. Greco, A. C. Green, P. Groot, H. Grote, S. Grunewald, G. M. Guidi, X. Guo, A. Gupta, M. K. Gupta, K. E. Gushwa, E. K. Gustafson, R. Gustafson, J. J. Hacker, B. R. Hall, E. D. Hall, G. Hammond, M. Haney, M. M. Hanke, J. Hanks, C. Hanna, M. D. Hannam, J. Hanson, T. Hardwick, J. Harms, G. M. Harry, I. W. Harry, M. J. Hart, M. T. Hartman, C.-J. Haster, K. Haughian, J. Healy,

A. Heidmann, M. C. Heintze, H. Heitmann, P. Hello, G. Hemming, M. Hendry, I. S. Heng, J. Hennig, J. Henry, A. W. Heptonstall, M. Heurs, S. Hild, D. Hoak, D. Hofman, K. Holt, D. E. Holz, P. Hopkins, J. Hough, E. A. Houston, E. J. Howell, Y. M. Hu, E. A. Huerta, D. Huet, B. Hughey, S. Husa, S. H. Huttner, T. Huynh-Dinh, N. Indik, D. R. Ingram, R. Inta, H. N. Isa, J.-M. Isac, M. Isi, T. Isogai, B. R. Iyer, K. Izumi, T. Jacqmin, K. Jani, P. Jaranowski, S. Jawahar, F. Jiménez-Forteza, W. W. Johnson, D. I. Jones, R. Jones, R. J. G. Jonker, L. Ju, J. Junker, C. V. Kalaghatgi, V. Kalogera, S. Kandhasamy, G. Kang, J. B. Kanner, S. Karki, K. S. Karvinen, M. Kasprzack, E. Katsavounidis, W. Katzman, S. Kaufer, T. Kaur, K. Kawabe, F. Kéfélian, D. Keitel, D. B. Kelley, R. Kennedy, J. S. Key, F. Y. Khalili, I. Khan, S. Khan, Z. Khan, E. A. Khazanov, N. Kijbunchoo, Chunglee Kim, J. C. Kim, Whansun Kim, W. Kim, Y.-M. Kim, S. J. Kimbrell, E. J. King, P. J. King, R. Kirchhoff, J. S. Kissel, B. Klein, L. Kleybolte, S. Klimenko, P. Koch, S. M. Koehlenbeck, S. Koley, V. Kondrashov, A. Kontos, M. Korobko, W. Z. Korth, I. Kowalska, D. B. Kozak, C. Krämer, V. Kringel, A. Królak, G. Kuehn, P. Kumar, R. Kumar, L. Kuo, A. Kutynia, B. D. Lackey, M. Landry, R. N. Lang, J. Lange, B. Lantz, R. K. Lanza, A. Lartaux-Vollard, P. D. Lasky, M. Laxen, A. Lazzarini, C. Lazzaro, P. Leaci, S. Leavey, E. O. Lebigot, C. H. Lee, H. K. Lee, H. M. Lee, K. Lee, J. Lehmann, A. Lenon, M. Leonardi, J. R. Leong, N. Leroy, N. Letendre, Y. Levin, T. G. F. Li, A. Libson, T. B. Littenberg, J. Liu, N. A. Lockerbie, A. L. Lombardi, L. T. London, J. E. Lord, M. Lorenzini, V. Loriette, M. Lormand, G. Losurdo, J. D. Lough, G. Lovelace, H. Lück, A. P. Lundgren, R. Lynch, Y. Ma, S. Macfoy, B. Machenschalk, M. MacInnis, D. M. Macleod, F. Magaña Sandoval, E. Majorana, I. Maksimovic, V. Malvezzi, N. Man, V. Mandic, V. Mangano, G. L. Mansell, M. Manske, M. Mantovani, F. Marchesoni, F. Marion, S. Márka, Z. Márka, A. S. Markosyan, E. Maros, F. Martelli, L. Martellini, I. W. Martin, D. V. Martynov, K. Mason, A. Masserot, T. J. Massinger, M. Masso-Reid, S. Mastrogiovanni, A. Matas, F. Matichard, L. Matone, N. Mavalvala, N. Mazumder, R. McCarthy, D. E. McClelland, S. McCormick, C. McGrath, S. C. McGuire, G. McIntyre, J. McIver, D. J. McManus, T. McRae, S. T. McWilliams, D. Meacher, G. D. Meadors, J. Meidam, A. Melatos, G. Mendell, D. Mendoza-Gandara, R. A. Mercer, E. L. Merilh, M. Merzougui, S. Meshkov, C. Messenger, C. Messick, R. Metzdorff, P. M. Meyers, F. Mezzani, H. Miao, C. Michel, H. Middleton, E. E. Mikhailov, L. Milano, A. L. Miller, A. Miller, B. B. Miller, J. Miller, M. Millhouse, Y. Minenkov, J. Ming, S. Mirshekari, C. Mishra, S. Mitra, V. P. Mitrofanov, G. Mitselmakher, R. Mittleman, A. Moggi, M. Mohan, S. R. P. Mohapatra, M. Montani, B. C. Moore, C. J. Moore, D. Moraru, G. Moreno, S. R. Morriss, B. Mours, C. M. Mow-Lowry, G. Mueller, A. W. Muir, Arunava Mukherjee, D. Mukherjee, S. Mukherjee, N. Mukund, A. Mullavey, J. Munch, E. A. M. Muniz, P. G. Murray, A. Mytidis, K. Napier, I. Nardecchia, L. Naticchioni, G. Nelemans, T. J. N. Nelson, M. Neri, M. Nery, A. Neunzert, J. M. Newport, G. Newton, T. T. Nguyen, A. B. Nielsen, S. Nissanke, A. Nitz, A. Noack, F. Nocera, D. Nolting, M. E. N. Normandin, L. K. Nuttall, J. Oberling, E. Ochsner, E. Oelker, G. H. Ogin, J. J. Oh, S. H. Oh, F. Ohme, M. Oliver, P. Oppermann, Richard J. Oram, B. O'Reilly, R. O'Shaughnessy, D. J. Ottaway, H. Overmier, B. J. Owen, A. E. Pace, J. Page, A. Pai, S. A. Pai, J. R. Palamos, O. Palashov, C. Palomba, A. Pal-Singh, H. Pan, C. Pankow, F. Pannarale, B. C. Pant, F. Paoletti, A. Paoli, M. A. Papa, H. R. Paris,

W. Parker, D. Pascucci, A. Pasqualetti, R. Passaquieti, D. Passuello, B. Patricelli, B. L. Pearlstone, M. Pedraza, R. Pedurand, L. Pekowsky, A. Pele, S. Penn, C. J. Perez, A. Perreca, L. M. Perri, H. P. Pfeiffer, M. Phelps, O. J. Piccinni, M. Pichot, F. Piergiovanni, V. Pierro, G. Pillant, L. Pinard, I. M. Pinto, M. Pitkin, M. Poe, R. Poggiani, P. Popolizio, A. Post, J. Powell, J. Prasad, J. W. W. Pratt, V. Predoi, T. Prestegard, M. Prijatelj, M. Principe, S. Privitera, G. A. Prodi, L. G. Prokhorov, O. Puncken, M. Punturo, P. Puppo, M. Pürrer, H. Qi, J. Qin, S. Qiu, V. Quetschke, E. A. Quintero, R. Quitzow-James, F. J. Raab, D. S. Rabeling, H. Radkins, P. Raffai, S. Raja, C. Rajan, M. Rakhmanov, P. Rapagnani, V. Raymond, M. Razzano, V. Re, J. Read, T. Regimbau, L. Rei, S. Reid, D. H. Reitze, H. Rew, S. D. Reyes, E. Rhoades, F. Ricci, K. Riles, M. Rizzo, N. A. Robertson, R. Robie, F. Robinet, A. Rocchi, L. Rolland, J. G. Rollins, V. J. Roma, J. D. Romano, R. Romano, J. H. Romie, D. Rosińska, S. Rowan, A. Rüdiger, P. Ruggi, K. Ryan, S. Sachdev, T. Sadecki, L. Sadeghian, M. Sakellariadou, L. Salconi, M. Saleem, F. Salemi, A. Samajdar, L. Sammut, L. M. Sampson, E. J. Sanchez, V. Sandberg, J. R. Sanders, B. Sassolas, B. S. Sathyaprakash, P. R. Saulson, O. Sauter, R. L. Savage, A. Sawadsky, P. Schale, J. Scheuer, S. Schlassa, E. Schmidt, J. Schmidt, P. Schmidt, R. Schnabel, R. M. S. Schofield, A. Schönbeck, E. Schreiber, D. Schuette, B. F. Schutz, S. G. Schwalbe, J. Scott, S. M. Scott, D. Sellers, A. S. Sengupta, D. Sentenac, V. Sequino, A. Sergeev, Y. Setyawati, D. A. Shaddock, T. J. Shaffer, M. S. Shahriar, B. Shapiro, P. Shawhan, A. Sheperd, D. H. Shoemaker, D. M. Shoemaker, K. Siellez, X. Siemens, M. Sieniawska, D. Sigg, A. D. Silva, A. Singer, L. P. Singer, A. Singh, R. Singh, A. Singhal, A. M. Sintes, B. J. J. Slagmolen, B. Smith, J. R. Smith, R. J. E. Smith, E. J. Son, B. Sorazu, F. Sorrentino, T. Souradeep, A. P. Spencer, A. K. Srivastava, A. Staley, M. Steinke, J. Steinlechner, S. Steinlechner, D. Steinmeyer, B. C. Stephens, S. P. Stevenson, R. Stone, K. A. Strain, N. Straniero, G. Stratta, S. E. Strigin, R. Sturani, A. L. Stuver, T. Z. Summerscales, L. Sun, S. Sunil, P. J. Sutton, B. L. Swinkels, M. J. Szczepańczyk, M. Tacca, D. Talukder, D. B. Tanner, D. Tao, M. Tápai, A. Taracchini, R. Taylor, T. Theeg, E. G. Thomas, M. Thomas, P. Thomas, K. A. Thorne, E. Thrane, T. Tippens, S. Tiwari, V. Tiwari, K. V. Tokmakov, K. Toland, C. Tomlinson, M. Tonelli, Z. Tornasi, C. I. Torrie, D. Töyrä, F. Travasso, G. Traylor, D. Trifirò, J. Trinastic, M. C. Tringali, L. Trozzo, M. Tse, R. Tso, M. Turconi, D. Tuyenbayev, D. Ugolini, C. S. Unnikrishnan, A. L. Urban, S. A. Usman, H. Vahlbruch, G. Vajente, G. Valdes, N. van Bakel, M. van Beuzekom, J. F. J. van den Brand, C. Van Den Broeck, D. C. Vander-Hyde, L. van der Schaaf, J. V. van Heijningen, A. A. van Veggel, M. Vardaro, V. Varma, S. Vass, M. Vasúth, A. Vecchio, G. Vedovato, J. Veitch, P. J. Veitch, K. Venkateswara, G. Venugopalan, D. Verkindt, F. Vetrano, A. Viceré, A. D. Viets, S. Vinciguerra, D. J. Vine, J.-Y. Vinet, S. Vitale, T. Vo, H. Vocca, C. Vorvick, D. V. Voss, W. D. Vousden, S. P. Vyatchanin, A. R. Wade, L. E. Wade, M. Wade, M. Walker, L. Wallace, S. Walsh, G. Wang, H. Wang, M. Wang, Y. Wang, R. L. Ward, J. Warner, M. Was, J. Watchi, B. Weaver, L.-W. Wei, M. Weinert, A. J. Weinstein, R. Weiss, L. Wen, P. Weßels, T. Westphal, K. Wette, J. T. Whelan, B. F. Whiting, C. Whittle, D. Williams, R. D. Williams, A. R. Williamson, J. L. Willis, B. Willke, M. H. Wimmer, W. Winkler, C. C. Wipf, H. Wittel, G. Woan, J. Woehler, J. Worden, J. L. Wright, D. S. Wu, G. Wu, W. Yam, H. Yamamoto, C. C. Yancey, M. J. Yap, Hang Yu, Haocun Yu, M. Yvert, A. Zadrożny, L. Zangrando,

M. Zanolin, J.-P. Zendri, M. Zevin, L. Zhang, M. Zhang, T. Zhang, Y. Zhang, C. Zhao, M. Zhou, Z. Zhou, S. J. Zhu, X. J. Zhu, M. E. Zucker, and J. Zweizig. Upper limits on the stochastic gravitational-wave background from advanced ligo's first observing run. Phys. Rev. Lett., 118:121101, Mar 2017.

[165] Planck Collaboration, Y. Akrami, F. Arroja, M. Ashdown, J. Aumont, C. Baccigalupi, M. Ballardini, A. J. Banday, R. B. Barreiro, N. Bartolo, S. Basak, K. Benabed, J. P. Bernard, M. Bersanelli, P. Bielewicz, J. J. Bock, J. R. Bond, J. Borrill, F. R. Bouchet, F. Boulanger, M. Bucher, C. Burigana, R. C. Butler, E. Calabrese, J. F. Cardoso, J. Carron, A. Challinor, H. C. Chiang, L. P. L. Colombo, C. Combet, D. Contreras, B. P. Crill, F. Cuttaia, P. de Bernardis, G. de Zotti, J. Delabrouille, J. M. Delouis, E. Di Valentino, J. M. Diego, S. Donzelli, O. Doré, M. Douspis, A. Ducout, X. Dupac, S. Dusini, G. Efstathiou, F. Elsner, T. A. Enßlin, H. K. Eriksen, Y. Fantaye, J. Fergusson, R. Fernandez-Cobos, F. Finelli, F. Forastieri, M. Frailis, E. Franceschi, A. Frolov, S. Galeotta, S. Galli, K. Ganga, C. Gauthier, R. T. Génova-Santos, M. Gerbino, T. Ghosh, J. González-Nuevo, K. M. Górski, S. Gratton, A. Gruppuso, J. E. Gudmundsson, J. Hamann, W. Handley, F. K. Hansen, D. Herranz, E. Hivon, D. C. Hooper, Z. Huang, A. H. Jaffe, W. C. Jones, E. Keihänen, R. Keskitalo, K. Kiiveri, J. Kim, T. S. Kisner, N. Krachmalnicoff, M. Kunz, H. Kurki-Suonio, G. Lagache, J. M. Lamarre, A. Lasenby, M. Lattanzi, C. R. Lawrence, M. Le Jeune, J. Lesgourgues, F. Levrier, A. Lewis, M. Liguori, P. B. Lilje, V. Lindholm, M. Lpez-Caniego, P. M. Lubin, Y. Z. Ma, J. F. Mac´ias-Pérez, G. Maggio, D. Maino, N. Mandolesi, A. Mangilli, A. Marcos-Caballero, M. Maris, P. G. Martin, E. Mart´inez-González, S. Matarrese, N. Mauri, J. D. McEwen, P. D. Meerburg, P. R. Meinhold, A. Melchiorri, A. Mennella, M. Migliaccio, S. Mitra, M. A. Miville-Deschênes, D. Molinari, A. Moneti, L. Montier, G. Morgante, A. Moss, M. Münchmeyer, P. Natoli, H. U. Nørgaard-Nielsen, L. Pagano, D. Paoletti, B. Partridge, G. Patanchon, H. V. Peiris, F. Perrotta, V. Pettorino, F. Piacentini, L. Polastri, G. Polenta, J. L. Puget, J. P. Rachen, M. Reinecke, M. Remazeilles, A. Renzi, G. Rocha, C. Rosset, G. Roudier, J. A. Rubiño-Mart´in, B. Ruiz-Granados, L. Salvati, M. Sandri, M. Savelainen, D. Scott, E. P. S. Shellard, M. Shiraishi, C. Sirignano, G. Sirri, L. D. Spencer, R. Sunyaev, A. S. Suur-Uski, J. A. Tauber, D. Tavagnacco, M. Tenti, L. Toffolatti, M. Tomasi, T. Trombetti, J. Valiviita, B. Van Tent, P. Vielva, F. Villa, N. Vittorio, B. D. Wandelt, I. K. Wehus, S. D. M. White, A. Zacchei, J. P. Zibin, and A. Zonca. Planck 2018 results. X. Constraints on inflation. arXiv e-prints, page arXiv:1807.06211, July 2018.

[166] P. A. R. Ade, Z. Ahmed, R. W. Aikin, K. D. Alexander, D. Barkats, S. J. Benton, C. A. Bischoff, J. J. Bock, R. Bowens-Rubin, J. A. Brevik, I. Buder, E. Bullock, V. Buza, J. Connors, J. Cornelison, B. P. Crill, M. Crumrine, M. Dierickx, L. Duband, C. Dvorkin, J. P. Filippini, S. Fliescher, J. Grayson, G. Hall, M. Halpern, S. Harrison, S. R. Hildebrandt, G. C. Hilton, H. Hui, K. D. Irwin, J. Kang, K. S. Karkare, E. Karpel, J. P. Kaufman, B. G. Keating, S. Kefeli, S. A. Kernasovskiy, J. M. Kovac, C. L. Kuo, N. A. Larsen, K. Lau, E. M. Leitch, M. Lueker, K. G. Megerian, L. Moncelsi, T. Namikawa, C. B. Netterfield, H. T. Nguyen, R. O'Brient, R. W. Ogburn, S. Palladino, C. Pryke, B. Racine, S. Richter, A. Schillaci, R. Schwarz, C. D. Sheehy, A. Soliman,

T. St. Germaine, Z. K. Staniszewski, B. Steinbach, R. V. Sudiwala, G. P. Teply, K. L. Thompson, J. E. Tolan, C. Tucker, A. D. Turner, C. Umiltà, A. G. Vieregg, A. Wandui, A. C. Weber, D. V. Wiebe, J. Willmert, C. L. Wong, W. L. K. Wu, H. Yang, K. W. Yoon, and C. Zhang. Constraints on primordial gravitational waves using *planck*, wmap, and new bicep2/*keck* observations through the 2015 season. Phys. Rev. Lett., 121:221301, Nov 2018.

[167] Nicola Bartolo, Chiara Caprini, Valerie Domcke, Daniel G. Figueroa, Juan Garcia-Bellido, Maria Chiara Guzzetti, Michele Liguori, Sabino Matarrese, Marco Peloso, Antoine Petiteau, Angelo Ricciardone, Mairi Sakellariadou, Lorenzo Sorbo, and Gianmassimo Tasinato. Science with the space-based interferometer LISA. IV: probing inflation with gravitational waves. Journal of Cosmology and Astroparticle Physics, 2016(12):026–026, dec 2016.

[168] Kevork N. Abazajian, Peter Adshead, Zeeshan Ahmed, Steven W. Allen, David Alonso, Kam S. Arnold, Carlo Baccigalupi, James G. Bartlett, Nicholas Battaglia, Bradford A. Benson, Colin A. Bischoff, Julian Borrill, Victor Buza, Erminia Calabrese, Robert Caldwell, John E. Carlstrom, Clarence L. Chang, Thomas M. Crawford, Francis-Yan Cyr-Racine, Francesco De Bernardis, Tijmen de Haan, Sperello di Serego Alighieri, Joanna Dunkley, Cora Dvorkin, Josquin Errard, Giulio Fabbian, Stephen Feeney, Simone Ferraro, Jeffrey P. Filippini, Raphael Flauger, George M. Fuller, Vera Gluscevic, Daniel Green, Daniel Grin, Evan Grohs, Jason W. Henning, J. Colin Hill, Renee Hlozek, Gilbert Holder, William Holzapfel, Wayne Hu, Kevin M. Huffenberger, Reijo Keskitalo, Lloyd Knox, Arthur Kosowsky, John Kovac, Ely D. Kovetz, Chao-Lin Kuo, Akito Kusaka, Maude Le Jeune, Adrian T. Lee, Marc Lilley, Marilena Loverde, Mathew S. Madhavacheril, Adam Mantz, David J. E. Marsh, Jeffrey McMahon, Pieter Daniel Meerburg, Joel Meyers, Amber D. Miller, Julian B. Munoz, Ho Nam Nguyen, Michael D. Niemack, Marco Peloso, Julien Peloton, Levon Pogosian, Clement Pryke, Marco Raveri, Christian L. Reichardt, Graca Rocha, Aditya Rotti, Emmanuel Schaan, Marcel M. Schmittfull, Douglas Scott, Neelima Sehgal, Sarah Shandera, Blake D. Sherwin, Tristan L. Smith, Lorenzo Sorbo, Glenn D. Starkman, Kyle T. Story, Alexander van Engelen, Joaquin D. Vieira, Scott Watson, Nathan Whitehorn, and W. L. Kimmy Wu. CMB-S4 Science Book, First Edition. arXiv e-prints, page arXiv:1610.02743, October 2016.

[169] P. Daniel Meerburg, Renée Hložek, Boryana Hadzhiyska, and Joel Meyers. Multiwavelength constraints on the inflationary consistency relation. Phys. Rev. D, 91:103505, May 2015.

[170] Ido Ben-Dayan. Gravitational waves in bouncing cosmologies from gauge field production. Journal of Cosmology and Astroparticle Physics, 2016(09):017–017, sep 2016.

[171] Ido Ben-Dayan and Judy Kupferman. Sourced scalar fluctuations in bouncing cosmology. Journal of Cosmology and Astroparticle Physics, 2019(07):050–050, jul 2019.

[172] Jens Chluba, Adrienne L. Erickcek, and Ido Ben-Dayan. PROBING THE INFLATON: SMALL-SCALE POWER SPECTRUM CONSTRAINTS FROM MEASUREMENTS

OF THE COSMIC MICROWAVE BACKGROUND ENERGY SPECTRUM. The Astrophysical Journal, 758(2):76, sep 2012.

[173] Ido Ben-Dayan and Tigran Kalaydzhyan. Constraining the primordial power spectrum from snia lensing dispersion. Phys. Rev. D, 90:083509, Oct 2014.

[174] Ido Ben-Dayan. Lensing dispersion of SNIa and small scales of the primordial power spectrum. arXiv e-prints, page arXiv:1408.3004, August 2014.

[175] Ido Ben-Dayan and Ryuichi Takahashi. Constraints on small-scale cosmological fluctuations from SNe lensing dispersion. Monthly Notices of the Royal Astronomical Society, 455(1):552–562, 11 2015.

[176] Torsten Bringmann, Pat Scott, and Yashar Akrami. Improved constraints on the primordial power spectrum at small scales from ultracompact minihalos. Phys. Rev. D, 85:125027, Jun 2012.

[177] J.P.P. Vieira, Christian T. Byrnes, and Antony Lewis. Can power spectrum observations rule out slow-roll inflation? Journal of Cosmology and Astroparticle Physics, 2018(01):019–019, jan 2018.

[178] Silvia Mollerach, Diego Harari, and Sabino Matarrese. Cmb polarization from secondary vector and tensor modes. Phys. Rev. D, 69:063002, Mar 2004.

[179] Kishore N. Ananda, Chris Clarkson, and David Wands. Cosmological gravitational wave background from primordial density perturbations. Phys. Rev. D, 75:123518, Jun 2007.

[180] Daniel Baumann, Paul Steinhardt, Keitaro Takahashi, and Kiyotomo Ichiki. Gravitational wave spectrum induced by primordial scalar perturbations. Phys. Rev. D, 76:084019, Oct 2007.

[181] Laila Alabidi, Kazunori Kohri, Misao Sasaki, and Yuuiti Sendouda. Observable spectra of induced gravitational waves from inflation. Journal of Cosmology and Astroparticle Physics, 2012(09):017–017, sep 2012.

[182] Kazunori Kohri and Takahiro Terada. Semianalytic calculation of gravitational wave spectrum nonlinearly induced from primordial curvature perturbations. Phys. Rev. D, 97:123532, Jun 2018.

[183] Christian T. Byrnes, Philippa S. Cole, and Subodh P. Patil. Steepest growth of the power spectrum and primordial black holes. Journal of Cosmology and Astroparticle Physics, 2019(06):028–028, jun 2019.

[184] Keisuke Inomata and Tomohiro Nakama. Gravitational waves induced by scalar perturbations as probes of the small-scale primordial spectrum. Phys. Rev. D, 99:043511, Feb 2019.

[185] Peter Ade, James Aguirre, Zeeshan Ahmed, Simone Aiola, Aamir Ali, David Alonso, Marcelo A. Alvarez, Kam Arnold, Peter Ashton, Jason Austermann, Humna Awan, Carlo Baccigalupi, Taylor Baildon, Darcy Barron, Nick Battaglia, Richard Battye, Eric Baxter, Andrew Bazarko, James A. Beall, Rachel Bean, Dominic Beck, Shawn Beckman, Benjamin Beringue, Federico Bianchini, Steven Boada, David Boettger, J. Richard Bond, Julian Borrill, Michael L. Brown, Sarah Marie Bruno, Sean Bryan, Erminia Calabrese, Victoria Calafut, Paolo Calisse, Julien Carron, Anthony Challinor, Grace Chesmore, Yuji Chinone, Jens Chluba, Hsiao-Mei Sherry Cho, Steve Choi, Gabriele Coppi, Nicholas F. Cothard, Kevin Coughlin, Devin Crichton, Kevin D. Crowley, Kevin T. Crowley, Ari Cukierman, John M. D'Ewart, Rolando Dünner, Tijmen de Haan, Mark Devlin, Simon Dicker, Joy Didier, Matt Dobbs, Bradley Dober, Cody J. Duell, Shannon Duff, Adri Duivenvoorden, Jo Dunkley, John Dusatko, Josquin Errard, Giulio Fabbian, Stephen Feeney, Simone Ferraro, Pedro Fluxà, Katherine Freese, Josef C. Frisch, Andrei Frolov, George Fuller, Brittany Fuzia, Nicholas Galitzki, Patricio A. Gallardo, Jose Tomas Galvez Ghersi, Jiansong Gao, Eric Gawiser, Martina Gerbino, Vera Gluscevic, Neil Goeckner-Wald, Joseph Golec, Sam Gordon, Megan Gralla, Daniel Green, Arpi Grigorian, John Groh, Chris Groppi, Yilun Guan, Jon E. Gudmundsson, Dongwon Han, Peter Hargrave, Masaya Hasegawa, Matthew Hasselfield, Makoto Hattori, Victor Haynes, Masashi Hazumi, Yizhou He, Erin Healy, Shawn W. Henderson, Carlos Hervias-Caimapo, Charles A. Hill, J. Colin Hill, Gene Hilton, Matt Hilton, Adam D. Hincks, Gary Hinshaw, Renée Hložek, Shirley Ho, Shuay-Pwu Patty Ho, Logan Howe, Zhiqi Huang, Johannes Hubmayr, Kevin Huffenberger, John P. Hughes, Anna Ijjas, Margaret Ikape, Kent Irwin, Andrew H. Jaffe, Bhuvnesh Jain, Oliver Jeong, Daisuke Kaneko, Ethan D. Karpel, Nobuhiko Katayama, Brian Keating, Sarah S. Kernasovskiy, Reijo Keskitalo, Theodore Kisner, Kenji Kiuchi, Jeff Klein, Kenda Knowles, Brian Koopman, Arthur Kosowsky, Nicoletta Krachmalnicoff, Stephen E. Kuenstner, Chao-Lin Kuo, Akito Kusaka, Jacob Lashner, Adrian Lee, Eunseong Lee, David Leon, Jason S. Y. Leung, Antony Lewis, Yaqiong Li, Zack Li, Michele Limon, Eric Linder, Carlos Lopez-Caraballo, Thibaut Louis, Lindsay Lowry, Marius Lungu, Mathew Madhavacheril, Daisy Mak, Felipe Maldonado, Hamdi Mani, Ben Mates, Frederick Matsuda, Lo¨ic Maurin, Phil Mauskopf, Andrew May, Nialh McCallum, Chris McKenney, Jeff McMahon, P. Daniel Meerburg, Joel Meyers, Amber Miller, Mark Mirmelstein, Kavilan Moodley, Moritz Munchmeyer, Charles Munson, Sigurd Naess, Federico Nati, Martin Navaroli, Laura Newburgh, Ho Nam Nguyen, Michael Niemack, Haruki Nishino, John Orlowski-Scherer, Lyman Page, Bruce Partridge, Julien Peloton, Francesca Perrotta, Lucio Piccirillo, Giampaolo Pisano, Davide Poletti, Roberto Puddu, Giuseppe Puglisi, Chris Raum, Christian L. Reichardt, Mathieu Remazeilles, Yoel Rephaeli, Dominik Riechers, Felipe Rojas, Anirban Roy, Sharon Sadeh, Yuki Sakurai, Maria Salatino, Mayuri Sathyanarayana Rao, Emmanuel Schaan, Marcel Schmittfull, Neelima Sehgal, Joseph Seibert, Uros Seljak, Blake Sherwin, Meir Shimon, Carlos Sierra, Jonathan Sievers, Precious Sikhosana, Maximiliano Silva-Feaver, Sara M. Simon, Adrian Sinclair, Praween Siritanasak, Kendrick Smith, Stephen R. Smith, David Spergel, Suzanne T. Staggs, George Stein, Jason R. Stevens, Radek Stompor, Aritoki Suzuki, Osamu Tajima, Satoru Takakura, Grant Teply, Daniel B. Thomas, Ben Thorne, Robert Thornton, Hy Trac, Calvin Tsai, Carole Tucker, Joel Ullom, Sunny Vagnozzi,

Alexander van Engelen, Jeff Van Lanen, Daniel D. Van Winkle, Eve M. Vavagiakis, Clara Vergès, Michael Vissers, Kasey Wagoner, Samantha Walker, Jon Ward, Ben Westbrook, Nathan Whitehorn, Jason Williams, Joel Williams, Edward J. Wollack, Zhilei Xu, Byeonghee Yu, Cyndia Yu, Fernando Zago, Hezi Zhang, Ningfeng Zhu, and Simons Observatory Collaboration. The Simons Observatory: science goals and forecasts. J. Cosmology Astropart. Phys., 2019(2):056, February 2019.

[186] P. A. R. Ade, Z. Ahmed, R. W. Aikin, K. D. Alexander, D. Barkats, S. J. Benton, C. A. Bischoff, J. J. Bock, R. Bowens-Rubin, J. A. Brevik, I. Buder, E. Bullock, V. Buza, J. Connors, B. P. Crill, L. Duband, C. Dvorkin, J. P. Filippini, S. Fliescher, J. Grayson, M. Halpern, S. Harrison, G. C. Hilton, H. Hui, K. D. Irwin, K. S. Karkare, E. Karpel, J. P. Kaufman, B. G. Keating, S. Kefeli, S. A. Kernasovskiy, J. M. Kovac, C. L. Kuo, E. M. Leitch, M. Lueker, K. G. Megerian, C. B. Netterfield, H. T. Nguyen, R. O'Brient, R. W. Ogburn, A. Orlando, C. Pryke, S. Richter, R. Schwarz, C. D. Sheehy, Z. K. Staniszewski, B. Steinbach, R. V. Sudiwala, G. P. Teply, K. L. Thompson, J. E. Tolan, C. Tucker, A. D. Turner, A. G. Vieregg, A. C. Weber, D. V. Wiebe, J. Willmert, C. L. Wong, W. L. K. Wu, and K. W. Yoon. Improved constraints on cosmology and foregrounds from bicep2 and keck array cosmic microwave background data with inclusion of 95 ghz band. Phys. Rev. Lett., 116:031302, Jan 2016.

[187] Antony Lewis and Sarah Bridle. Cosmological parameters from cmb and other data: A monte carlo approach. Phys. Rev. D, 66:103511, Nov 2002.

[188] N. Stebor, P. Ade, Y. Akiba, C. Aleman, K. Arnold, C. Baccigalupi, B. Barch, D. Barron, S. Beckman, A. Bender, D. Boettger, J. Borrill, S. Chapman, Y. Chinone, A. Cukierman, T. de Haan, M. Dobbs, A. Ducout, R. Dunner, T. Elleflot, J. Errard, G. Fabbian, S. Feeney, C. Feng, T. Fujino, G. Fuller, A. J. Gilbert, N. Goeckner-Wald, J. Groh, G. Hall, N. Halverson, T. Hamada, M. Hasegawa, K. Hattori, M. Hazumi, C. Hill, W. L. Holzapfel, Y. Hori, L. Howe, Y. Inoue, F. Irie, G. Jaehnig, A. Jaffe, O. Jeong, N. Katayama, J. P. Kaufman, K. Kazemzadeh, B. G. Keating, Z. Kermish, R. Keskitalo, T. Kisner, A. Kusaka, M. Le Jeune, A. T. Lee, D. Leon, E. V. Linder, L. Lowry, F. Matsuda, T. Matsumura, N. Miller, J. Montgomery, M. Navaroli, H. Nishino, H. Paar, J. Peloton, D. Poletti, G. Puglisi, C. R. Raum, G. M. Rebeiz, C. L. Reichardt, P. L. Richards, C. Ross, K. M. Rotermund, Y. Segawa, B. D. Sherwin, I. Shirley, P. Siritanasak, L. Steinmetz, R. Stompor, A. Suzuki, O. Tajima, S. Takada, S. Takatori, G. P. Teply, A. Tikhomirov, T. Tomaru, B. Westbrook, N. Whitehorn, A. Zahn, and O. Zahn. The Simons Array CMB polarization experiment, volume 9914 of Society of Photo-Optical Instrumentation Engineers (SPIE) Conference Series, page 99141H. 2016.

[189] Andrew S. Friedman, David Leon, Roman Gerasimov, Kevin D. Crowley, Isaac Broudy, Yash Melkani, Walker Stevens, Delwin Johnson, Grant Teply, David Tytler, Brian G. Keating, and Gary M. Cole. Standard-model extension constraints on lorentz and cpt violation from optical polarimetry of active galactic nuclei, 2019.

[190] Andrew S. Friedman, Roman Gerasimov, Fabian Kislat, David Leon, Walker Stevens, David Tytler, and Brian G. Keating. Improved Constraints on Anisotropic Birefringent

Lorentz Invariance and CPT Violation from Broadband Optical Polarimetry of High Redshift Galaxies. arXiv e-prints, page arXiv:2003.00647, March 2020.